Title
True polar wander on convecting planets

Author
Rose, Ian Robert

Publication Date
2016

Peer reviewed|Thesis/dissertation

True polar wander on convecting planets

By

Ian Robert Rose

A dissertation submitted in partial satisfaction of the

requirements for the degree of

Doctor of Philosophy

in

Earth and Planetary Science

in the

Graduate Division

of the

University of California, Berkeley

Committee in charge:

Professor Bruce Buffett, Chair
Professor Nicholas Swanson-Hysell
Professor Philip Marcus

Summer 2016

True polar wander on convecting planets

Abstract

True polar wander on convecting planets

by

Ian Robert Rose

Doctor of Philosophy in Earth and Planetary Science

University of California, Berkeley

Professor Bruce Buffett, Chair

Rotating planets are most stable when spinning around their maximum moment of inertia, and will tend to reorient themselves to achieve this configuration. Geological activity redistributes mass in the planet, making the moment of inertia a function of time. As the moment of inertia of the planet changes, the spin axis shifts with respect to a mantle reference frame in order to maintain rotational stability. This process is known as true polar wander (TPW). Of the processes that contribute to a planet's moment of inertia, convection in the mantle generates the largest and longest-period fluctuations, with corresponding shifts in the spin axis. True polar wander has been hypothesized to explain several physiographic features on planets and moons in our solar system. On Earth, TPW events have been invoked in some interpretations of paleomagnetic data. Large swings in the spin axis could have enormous ramifications for paleogeography, paleoclimate, and the history of life.

Although the existence of TPW is well-verified, it is not known whether its rate and magnitude have been large enough for it to be an important process in Earth history. If true polar wander has been sluggish compared to plate tectonic speeds, then it would be difficult to detect and its consequences would be minor. Herein I investigate rates of true polar wander on convecting planets using scaling, numerics, and inverse problems.

I perform a scaling analysis of TPW on a convecting planet, identifying a minimal set of nondimensional parameters which describe the problem. The primary nondimensional numbers that control the rate of TPW are the ratio of centrifugal to gravitational forces (m) and the Rayleigh number (Ra). The parameter m sets the size of a planet's rotational bulge, which determines the amount of work that needs to be done to move the spin axis. The Rayleigh number controls the size, distribution, and rate of change of moment of inertia anomalies, all of which affect the rate of TPW. I find that the characteristic size of moment of inertia anomalies decreases with higher Ra, but that the characteristic response time for TPW also decreases. These two effects approximately cancel. However, the orientation of the principal axes of the moment of inertia becomes less stable to perturbations at high Ra, thereby increasing the rate of TPW. Overall, I find that a more vigorously convecting planet

(one with a higher Ra) is more likely to experience large TPW events. If early Earth had more vigorous convection, it may have experienced more TPW than present-day Earth.

Flow induced by density anomalies in the mantle deflects free surfaces at the surface and the CMB, and the mass anomalies due to these deflections contribute to the moment of inertia. A full accounting of the moment of inertia anomalies must include these surface effects. Numerical models of mantle convection with a free surface have suffered from numerical sloshing instabilities. I analyze the sloshing instability by constructing a generalized eigenvalue problem for the relaxation time spectrum. The minimum relaxation time of the spectrum sets the maximum stable timestep. This analysis gives the first quantitative explanation for why existing techniques for stabilizing geodynamic simulations with a free surface work. I also use this perspective to construct an alternative stabilization scheme based on nonstandard finite differences. This scheme has a single parameter, given by an estimate of the minimum relaxation time, and allows for still larger timesteps.

Finally, I develop a new method for analyzing apparent polar wander (APW) paths described by sequences of paleomagnetic poles. Existing techniques, such as spline fits and running means, do not fully account for the uncertainties in the position and timing of paleomagnetic pole paths. Furthermore, they impose regularization on the solution, and the resulting uncertainties are difficult to interpret. Our technique is an extension of paleomagnetic Euler pole (PEP) analysis. I invert for finite Euler pole rotations that can reproduce APW paths within a Bayesian Markov chain Monte Carlo (MCMC) framework. This allows us to naturally include uncertainties in age and position, and provides error estimates on the resulting model parameters. Regularization can be accomplished via physically motivated choices for the parameters' prior probability distributions.

I applied the Bayesian PEP technique to the Mesoproterozoic Laurentian APW track, which primarily comes from the Keweenawan Midcontinent Rift. I fit the track with one and two Euler rotations. Both inversions did a good job of reproducing the Keweenawan track, though the two Euler pole inversion has a closer fit. I find that the implied Laurentian plate speeds exceeds 22.9 cm/yr at the 95% confidence level. These speeds are significantly faster than Cenozoic plate speeds, and could be explained by either faster plate speeds in the Proterozoic or a TPW event.

For my family

Contents

List of Figures

List of Tables

Acknowledgments

An undertaking as large as a Ph.D cannot be done alone, despite the occasional use of the first person singular in this document. I have received encouragement, help, insight, and support from many people at every step of the way, and I would not have gotten to this point without them.

First and foremost, I thank my advisor, Bruce Buffett. Bruce is an inspiring scientist, with a breadth and depth of knowledge that I have yet to exhaust, and a range of research projects that spans the whole planet. Even in the times when I have come to him with a problem which he as not previously encountered, his instincts almost always point me in the right direction. More than this, Bruce has given me the intellectual space to craft my own path, to make my own mistakes, and form my own conclusions.

Thanks to Nicholas Swanson-Hysell, who arrived at Berkeley during my degree, and jumped into the work I was doing without hesitation. His thoughts and insights have been invaluable. Thanks to Michael Manga, who taught me so many things about science and academia, even when I did not initially understand them. Thanks to Phil Marcus, a skilled fluid dynamicist who expanded my toolbox of analytical and numerical techniques, and more importantly, expanded my intuition for the behavior of PDEs and their solution using computers.

Thanks furthermore to two non-Berkeley faculty, Timo Heister and Wolfgang Bangerth, who taught me how to to program. They are both top-notch mathematicians with many demands on their time. Despite that, they view both education and community-building as equally important as their research, and I have benefited immensely from their efforts.

Thanks to my undergraduate advisors Dave Evans, Jun Korenaga, and Mark Brandon, who incited my love of Earth science.

Two institutions have supported my development as a scientist in such a fundamental way that I would certainly not have gotten here without them. The first institution is CIDER, the deep Earth summer program held at the Kavli Institute for Theoretical Physics, which has been an amazing resource for learning and research. The directors of the program, led by the incomparable Barbara Romanowicz, have reshaped the field of deep Earth research and built a durable community. The second institution is CIG, led by Louise Kellog, which has done more than any other institution to promote the open development and use of software in Earth science. CIG-developed (and CIG-maintained) software has touched nearly every aspect of this dissertation.

More broadly than CIG, open source software has contributed enormously to my work. At some point in the near future, the transparent and reproducible use of scientific software will be universally seen as a crucial component of good science, and many great open source projects are showing the way. These projects have dozens or hundreds of contributors, many of whom contribute for no pay. They cannot all be thanked here, but I have particularly benefitted from the work put into `ASPECT`, `deal.II`, `Burnman`, Numpy, Scipy, Matplotlib, and PyMC. This dissertation was typeset using the ucastrothesis LaTeX template.

My fellow graduate students have been an incredible resource, and I have learned as much from them as any coursework. I want to thank Max, Edwin, Amanda, Leif, Ved, Scott, Tyler, Jesse, Nick, Percy, Daniella, Patrick, Jennifer, and Seth, for being both colleagues and friends. Importantly, I thank Carolina, Brent, Noah, Zack, Slayer, Pam, and Sanne for being friends first when it mattered. My non-Earth science friends, including Caitlin, Katherine, Andy, Anna, Emily, Chase, Lauren, Jenny, Mary, Marc, Alice, Claire, Gerstle, Jay, and Jacob provided important encouragement and perspective. David Mangiante, my sometimes officemate, oftentimes co-schemer, and always friend, has kept me thinking about what is most important in life.

Finally, my family has been an unending source of unconditional love and support. Mom, Dad, Noah and Morgan, I would not be here without you. Thank you.

Chapter 1

Introduction

1.1 Prelude

Two of the most foundational observations of the Earth system are (1) that the planet is cooling off from a combination of primordial heat and the decay of radioactive elements, and (2) that it is rotating. The cooling of the planet results in convection in Earth's interior and its surface expression in plate tectonics, and is thus responsible for a great deal of the geologic activity that we experience. The rotation of the planet is a dominant factor in the fluid dynamics of the oceans, atmosphere, and core. In this dissertation we consider the interaction between convection in Earth's mantle and the rotational dynamics of the planet. We may relate the two processes through the classical angular momentum equation. Conservation of angular momentum in a rotating reference frame for a torque free planet requires

$$\frac{\partial \mathbf{H}}{\partial t} + \boldsymbol{\Omega} \times \mathbf{H} = 0, \tag{1.1}$$

where the angular momentum $\mathbf{H}$ is given by $\mathbf{H} = \mathbf{I} \cdot \boldsymbol{\Omega}$, $\mathbf{I}$ is the moment of inertia tensor, and $\boldsymbol{\Omega}$ is the angular velocity vector. For geologic processes the effects of inertia are small, so the inertial term $\partial \mathbf{H}/\partial t$ may be neglected, and the conservation equation becomes

$$\boldsymbol{\Omega} \times (\mathbf{I} \cdot \boldsymbol{\Omega}) = 0. \tag{1.2}$$

Convection in Earth's mantle, by its very nature, involves the transfer mass of different densities, as cold lithosphere sinks into the mantle, and buoyant plumes rise from the core mantle boundary (CMB). This transfer of mass changes the density structure of the mantle, thereby changing the moment of inertia. Equation (1.2) is a strong constraint on $\boldsymbol{\Omega}$: if the moment of inertia is a function of time, then the spin axis must also be a function of time. The change in direction of a planet's spin axis as a response to a changing moment of inertia is known as true polar wander (TPW), which is the primary focus of this dissertation. In the following sections we give a brief account of the history of conceptions of TPW, as well as an overview of the content of the dissertation.

Figure 1.1: Map of the world according to Macrobius Ambrosius Theodosius in *De Somnio Scipionis*, or *Dream of Scipio*, *ca.* 430 C.E.. It shows a great southern continent, which was thought to be very similar to the known northern lands, and fed into the legend of *Terra Australis*. The map was reproduced and reinterpreted many times during the medieval period and Renaissance. This particular print comes from a 1515 reproduction.

1.2 A short history of true polar wander

Although true polar wander as it is understood today is a relatively recent concept, concerns about the stability of Earth and its place in the universe are quite old. Aristotle advanced a conception of nature that relied heavily on order and symmetry. This philosophy entered into the worldview of early Mediterranean cartographers, who, knowing that they lived in the northern hemisphere, postulated that there must be a large southern continent to preserve symmetry and balance in the world (Wilford, 2001). This hypothetical southern continent became known as *Terra Incognita Australis*, from which we get the name "Australia".

Among the earliest maps showing the southern continent was that of Macrobius Ambrosius Theodosius, a fifth century Roman author. His map, from *De Somnio Scipionis*, showed the large southern continent largely mirroring the northern continents in shape and size (Figure 1.1). This map became hugely influential in medieval and Renaissance cartography (Stahl, 1942). During the Renaissance, ideas about Earth's place in the solar system famously became entwined with Catholic theology. In the 17th century the Jesuit scholar Athanasius Kircher published a series of treatises on geology and volcanology. In his *Turris*

Babel (1679) Kircher interpreted the Biblical story of the Tower of Babel as meaning that the tower was intended to reach the moon. He performed a series of calculations about how much material would be needed to build such a tower, determined where the planet's new center of mass would be, and concluded: "... the motion of the earthly globe from it center would bring the total ruin of nature below" (see Figure 1.2).

A more modern approach to Earth's stability can be found in Newton's *Principia* (1687), where he describes the tendency of mass anomalies to move towards the equator of a spinning object:

> ... let there be added anywhere between the pole and the equator a heap of new matter like a mountain, and this, by its continual endeavor to recede from the center of its motion, will disturb the motion of the globe, and cause its poles to wander about its surface describing circles about themselves and the points opposite them. Neither can this enormous deviation of the poles be corrected otherwise than by placing that mountain either in one of the poles... or in the equatorial regions...

During the 18th and 19th centuries, as the science of geology developed, catastrophic polar wandering became a possible explanation for the puzzling paleoclimatic and paleontologic findings, such as coal seams in Svalbard and low-latitude glacial deposits (Barrell, 1914). Alfred Wegener, most famous for originating the theory of continental drift, published a paleoclimatology book with Wladimir Köppen (Köppen and Wegener, 1924) which, in addition to providing a continental reconstruction, attempted infer a paleopole position from their data.

The first scientist to approach polar wandering from a quantitative perspective was George Darwin (son of Charles) in 1887. In a manuscript given before the Royal Society (Darwin, 1887) he described what is essentially the modern concept of true polar wander:

> ... If the earth were a viscous fluid there is no doubt that the pole of the figure would tend to displace itself towards the instantaneous axis... But Sir William Thomson has shown that the earth is sensibly rigid; and in any case the earth is not a viscous fluid, sensibly called, although it may be slightly plastic.

In other words, he concluded that if Earth were sufficiently deformable, polar wandering would be inevitable, but he had been convinced by William Thomson (not yet Lord Kelvin) that it was too rigid for large scale motion of the poles.

After Darwin there was little further work on the physics of polar wandering until the 1950s. At that time, the first geophysical evidence for polar wandering was emerging in the form of paleomagnetism. In a series of papers by Ken Creer, Keith Runcorn and Ted Irving (Creer et al., 1954; Runcorn, 1955; Creer et al., 1957) paleomagnetic data, primarily from Britain and North America, showed that the north pole had apparently shifted significantly since the Precambrian. They considered both continental drift and true polar wander as

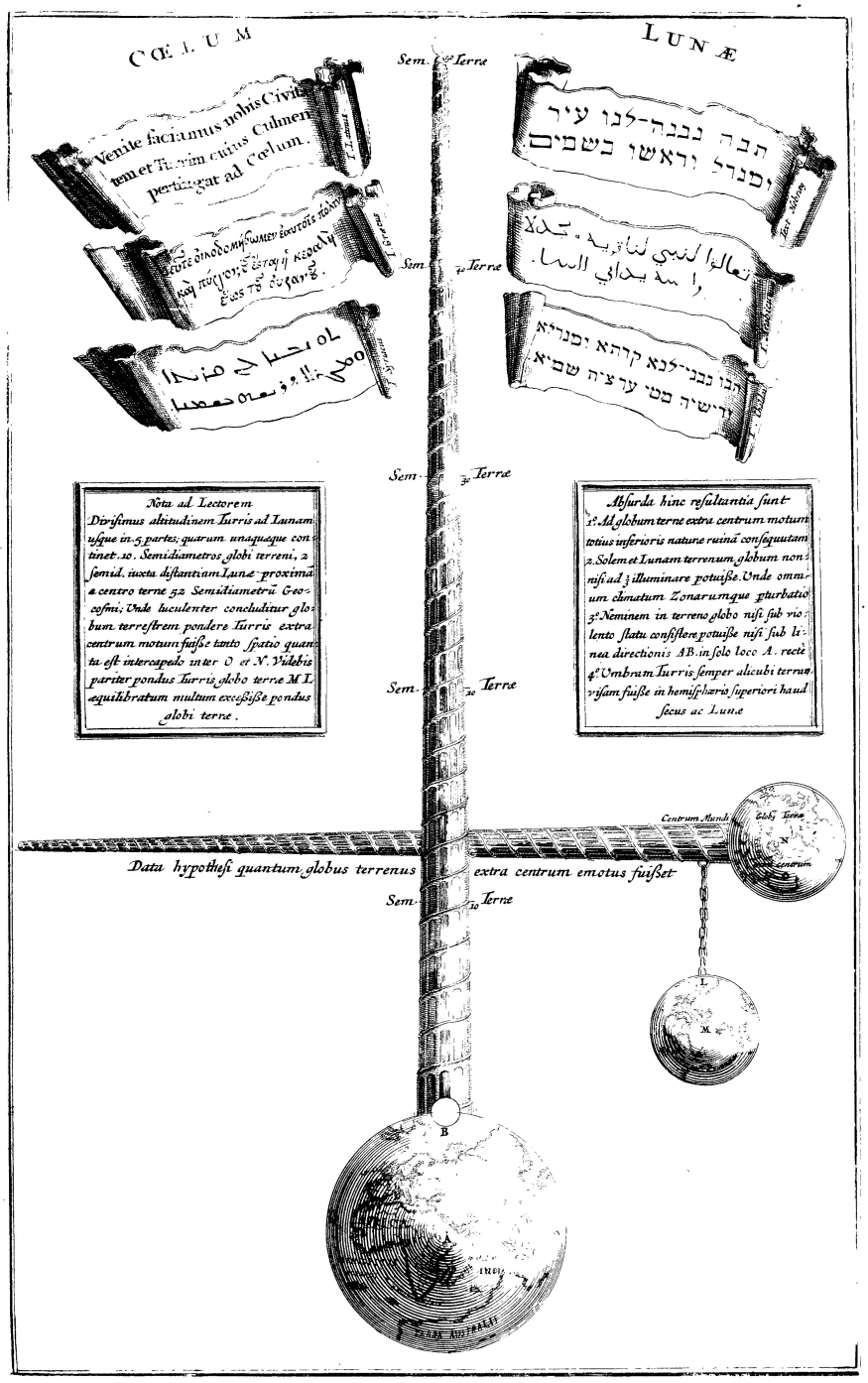

Figure 1.2: Plate from *Turris Babel* (1679), by Athanasius Kircher. A fanciful thought experiment about the consequences of building the Tower of Babel to the moon.

possible explanations for this wandering, with a preference for polar wander due to its simplicity. However, as more paleomagnetic evidence mounted (e.g. Irving and Green, 1958), it became clear that different continents displayed different paleomagnetic apparent polar wander paths, and apparent polar wandering became more frequently ascribed to the new theory of plate tectonics. This is also where the terminology of "true polar wander" begins, in order to distinguish it from the apparent polar wander due to plate motions.

At the same time, the dynamical theory of true polar wander began to receive more attention, as the geophysical evidence began mounting that, on geological timescales, Earth is more plastic than rigid. Gold (1955) provided a qualitative description of true polar wander that included the famous mixed-metaphor of a beetle crawling around on a perfectly spherical Earth, the spin axis always trying to catch up with it, "as with the ass and the carrot hanging from a stick held by the rider." Munk and MacDonald (1960) established the modern theoretical framework for TPW in their landmark book *The Rotation of the Earth*. Goldreich and Toomre (1969) pointed out that in a convecting system there are many density anomalies contributing to the moment of inertia, and they extended Gold's beetle thought experiment to include many beetles crawling over Earth's surface. In this case, the principal axes of Earth's moment of inertia do not track any one beetle, and they may move faster than the beetles crawl.

In more recent years there has been renewed interest in true polar wander as an important process in Earth history. A rapid reorientation of the solid Earth would have enormous consequences for paleoclimate (Kirschvink et al., 1997), as the poles could become tropics, and the tropics poles. The readjustment of the rotational bulge would cause global shifts in sea level (Mound et al., 1999). These effects could have had a profound impact on the history of life (e.g Kirschvink and Raub, 2003). Furthermore, the melting of glaciers and polar ice caps is the dominant cause of present-day TPW (Adhikari and Ivins, 2016), providing important constraints for paleoclimate reconstructions (Milne and Mitrovica, 1996). Finally, as we have explored the solar system it has become clear that TPW may be an important process on other planetary bodies as well. TPW has been suggested as an explanation for features on Mars (Perron et al., 2007), Enceladus (Nimmo and Pappalardo, 2006) and the Moon (Garrick-Bethell et al., 2014).

1.3 Overview

Mass redistribution in a planet causes perturbations in its moment of inertia tensor, which cause variations in that planet's spin axis. This mass redistribution can arise from many sources, including mantle convection (Spada et al., 1992), glacial loading and unloading (Chen et al., 2013), and oceanic and atmospheric circulation (Munk and MacDonald, 1960). This dissertation focuses on true polar wander due to mantle convection, which has the largest and longest-period effect. We further the theory of true polar wander through scaling analyses, numerical modeling, and the development new techniques for paleomagnetic data analysis.

In Chapter 2 we consider the problem of TPW from the perspective of fluid dynamics. We present scaling analyses and numerical simulations of TPW due to mantle convection over a range of parameter space relevant to planetary interiors. For simple rotating convection, the most important parameters are the Rayleigh number, the rotation rate, and the size of relative density fluctuations (i.e. thermal expansivity times the temperature variations). We identify timescales for the growth of moment of inertia perturbations due to convection and for their relaxation due to true polar wander. These timescales, as well as the relative sizes of convective anomalies, control the rate and magnitude of TPW. This analysis also clarifies the nature of so called "inertial interchange" TPW events, and when they are likely to occur. Finally, we discuss implications for large-scale TPW in Earth's past.

In Chapter 3 we describe the development of numerical methods for geodynamic models with a free-surface boundary condition. Geodynamic simulations increasingly rely on simulations with a true free surface to investigate questions of dynamic topography, tectonic deformation, and global mantle convection. In particular, gravity and moment of inertia perturbations due to internal mantle density anomalies (crucial for TPW analyses) are modified by the deflections at a free surface. However, implementations of free surface boundary conditions have proven challenging from a standpoint of accuracy, robustness, and stability. In particular, time integration of a free surface tends to suffer from a numerical instability that manifests as sloshing surface motions, also known as the "drunken sailor" instability. This instability severely limits stable timestep sizes to those much smaller than could be used in geodynamic simulations without a free surface. Several schemes have been proposed in the literature to deal with these instabilities.

We analyze the problem of creeping viscous flow with a free surface and discuss the origin of these instabilities. We demonstrate their cause and how existing stabilization schemes work to damp them out. We also propose a new scheme for removing instabilities from free surface calculations. It does not require modifications to the system matrix, nor additional variables, but is instead an explicit scheme based on nonstandard finite differences. It relies on a single stabilization parameter which may be identified with the smallest relaxation timescale of the free surface.

We also discuss the implementation of a free surface in the open source, community based mantle convection software `ASPECT`.

In Chapter 4 we develop a new Bayesian statistical approach for analyzing paleomagnetic data. Apparent polar wander (APW) paths from paleomagnetic poles provide the most direct data for reconstructing past paleogeography and plate motions for times earlier than $\sim$200 Ma. Many of the proposed TPW events are from interpretations of paleomagnetic APW paths. However, it can be difficult to interpret APW paths in the presence of large errors, age uncertainties, and the lack of paleolongitude control in traditional paleomagnetic analysis. Approaches for dealing with the uncertainties and compiling paleomagnetic poles into a single APW path include spline fits and running means. We propose a new approach for interpretation of APW paths. It extends the paleomagnetic Euler pole analysis of Gordon et al. (1984) by placing it within the framework of a Bayesian inverse problem. This approach allows the natural incorporation of uncertainties in both pole position and age.

The resulting paleomagnetic Euler poles provide estimates for the total plate motions (not just the latitudinal components) as well as their uncertainties.

We show several example inversions on simple synthetic data to demonstrate the capabilities of the method. We apply this method to the Cenozoic APW path of Australia and to the Mesozoic Keweenawan Track of cratonic North America (Laurentia). The inversion for the Keweenawan track gives extremely rapid plate speeds, and we discuss the potential for TPW as an explanation.

Chapter 2

Rates of true polar wander on convecting planets

2.1 Introduction

A rotating, quasistatic body like a planetary mantle will tend to spin about the axis of its maximum moment of inertia. Convection in a planetary mantle continuously redistributes mass, which can change the moment of inertia tensor, necessitating a change in the spin axis of the planet to conserve angular momentum, a process known as true polar wander (TPW).

TPW was first considered in detail by Darwin (1887), and the theory has been subsequently developed by many (e.g. Munk and MacDonald, 1960; Goldreich and Toomre, 1969; Ricard et al., 1993). Despite this, the ability of internal mass anomalies to drive large-scale TPW remains controversial. Paleomagnetic data have been interpreted to require up to $3^\circ - 12^\circ$/Myr rates of TPW (Mitchell et al., 2011), but the ability of the mantle to respond at such rates has been questioned (Tsai and Stevenson, 2007).

The primary uncertainties in assigning a maximum TPW rate to a convecting planet are the size of convective anomalies, which drive the rotational adjustment, and the viscosity structure of the mantle, which retards it. These two uncertainties are not unrelated: they are both expected to be functions of the geometric and material properties of the mantle. As such, they do not vary independently, and first-order questions about the propensity for planets to experience TPW remain: how are rates of TPW expected to vary with the vigor of convection? Are other planetary bodies more or less likely than Earth to experience TPW? And are these rates expected to vary through Earth history?

These questions suggest that an approach rooted in dimensional analysis and fluid dynamics can clarify the rates and magnitudes of TPW. Most previous studies coupling mantle convection models to polar wander calculations have done so with prescribed density perturbations (e.g. Greff-Lefftz, 2004), or prescribed moment of inertia variations (e.g. Tsai and Stevenson, 2007; Creveling et al., 2012). Richards et al. (1999) coupled thermal convection models to a polar wander model, but did not address in detail the scaling relationships between the two.

Herein we perform a scaling analysis of rates of TPW for a minimal system of a rotating, convecting mantle, which we support with numerical simulations.

2.2 Rotational dynamics

2.2.1 The Liouville equation

Conservation of angular momentum for a torque-free system in a rotating reference frame requires

$$\frac{d\mathbf{H}}{dt} + \boldsymbol{\Omega} \times \mathbf{H} = 0 \tag{2.1}$$

where $\mathbf{H} = \mathbf{I} \cdot \boldsymbol{\Omega}$ is the angular momentum vector, $\mathbf{I}$ is the moment of inertia tensor, and $\boldsymbol{\Omega}$ is the angular velocity vector. On a dynamic planet $\mathbf{I}$ may be a function of time, so to conserve angular momentum $\boldsymbol{\Omega}$ must be also vary with time. In this case, Equation (2.1) is often called the Liouville equation (e.g. Munk and MacDonald, 1960). For a slowly convecting fluid, such as a planetary mantle, the inertial term $\partial\mathbf{H}/\partial t$ is negligible, so we may solve the simplified quasistatic equations

$$\boldsymbol{\Omega}(t) \times (\mathbf{I}(t) \cdot \boldsymbol{\Omega}(t)) = 0. \tag{2.2}$$

Equation (2.2) indicates that $\boldsymbol{\Omega}$ and $\mathbf{H}$ are parallel, so a solution for $\boldsymbol{\Omega}(t)$ is equivalent to solving an eigenvalue problem for $\mathbf{I}(t)$, where the eigenvectors correspond to the principal axes and the eigenvalues correspond to the principal moments (where the most stable orientation of the planet corresponds to rotating about the largest principal axis). In practice, this eigenvalue approach has been often used in previous studies for computing the spin axis of a planet (e.g. Steinberger and O'Connell, 1997; Roberts and Zhong, 2007). The moment of inertia tensor in Equation (2.2) includes all contributions to the mass structure of the planet, including the spherically symmetric mass distribution, rotational deformation, deformation due to self gravity, internal and surface density anomalies, and surface deflections due to density anomalies. Here we are interested in contributions from mantle convection, so we restrict our attention to these processes.

For mantle convection problems the moment of inertia tensor is commonly separated into three parts (Sabadini and Peltier, 1981; Spada et al., 1992):

$$I_{ij}(t) = I_0\delta_{ij} + J_{ij}(t) + E_{ij}(t) \tag{2.3}$$

where I_0 is the spherically symmetric reference moment, J_{ij} is the contribution due to rotational deformation, and E_{ij} is the contribution due to internal density anomalies, as well as the surface deflections caused by them. If we plug this decomposition into Equation (2.2) the spherically symmetric part $I_0\delta_{ij}$ drops out, and we are left with

$$\boldsymbol{\Omega} \times (\mathbf{J} \cdot \boldsymbol{\Omega}) = -\boldsymbol{\Omega} \times (\mathbf{E} \cdot \boldsymbol{\Omega}). \tag{2.4}$$

This form of the quasistatic Liouville equation makes clear that the polar wander problem represents a balance between the mismatches of the convective part of the moment of inertia ($\mathbf{E}$) and the rotational deformation part of the moment of inertia ($\mathbf{J}$). Our goal is to characterize this balance from a perspective of scaling and fluid dynamics.

2.2.2 A note on reference frames

True polar wander can be described in different reference frames, and this choice is fundamentally an arbitrary one. However, certain aspects of the physics can be made much simpler by an appropriate choice of the reference frame. In our treatment of TPW, we will refer to three different reference frames:

- First, there is the inertial, non-rotating frame corresponding to spatial coordinates that are fixed in time.
- Second, there is the body-fixed (or geographic) frame. By definition, the rotation of the body-fixed frame relative to the inertial frame is specified by $\mathbf{\Omega}$. A terrestrial no-net-rotation or hotspot reference frame are common choices for the body-fixed frame. Treatments of gravitational or rotational deformation of a planet are most naturally expressed in the body-fixed frame, as described in Section 2.2.3.
- Finally, there is the frame described by the principal axes of convective part of the moment of inertia $\mathbf{E}$, which we will refer to as the "$\mathbf{E}$-frame." Redistribution of mantle mass anomalies due to convection changes the principal axes of $\mathbf{E}$, causing the $\mathbf{E}$-frame to slowly rotate with respect to the geographic frame. We denote this drift by a rotation vector $\mathbf{\Psi}$ (see Section 2.4.2).

These reference frames and vectors are illustrated in Figure 2.1.

2.2.3 Rotational deformation

The part of the moment of inertia due to the elastic rotational deformation in the body-fixed frame is traditionally related to the degree-two part of the gravity field via MacCullagh's formula (Munk and MacDonald, 1960):

$$J_{ij} = \frac{ka^5}{3G}\left(\Omega_i\Omega_j - \frac{1}{3}\Omega_q\Omega_q\delta_{ij}\right) \tag{2.5}$$

where k is an elastic Love number, a is the semimajor axis of the planet, and G is the gravitational constant. This result may be extended to a viscoelastic rheology via the viscoelastic correspondence principle (e.g. Peltier, 1974):

$$J_{ij} = \frac{k(t)a^5}{3G} * \left(\Omega_i\Omega_j - \frac{1}{3}\Omega_q\Omega_q\delta_{ij}\right) \tag{2.6}$$

where k is now a time-dependent viscoelastic Love number which is convolved with the time-dependent rotation vector.

The infinite-time limit of Equation (2.6) for a constant rotation vector around the z-axis implies

$$\begin{aligned} J_{zz} = C &= \frac{2}{3}\frac{k_f a^5 \Omega^2}{3G} \\ J_{xx} = J_{yy} = A &= -\frac{1}{3}\frac{k_f a^5 \Omega^2}{3G} \end{aligned} \tag{2.7}$$

where C and A are the polar and equatorial moments of inertia, respectively, and k_f is the fluid limit of k. We can solve for k_f in terms of $C - A$:

$$k_f = \frac{3G(C-A)}{\Omega^2 a^5}. \tag{2.8}$$

This fluid-limit representation of the deformation does not allow for any disequilibrium between J_{ij} and E_{ij}, so it does not permit TPW.

Ricard et al. (1993) obtain an approximation to Equation (2.6) which retains its long-time behavior by entering the Laplace domain and truncating a Taylor series for $k(s)$ to first order. This introduces a new parameter, termed T_1, which can be seen as a weighted relaxation time for the system. This simple approximation in the Laplace domain allows for an analytical transformation back into the time domain, and neglecting second order terms in $\dot{\Omega}$ we find:

$$J_{ij} = \frac{k_f a^5}{3G}\left(\Omega_i\Omega_j - \frac{1}{3}\Omega_q\Omega_q\delta_{ij}\right) - \frac{k_f a^5 T_1}{3G}\left(\dot{\Omega}_i\Omega_j + \Omega_i\dot{\Omega}_j - \frac{2}{3}\Omega_q\dot{\Omega}_q\delta_{ij}\right). \tag{2.9}$$

The two terms of this equation have simple interpretations. The first term corresponds to the fluid limit of rotational deformation (in the absence of any long-term elastic strength). The second term represents the lag in the moment of inertia due to the viscous adjustment of the rotational bulge, where T_1 is the characteristic time constant for this adjustment. Since the first term represents the fluid limit of rotational deformation, it automatically satisfies Equation (2.2), and hence does not contribute to the polar wander problem.

2.2.4 The convective moment of inertia

The term on the right-hand side of Equation (2.4) represents the moment of inertia due to internal density anomalies as well as the surface deflections due to them. This part of the moment of inertia may also be parameterized using a viscoelastic Love number approach:

$$\mathbf{E} = \left[\delta(t) + k^L(t)\right] * \mathbf{C} \tag{2.10}$$

where k^L is an internal loading Love number representing the surface deflection due to density anomalies, and C_{ij} is the moment of inertia due solely to the internal load. Frequently the simplification is made that the timescale of the surface response is quick compared to the

true polar wander timescale, and we may use the fluid limit geoid kernels (e.g. Richards and Hager, 1984):

$$E_{ij} = (1 + k_f^L)C_{ij}. \tag{2.11}$$

An alternative to the Love number formalism is to calculate to surface deflections directly using mantle convection simulations with a true free surface boundary condition. In Chapter 3 we describe the implementation of a free surface boundary condition in the CIG-sponsored mantle convection software `ASPECT`. permits more general treatments of mantle rheology.

2.2.5 Rate of true polar wander

We are in a position to address the rates of true polar wander for a given convective moment $\mathbf{E}$. A considerable simplification occurs if we neglect secular changes in the rotation rate, and just consider changes in direction of the pole ($d\Omega^2/dt = 2\Omega_i\dot{\Omega}_i = 0$) Substituting Equation (2.9) into Equation (2.4) we find

$$\frac{k_f a^5 T_1 \Omega^2}{3G}\boldsymbol{\Omega} \times \dot{\boldsymbol{\Omega}} = \boldsymbol{\Omega} \times (\mathbf{E} \cdot \boldsymbol{\Omega}) \,. \tag{2.12}$$

Introducing a unit vector $\boldsymbol{\omega} = \boldsymbol{\Omega}/\|\boldsymbol{\Omega}\|$ and using Equation (2.8) for k_f, we may solve this equation for $\dot{\boldsymbol{\omega}}$:

$$\dot{\boldsymbol{\omega}} = \frac{1}{(C-A)T_1} \left[\mathbf{E} \cdot \boldsymbol{\omega} - (\boldsymbol{\omega} \cdot \mathbf{E} \cdot \boldsymbol{\omega})\, \boldsymbol{\omega}\right]. \tag{2.13}$$

Note that the quantity in brackets is similar in form to the shear stress on a plane in classical elastostatics. This correspondence permits useful insights (see below). Let $\dot{\Theta} = |\dot{\boldsymbol{\omega}}|$ denote the rate of polar wander. Evaluating the scalar product $\dot{\Theta}^2 = \dot{\boldsymbol{\omega}} \cdot \dot{\boldsymbol{\omega}}$ gives

$$\dot{\Theta}^2 = \dot{\boldsymbol{\omega}}^2 = \frac{1}{(C-A)^2 T_1^2} \left[(\mathbf{E} \cdot \boldsymbol{\omega})^2 - (\boldsymbol{\omega} \cdot \mathbf{E} \cdot \boldsymbol{\omega})^2\right]. \tag{2.14}$$

Our goal is to quantify the polar wander rate $\dot{\Theta}$ due to a convective perturbation $\mathbf{E}$ in the moment of inertia. The rate defined by Equation (2.14) is expressed in the body-fixed geographic frame, which is also the reference frame used to measure TPW. However, the physics of the right-hand-side of Equation (2.14) is more naturally expressed in the reference frame of the principal axes of $\mathbf{E}$. In general the $\mathbf{E}$-frame rotates slowly with respect to the geographic frame, so the time derivative of ω is different in these two frames. However, Equation (2.14) is a scalar equation, which means it is invariant to rotations. Therefore we can enter the coordinate system of the convective moment of inertia $\mathbf{E}$ with principal moments $\lambda_1 \leq \lambda_2 \leq \lambda_3$ and define the orientation of $\boldsymbol{\omega}$ in the $\mathbf{E}$-frame with colatitude θ and longitude ϕ (see Figure 2.1). Plugging this description of $\boldsymbol{\omega}$ into Equation (2.14), and after

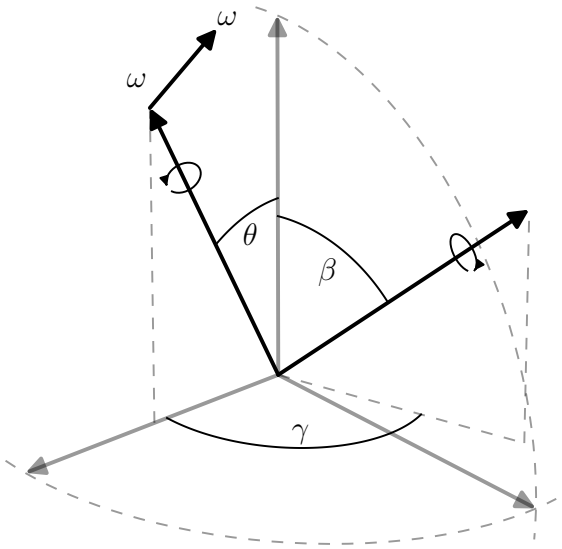

Figure 2.1: Relevant vectors and angles for the TPW analysis. The axes $\mathbf{e}_1$, $\mathbf{e}_2$, and $\mathbf{e}_3$ represent the principal axes of the convective moment of inertia $\mathbf{E}$, with associated eigenvalues λ_1, λ_2, and λ_3, respectively. Since the choice of geographic axes is arbitrary, we assume that at this instant the $\mathbf{E}$-frame and the geographic frames are colocated (though at future times they will not be). The angle θ represents the mismatch between the rotation axis $\boldsymbol{\omega}$ and the $\mathbf{e}_3$-axis. For illustration, we assume the longitude ϕ of the rotation axis is zero so $\boldsymbol{\omega}$ lies in the $\mathbf{e_1}$-$\mathbf{e_3}$ plane. True polar wander moves the rotation axis towards the $\mathbf{e}_3$-axis. We denote this motion by $\dot{\boldsymbol{\omega}}$ in the geographic frame. However, time-dependent convection in the mantle may cause a relative rotation between the geographic frame and the $\mathbf{E}$-frame. This relative rotation can be represented as a rotation around the axis $\boldsymbol{\Psi}$, which is defined by colatitude β and longitude γ. The rotation around the $\boldsymbol{\Psi}$ axis contributes to the motion of $\boldsymbol{\omega}$ as seen in the $\mathbf{E}$-frame. Further discussion of the reference frames and the relative rotation vector $\boldsymbol{\Psi}$ can be found in Sections 2.2.2 and 2.4.2

some tedious algebra, we find

$$\begin{aligned}\dot{\Theta}^2 =& \frac{1}{4(C-A)^2 T_1^2} \sin^2 2\theta \left[(\lambda_3-\lambda_1)^2 \cos^2\phi + (\lambda_3-\lambda_2)^2 \sin^2\phi\right] + \\ & \frac{1}{4(C-A)^2 T_1^2} \sin^4\theta \sin^2 2\phi \,(\lambda_2-\lambda_1)^2 \,. \end{aligned} \tag{2.15}$$

This equation is a version of what has been called the "Milankovitch theorem" (Munk and MacDonald, 1960). Two special cases of this equation are of note. First, if $\dot{\Theta}^2$ is evaluated on the octahedral plane (the plane with direction cosines all $1/\sqrt{3}$, or $\phi = 45°, \theta \approx 55°$, cf. Fung (1965)), then it can be expressed in terms of the second invariant (E_{II}) of the moment of inertia deviator ($E_{ij} - 1/3 E_{kk}\delta_{ij}$):

$$\begin{aligned}\dot{\Theta}^2 &= \frac{1}{9(C-A)^2 T_1^2}\left[(\lambda_3-\lambda_1)^2 + (\lambda_3-\lambda_2)^2 + (\lambda_2-\lambda_1)^2\right] \\ &= \frac{E_{\mathrm{II}}}{9(C-A)^2 T_1^2}. \end{aligned} \tag{2.16}$$

The second invariant of the stress deviator is commonly used in the theories of elasticity and plasticity as a convenient scalar approximation of the shear stress in a system. The second invariant of the moment of inertia deviator can be similarly viewed as a scalar estimate of the "rotational stress."

The second special case is if the rotation vector $\boldsymbol{\omega}$ lies in $\mathbf{e}_1$-$\mathbf{e}_3$ plane ($\phi = 0$). Then Equation (2.15) becomes significantly simpler, which is useful for scaling purposes:

$$|\dot{\Theta}| = \frac{1}{2(C-A)T_1} \sin 2\theta (\lambda_3 - \lambda_1). \tag{2.17}$$

The maximum true polar wander rate of the system is achieved when $\theta = 45°$ (see, e.g. Fung (1965)).

From Equation (2.17) it is clear that the important quantities for estimating the rate of true polar wander ($\dot{\Theta}$) are θ and the differences between the eigenvalues of the convective moment $\mathbf{E}$, both of which depend on the structure and dynamics of mantle convection. They represent, respectively, the angular mismatch between the rotation axis and the principal axis of the convective moment and the size of convective anomalies in the moment of inertia tensor. The dynamics of mantle convection affects the rate of TPW in two ways; it controls λ_i and it represents the mechanism that drives the angular mismatch. The value of θ at any time also depends on the relaxation of the rotation axis back toward the principal axis of $\mathbf{E}$. We focus on the dynamics of the convective contribution in the next section.

2.3 Internal dynamics

Mantle convection and rotational dynamics of planetary bodies are usually considered separately, yet the processes are based on a common set of governing equations. As such,

some extra care must be taken to ensure that the equations we consider are self-consistent. Furthermore, since our goal is to establish a scaling for TPW rate, we must identify a minimal set of nondimensional numbers which describe its physics. For simplicity we consider an isoviscous planet in a rotating reference frame with no internal heating in the incompressible Boussinesq approximation. The equations for mass, momentum, and energy then read

$$\nabla \cdot \mathbf{u} = 0 \tag{2.18}$$

$$-\nabla P + \eta \nabla^2 \mathbf{u} = \rho \mathbf{g} - \rho \boldsymbol{\Omega} \times \boldsymbol{\Omega} \times \mathbf{r} \tag{2.19}$$

$$\frac{\partial T}{\partial t} + \mathbf{u} \cdot \nabla T = \kappa \nabla^2 T \tag{2.20}$$

where $\mathbf{u}$ is the velocity, P is the pressure, and T is the temperature. The vector $\mathbf{g}$ is the gravitational acceleration, which defined in terms of a gravitational potential V by $\mathbf{g} = -\nabla V$. The gravitational potential obeys

$$\nabla^2 V = 4\pi G \rho. \tag{2.21}$$

where G is the gravitational constant. For the purposes of scaling, we assume that the magnitude of the gravitational acceleration, g_0, is the approximately constant (as is the case for Earth's mantle). In addition we use the simple equation of state

$$\rho = \rho_0 \left(1 - \alpha (T - T_0)\right). \tag{2.22}$$

to define the density. The remaining parameters are defined in Table 2.1. Note that here we retain the centrifugal term, which is normally either neglected or absorbed into a modified pressure (in the latter case the boundary conditions on P must be modified). The centrifugal term, although the largest of the terms neglected in typical mantle convection models, is generally small compared to gravitational forces (at least for Earth-like parameters), and likely does not have a strong influence on the style of convection. However, this term is critical for determining the size of the rotational bulge which must move relative to the mantle, and so we must include it to establish the connection between the linear and angular momentum equations.

Dimensional analysis of this system (cf. Barenblatt (1996)) requires four nondimensional numbers to characterize it (a fifth one, defined by the ratio of the length of day to a diffusion timescale, does not appear in the governing equations). Convenient choices for these numbers are listed in Table 2.2, along with approximate Earth-like values for them.

Two dimensionless parameters have a prominent role in our scaling analysis. The first is the Rayleigh number, which characterizes the vigor of convection. The second is the ratio of centrifugal to gravitational forces. This nondimensional number does not have a uniformly agreed-upon name: it has been called a Froude number in analogy with other applications of inertial-to-gravitational effects (McKenzie, 1968), and in the geodesy community has commonly been termed m (e.g. Nakiboglu, 1982; Chambat et al., 2010), which we adopt here.

Since we have begun with equations that do not have inertia or compressibility, we have implicitly thrown out the dependence on the nondimensional numbers that characterize those effects (e.g., the Prandtl and dissipation numbers). It would be straightforward to include them, but they do not affect the overall treatment of this scaling.

In this case, the dynamics can be characterized in terms of deviations from a reference hydrostatic state, which includes the dynamic pressure $P^* = P - P_0$ and density perturbations $\delta\rho = \rho - \rho_0 = -\rho_0\alpha(T - T_0)$. In addition, we expect deviations in the figure of the planet from its hydrostatic shape, which we denote by $V = V_H + \Delta V$, where V_H is the hydrostatic figure and ΔV is the deviation. Our rationale for this decomposition is simply that the hydrostatic pressure is most naturally defined in the (oblate) hydrostatic configuration. The introduction of ΔV requires another nondimensional number to characterize it, and we find that the quantity $\Gamma \equiv \alpha\Delta T$ is convenient. Finally, we define $\boldsymbol{\Omega} = \Omega_0\boldsymbol{\omega}$, where $\boldsymbol{\omega}$ is a unit vector in the direction of $\boldsymbol{\Omega}$.

By definition the hydrostatic reference state is a solution to Equation (2.19) where there is no flow:

$$-\nabla P_0 = \rho_0\mathbf{g} - \rho_0\boldsymbol{\Omega}\times\boldsymbol{\Omega}\times\mathbf{r}. \tag{2.23}$$

Nondimensionalizing with the parameters in Table 2.2 and removing the reference state we find the nondimensional momentum equation:

$$-\nabla P^* + \nabla^2\mathbf{u} - \mathrm{Ra}\, T\, \mathbf{g} + \mathrm{Ra}\, m\, T\, \boldsymbol{\omega}\times\boldsymbol{\omega}\times\mathbf{r} = 0. \tag{2.24}$$

We can explicitly draw the connection between the angular and linear momentum equations by returning to the dimensional Equation (2.19), crossing it with $\mathbf{r}$ and integrating over the volume of the mantle:

$$-\int_V \mathbf{r}\times\nabla P\, dV + \int_V \eta\mathbf{r}\times\nabla^2\mathbf{u}\, dV - \int_V \rho\mathbf{r}\times\mathbf{g}\, dV + \int_V \rho\mathbf{r}\times\boldsymbol{\Omega}\times\boldsymbol{\Omega}\times\mathbf{r}\, dV = 0. \tag{2.25}$$

The first three terms represent pressure, viscous torques, and gravitational torques on the mantle. Convection in the outer core, atmospheres, and oceans is not strong enough to provide significant pressure and viscous torques over geologic timescales, and a self-gravitating body cannot self-torque (Braginsky and Roberts, 1995). Therefore we can neglect those terms, and we are left with

$$\int_V \rho\mathbf{r}\times\boldsymbol{\Omega}\times\boldsymbol{\Omega}\times\mathbf{r}\, dV = 0 \tag{2.26}$$

which may be rewritten via the Jacobi identity to find

$$\boldsymbol{\Omega}\times\int_V \rho\mathbf{r}\times(\boldsymbol{\Omega}\times\mathbf{r})\, dV = 0. \tag{2.27}$$

This equation can be directly identified with Equation (2.2), and is a statement that a quasistatic body will rotate around the principal axis of its total moment of inertia.

Table 2.1: Parameters for rotating mantle convection

Symbol	Definition
R_i	inner radius
R	outer radius
G	gravitational constant
V	gravitational potential
M	mass of the planet
Ω_0	reference rotation rate
η	viscosity
κ	thermal diffusivity
α	thermal expansivity
g_0	reference gravity
I_0	reference moment of inertia
T_0	reference temperature
ρ_0	reference density
ΔT	temperature drop across mantle

We now seek to evaluate Equation (2.26) in the perturbed, convecting state. Hydrostatic balance (Equation (2.23)) ensures that the integral over the reference shape V_H vanishes when $\rho = \rho_0$. Nonzero contributions arise from perturbations in the density field or from perturbations in the shape. To make this dependence explicit, we split the shape into the reference volume V_H and perturbations from it ΔV, and use Equation (2.22) to define density perturbations. Substituting this decomposition into Equation (2.26) brings the integral into the form

$$\begin{aligned}\int_{V_H} \rho_0 \mathbf{r} \times \mathbf{\Omega} \times \mathbf{\Omega} \times \mathbf{r}\, dV + \int_{V_H} \rho_0 \alpha (T - T_0) \mathbf{r} \times \mathbf{\Omega} \times \mathbf{\Omega} \times \mathbf{r}\, dV + \\ \int_{\Delta V} \rho_0 \mathbf{r} \times \mathbf{\Omega} \times \mathbf{\Omega} \times \mathbf{r}\, dV + \int_{\Delta V} \rho_0 \alpha (T - T_0) \mathbf{r} \times \mathbf{\Omega} \times \mathbf{\Omega} \times \mathbf{r}\, dV = 0.\end{aligned} \tag{2.28}$$

As previously noted, the first term of this equation is zero due to the hydrostatic equation. The fourth term is negligible due to being second order in the smallness parameters $\Delta V / V_H$ and $\Gamma \equiv \alpha \Delta T$. Removing these, we find

$$\int_{\Delta V} \rho_0 \mathbf{r} \times \mathbf{\Omega} \times \mathbf{\Omega} \times \mathbf{r}\, dV = -\int_{V_H} \rho_0 \alpha (T - T_0) \mathbf{r} \times \mathbf{\Omega} \times \mathbf{\Omega} \times \mathbf{r}\, dV. \tag{2.29}$$

This equation may be identified with Equation (2.4), where disequilibrium in the rotational deformation (left side) is balanced by the mismatch of the convective moment of inertia with the spin axis (right side). Our goal is to identify characteristic sizes of these quantities, which must be functions of the nondimensional numbers identified in Table 2.2.

Table 2.2: Nondimensional numbers with approximate Earth-like values

Symbol	Name	Definition	Approximate value
Ra	Rayleigh	$\rho_0 g_0 \alpha \Delta T R^3/\eta\kappa$	10^7
m	Froude	$\Omega_0^2 R/g_0 = \Omega_0^2 R^3/GM$	10^{-3}
A	aspect ratio	R_i/R	0.54
Γ	density deficit	$\alpha\Delta T$	10^{-2}

2.4 Scaling

Having drawn the connection between the angular momentum equation (Section 2.2) and the linear momentum equation (Section 2.3), we would like to apply the scaling of the linear momentum equation to the problem of TPW. We would therefore like to rewrite Equation (2.17) in terms of the nondimensional numbers identified in Section 2.3. Specifically, we will need estimates for $(C-A)$, T_1, $(\lambda_3 - \lambda_1)$, and θ.

It is useful to define a nondimensional eigenvalue difference, which may also be described as a normalized "eigengap": $\Lambda_{ij} \equiv (\lambda_i - \lambda_j)/I_0$. This quantity represents the size of fluctuations in the convective moment of inertia compared to the reference value. The difference in the polar and equatorial moments of the hydrostatic planet $(C-A)$ is proportional to the ratio of rotational to gravitational forces (Munk and MacDonald, 1960):

$$(C-A) \sim I_0 m. \tag{2.30}$$

The time constant T_1 is a viscous relaxation time of the planetary mantle. It is frequently represented as a weighted average of the different relaxation modes (e.g. Ricard et al., 1993; Greff-Lefftz, 2004), but for our purposes it is enough to approximate it as a single mode:

$$T_1 \sim \frac{\eta}{\rho_0 g_0 R} = \frac{R^2}{\kappa}\frac{\Gamma}{\mathrm{Ra}}. \tag{2.31}$$

Plugging these scalings into Equation (2.17) we find

$$\frac{\kappa}{R^2}\,\dot{\Theta} \sim -\frac{\mathrm{Ra}}{\Gamma m}\Lambda_{31}\sin 2\theta. \tag{2.32}$$

At this point we do not have estimates for the characteristic magnitudes of Λ_{ij} or θ, both of which are crucial for predicting characteristic rates of TPW. They represent, respectively, the size of convective anomalies in the moment of inertia tensor and the angular mismatch between the rotation axis and the principal axis of the convective moment.

The quantity Λ_{ij} should be a function of our nondimensional parameters Ra, m, and Γ. Similarly, the convective forcing that drives changes in θ must also be a function these nondimensional parameters. To be explicit in our discussion, we denote the angular velocity induced by forcing by Ψ (see Figure 2.1). We consider relatively slowly rotating bodies here ($m \ll 1$), and so make the simplifying assumption that the rotation does not significantly affect the style of convection. In this regime, therefore, we neglect the dependence on m, and look for scalings of the form $\Lambda_{ij}(\mathrm{Ra}, \Gamma)$ and $\Psi(\mathrm{Ra}, \Gamma)$.

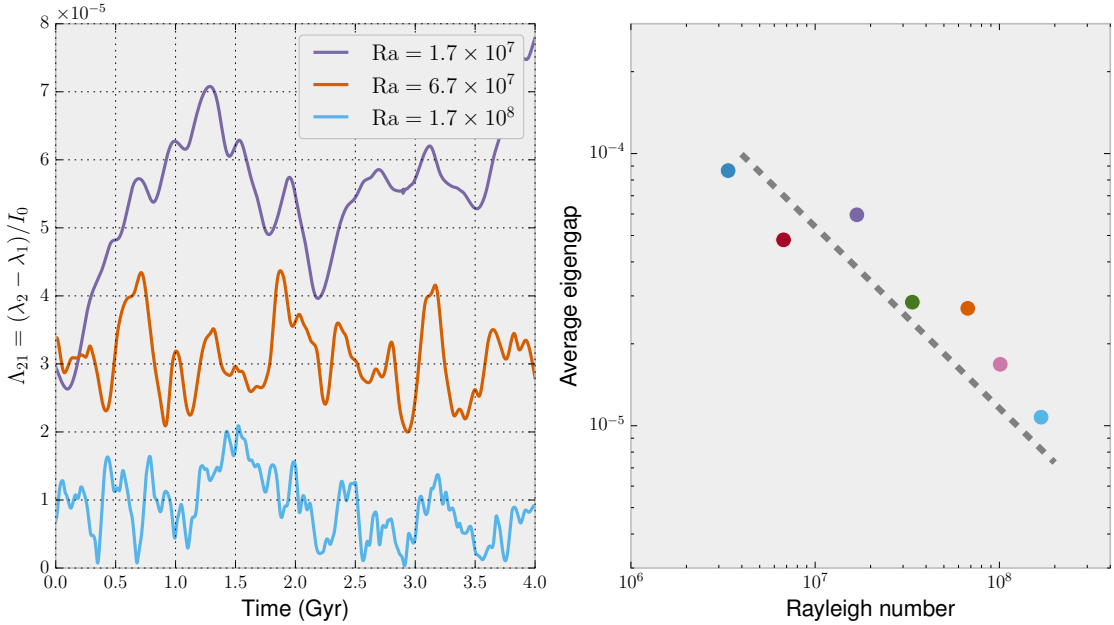

Figure 2.2: Left: Time series of the normalized difference between moments $\Lambda_{21} = (\lambda_2 - \lambda_1)/I_0$ for convection in a 2D annulus at several different Rayleigh numbers. As the Rayleigh number increases, the average value of the relative moment decreases due to less low-degree coherence in the temperature structure. Right: average value of Λ_{21} for the different Rayleigh numbers. Also shown is a line with slope $\mathrm{Ra}^{-2/3}$, which is predicted from the scaling analysis (the exponent is $-2/3$ instead of -1 due to the reduced dimensionality of the simulations).

2.4.1 An estimate for Λ_{ij}

Fluctuations in the nonhydrostatic moment of inertia are caused by density variations due to the temperature fluctuations in the mantle and their spatial structure:

$$C_{ij} = \int_{V_H} \rho_0 \alpha (T - T_0) \left(r_q r_q \delta_{ij} - r_i r_j \right) \, dV \tag{2.33}$$

As discussed in Section 2.2.4, these internal density loads may be convolved with their surface responses to get the convective moment of inertia E_{ij}. The surface response is a function of the viscosity structure of the planet and the wavelength and depth of the internal load. The factor $(1+k_f^L)$ is generally an order-one parameter (strictly speaking, dynamic compensation usually makes it less than one, (e.g. Richards and Hager, 1984)). For the purposes of scaling, it is reasonable to neglect this multiplicative factor.

For thermal convection, the convective part of the moment of inertia E_{ij} is directly related to the degree-two part of the temperature field (see Appendix 2.A). Therefore, an estimate for one specifies the other. We can expand the temperature structure of the convecting planet with a set of orthonormal basis functions $R_n Y_{lm}$, where Y_{lm} are spherical harmonics, R_n are some set of orthogonal radial polynomials, and T_{nlm} are the coefficients for the expansion

which have been normalized by ΔT:

$$T(r,\theta,\phi,t) = \Delta T \sum_{n=0}^{\infty} \sum_{l=0}^{\infty} \sum_{m=-l}^{l} T_{lmn}(t) R_n(r) Y_{lm}(\theta,\phi). \tag{2.34}$$

Inserting the temperature expansion (2.34) into Equation (2.33) results in a prefactor of the nondimensional number $\Gamma = \alpha \Delta T$. Orthogonality of the basis functions for the expansion means that the integral for C_{ij} picks out degree-two spherical harmonics in the lateral dimensions, and only the lowest few radial functions $R_n(r)$. Therefore, of the entire temperature spectrum, only a few of the modes matter for TPW. We want to estimate the power in those few modes, which we denote by $T_{\text{degree-two}}$ (see Appendix 2.A for more detail):

$$\Lambda_{31} \sim \Gamma T_{\text{degree-two}}. \tag{2.35}$$

The temperature field has been normalized by ΔT and thus goes between zero and one, therefore the expansion in T_{lmn} is constrained by

$$\max \left(\sum_{n=0}^{\infty} \sum_{l=0}^{\infty} \sum_{m=-l}^{l} T_{lmn}(t) R_n(r) Y_{lm}(\theta,\phi) \right) = 1. \tag{2.36}$$

This is a strong constraint, but it gives very little information about the distribution of power across the T_{lmn}. We can, however, think about the power spectrum in two different regimes: that of steady/quasisteady flow, (relatively low Ra) and that of chaotic flow (relatively high Ra). The structure of thermal convection is primarily controlled by the Rayleigh number. Once the Rayleigh number is sufficiently high ($\sim 10^6$) the style of convection changes from steady/quasisteady to chaotic. Accompanying this transition to chaos is a broadening of the spatial and temporal spectra (McLaughlin and Orszag, 1982).

At low Rayleigh number we expect the spectrum of the temperature field to be dominated by only a few low-degree modes which are largely influenced by the aspect ratio. This spectrum may or may not have a lot of power in the degree-two modes, and does not depend strongly on time.

At high Rayleigh number we expect the shortest lengthscales to be limited by the effects of thermal diffusion, which tends to wipe out thermal heterogeneity at small scales. Consequently, there will be little power in modes with shorter lengthscales than that allowed by diffusion. Therefore we expect, to a good approximation, that the infinite sum in Equation (2.34) can be truncated at some maximum wavenumber, set by the smallest lengthscale d:

$$n_{\max}, l_{\max}, m_{\max} \sim \frac{R}{d}. \tag{2.37}$$

Strictly speaking, convective mixing can produce smaller scales, but the power in these scales is greatly reduced by diffusion. Thus total number of modes that are accessible to the system are

$$N_{\text{modes}} = n_{\max} \times l_{\max} \times m_{\max} \sim \left(\frac{R}{d} \right)^3. \tag{2.38}$$

The value of each $T_{lmn}(t)$ will in general be some complex function of time, but for a given style of convection we expect there to be some average value. For chaotic flow the power should be spread out amongst the modes accessible to it. We may make the hypothesis that each of the modes are roughly as likely as any of the others, which implies

$$T_{\text{degree-two}}(t) \sim \frac{1}{N_{\text{modes}}} \sim \left(\frac{d}{R}\right)^3. \tag{2.39}$$

Any of a number of scaling laws can provide an estimate for the characteristic length scale of a convecting system which may depending on rheology, geometry, or density structure. The simplest, based on boundary layer theory (Turcotte and Oxburgh, 1967), finds $d/R \sim \text{Ra}^{-1/3}$. This scaling is roughly a measure of the diffusive lengthscale for the timescale of a convective overturn, consistent with the cutoff in Equation (2.37). It thus furnishes us with an estimate of the power in the degree-two part of the field as a function of Rayleigh number:

$$T_{\text{degree-two}}(t) \sim \text{Ra}^{-1}. \tag{2.40}$$

We performed a series of numerical simulations of mantle convection at different Rayleigh numbers to test this scaling. We used the mantle convection software `ASPECT` (Kronbichler et al., 2012), based on the finite element library `deal.II` (Bangerth et al., 2015a), which allows for flexible implementation of different rheologies, geometries, and postprocessors. In order to test a wide range of Rayleigh numbers, we ran the simulations in a 2D annulus, tracking the eigenvalues of the moment of inertia tensor and integrating Equation (2.13) in time. For the 2D simulations there is a reduced dimensionality when calculating the number of modes, so $N_{\text{modes}} \sim (R/d)^2$. This leads us to a scaling of $T_{\text{degree-two}} \sim \text{Ra}^{-2/3}$, which is shown as a dashed line in Figure 2.2. This result has a simple interpretation. As the Rayleigh number of the system increases, the smallest lengthscale of convective features gets smaller. The total power in the temperature field is spread across a larger spectrum, leaving less total power for the degree-two part, which is what drives TPW.

With an estimate for the power in the degree-two part of the temperature field, we may finally estimate Λ_{ij}:

$$\Lambda_{ij} \sim \frac{\Gamma}{\text{Ra}}. \tag{2.41}$$

Other power spectra for the temperature field are possible. Isoviscous models tend to be "bluer," (dominated by small wavelengths) and models with viscosity stratification tend to be "redder" (dominated by long wavelengths) (Richards et al., 1999). Present day Earth seems to have a fairly "red" spectrum, with large low-degree seismic anomalies due to Cenozoic subduction history and the lower mantle LLSVPs (Dziewonski et al., 2010). Nevertheless, at high Rayleigh number the expectation is that the power will be distributed across many length scales.

2.4.2 An estimate for the angular mismatch angle (θ)

Convection can drive both growth and decay in the mismatch angle (θ) between the current rotation axis and the principal axis of the convective moment. This parameter is crucial for the rate of TPW, as previously noted in Equation (2.32). Much of the debate around the existence and magnitude of TPW on Earth comes down to the question of how big θ can be (Kirschvink et al., 1997; Steinberger and O'Connell, 1997).

Two processes control the evolution of θ. Its growth occurs through perturbations in the convective moment and its decay occurs by relaxation of the pole towards the maximum moment of inertia. We can explore these two effects by converting Equation (2.13) from the body-fixed frame to the **E**-frame (recall that $\mathbf{\Omega}$ defines the rotation of the body-fixed frame relative to inertial space in Equation (2.1)). The **E**-frame rotates slowly with respect to the geographic frame, which we describe by the rotation vector $\mathbf{\Psi}$. (To be explicit in our discussion we let $\mathbf{\Psi}$ define the rotation of the **E**-frame in the geographic frame, although this choice is arbitrary as long as we are consistent). The time derivatives of $\boldsymbol{\omega}$ in the two frames are related by

$$\dot{\boldsymbol{\omega}} = \dot{\boldsymbol{\omega}}' + \mathbf{\Psi} \times \boldsymbol{\omega}'. \tag{2.42}$$

where primes are used to define quantities in the **E**-frame. Rearranging gives

$$\dot{\boldsymbol{\omega}}' = \dot{\boldsymbol{\omega}} - \mathbf{\Psi} \times \boldsymbol{\omega}'. \tag{2.43}$$

We now substitute for $\dot{\boldsymbol{\omega}}$ from Equation (2.13), making the additional assumption that the geographic and **E**-frames are momentarily aligned. This assumption is not a serious restriction because our goal is simply to relate the time derivatives of $\boldsymbol{\omega}$ in the two frames, rather than track the evolution of $\boldsymbol{\omega}$ over time. The expression for $\dot{\boldsymbol{\omega}}$ becomes

$$\dot{\boldsymbol{\omega}}' = \frac{1}{(C-A)T_1}\left[\mathbf{E}' \cdot \boldsymbol{\omega}' - (\boldsymbol{\omega}' \cdot \mathbf{E}' \cdot \boldsymbol{\omega}')\,\boldsymbol{\omega}'\right] - \mathbf{\Psi} \times \boldsymbol{\omega}'. \tag{2.44}$$

The advantage of expressing the rate of TPW in the **E**-frame is that the entire equation may be written in terms of the principal moments λ_i and the angles from the principal axes. As in Equation (2.17), we make the simplifying assumption that $\boldsymbol{\omega}'$ lies in $\mathbf{e}_1' - \mathbf{e}_3'$ plane (as shown in Figure 2.1). In this case the orientation of $\boldsymbol{\omega}'$ is defined by colatitude θ and longitude $\phi = 0$. The colatitude θ is precisely the angular misalignment that specifies the rate of TPW in Equation (2.17). We furthermore specify the orientation of Ψ using colatitude β and longitude γ (see Figure 2.1).

The time derivative of the unit vector $\boldsymbol{\omega}'$ defines the changing orientation of the rotation axis in the **E**-frame. We can express this changing orientation in terms of changes in angles θ and ϕ. The change in colatitude is

$$\dot{\theta} = -\frac{1}{2(C-A)T_1}\sin 2\theta(\lambda_3 - \lambda_1) - |\mathbf{\Psi}|\sin\beta\sin\gamma. \tag{2.45}$$

where $\mathbf{\Psi}$ is expressed in terms of its amplitude $|\mathbf{\Psi}|$ and its orientation angles β and γ. Equation (2.45) captures the essential competition between growth and decay of the mismatch

angle. The first term acts to reduce θ via TPW, while the second term can increase (or decrease) it via relative motion between the geographic frame and the principal axes of the **E**-frame. Comparison with Equation (2.17) shows that, when $|\boldsymbol{\Psi}|$ is zero, then the rate of TPW $|\dot{\Theta}|$ is identical to $|\dot{\theta}|$. Conversely, when the rate of TPW is very slow (i.e. $|\dot{\Theta}| \sim 0$), then $|\dot{\theta}| \sim |\boldsymbol{\Psi}|$, so the evolution of θ is driven mostly by $\boldsymbol{\Psi}$. For the purposes of scaling we will omit the orientation factor $\sin\beta \sin\gamma$ and focus on $|\boldsymbol{\Psi}|$. In order for the TPW rate to be large, the growth of θ via $|\boldsymbol{\Psi}|$ must, at least occasionally, be larger than its decay.

An estimate for $|\boldsymbol{\Psi}|$ must concern the stability of the convective moment of inertia. Convection is continuously redistributing mass throughout the mantle, which will perturb the convective moment of inertia. If the convective moment is stable to small perturbations, then $|\boldsymbol{\Psi}|$ should be small, so θ will never have the opportunity to grow. However, if **E** is not stable to perturbations, then $|\boldsymbol{\Psi}|$ can be large and θ can grow up to 90°. Given a random perturbation to **E**, we would like to give a bound on the size of changes in the orientation of the principle axes. This may be done by application of a theorem due to Davis and Kahan (1970).

Let δ be the size of the perturbation to the convective moment of inertia tensor after some time interval Δt, and let $\lambda_3 \geq \lambda_2 \geq \lambda_1$ be the eigenvalues of that tensor. The corresponding rotation of the principal axes is defined by the angle ξ. A bound on ξ is given by

$$|\sin(2\xi)| \leq \frac{2|\delta|}{\min\limits_{i \neq j} |\lambda_i - \lambda_j|}. \tag{2.46}$$

That is to say, if there is a large difference between the eigenvalues, this stabilizes axes to perturbations. If, however, there is a small difference between the eigenvalues (i.e., they are nearly degenerate), then perturbations can cause large rotations of the principal axes. This is illustrated schematically in Figure 2.3. Evans (1998) described a situation where the convective moment of inertia of Earth is prolate, with the maximum and intermediate moments of inertia nearly equal. He argued that perturbations in this case would result in TPW paths that are approximately on the great circle path between the intermediate and maximum axes. This behavior is a consequence of the instability described in Equation (2.46).

We may arrive at a simple estimate for $|\boldsymbol{\Psi}|$ by differentiating Equation (2.46), tentatively holding $|\lambda_i - \lambda_j|$ fixed:

$$|\boldsymbol{\Psi}| \sim |\dot{\xi}| \leq \frac{|\dot{\delta}|}{\min\limits_{i \neq j} |\lambda_i - \lambda_j|}. \tag{2.47}$$

As noted previously, $|\boldsymbol{\Psi}| \sim |\dot{\theta}|$ when the rate of TPW is small and the angular misalignment θ is small. Consequently, we can interpret Equation (2.47) as a bound on how fast θ can grow.

The quantity $(\lambda_i - \lambda_j)$ which appears in the denominator of these equations is precisely the same as the quantity which we estimated in the previous section to scale with $\sim \mathrm{Ra}^{-1}$. Therefore, as the Rayleigh number increases, the characteristic gap between the eigenvalues of the convective moment becomes smaller. Additionally, the timescale of fluctuations in

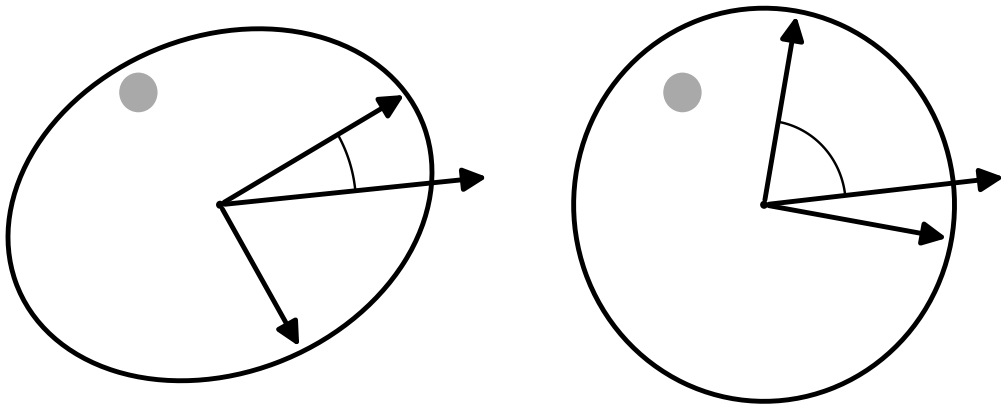

Figure 2.3: Graphical demonstration of the $\sin 2\xi$ theorem of Davis and Kahan (1970). Two spheroidal bodies with eigenvalues $\lambda_2 > \lambda_1$ start out with the rotation axis Ω aligned with the λ_2 axis. However, on the left the eigengap $\|\lambda_2 - \lambda_1\|$ is large, while on the right it is small. A negative mass perturbation is instantaneously added to both bodies, which effects a small rotation of the principal axes on the left, but a large one on the right.

these values goes down. Overall, this makes the principal axes of high Rayleigh number systems much less stable. This is consistent with the result of Richards et al. (1999).

In the limit that the eigengap becomes zero, the rotation of the principle axes can be arbitrary. This essentially corresponds to the hypothesized "inertial interchange true polar wander" (Kirschvink et al., 1997), where the mismatch angle is 90°. However, the eigengap does not need to be zero for there to be large displacements polar wander, and if it does go to zero, the wander does not need to be 90°.

Figure 2.4 shows a representative timeseries for annular convection, where we track the eigenvalues of the moment of inertia and integrate Equation (2.13) in time. Since it is a 2D model, the spin axis may be represented by a single angle. When the eigengap gets small, the misfit angle becomes much larger, and the rate of polar wander becomes much faster. At ∼1 Gyr into the model run the eigengap goes to zero, and the misfit angle goes to approximately 90°, an IITPW event. But there are several other events where the eigengap becomes small, and there are still large TPW events associated with them. For example, at ∼0.3 Gyr the eigengap dips, with an associated large TPW event, even though there is technically no interchange of the axes.

We suggest, then, that 90° IITPW events are simply a special case of a broad class of events which can occur when the principal moments are close to each other. Furthermore, a more vigorously convecting planet is much more likely to experience rapid TPW events as it has a lower characteristic gap between principal moments and the gap is much more likely to go to zero.

Tsai and Stevenson (2007) suggested that interchanges in the principal moments are unlikely to produce large TPW events, since (1) during an inertial interchange the total moment of inertia anomaly is small, and (2) the TPW event can only asymptotically approach 90°. This is true for the case of a single interchange. However, we argue that this is overly restrictive for our generalization of IITPW. Our numerical experiments show that in a vigorously convecting system the principal moments can interchange, or almost interchange, quite rapidly, and the perturbation sizes can be large soon after an interchange. Furthermore, the location of the principal axes need not stay put during a TPW event, which can lead to extended polar wandering of distances greater than 90°.

2.5 Discussion

The preceding results clarify the complex relationship between the Rayleigh number, m, and the rates of TPW for a convecting planet. As mantle convection redistributes mass in the planet's interior, the spin axis moves around to stay aligned with the principal axes of the convective moment of inertia. There is a constant competition between growth of the mismatch angle θ through Equation (2.47) and its relaxation through TPW. Goldreich and Toomre (1969) envisioned an analogy of beetles crawling on the surface of the globe, with the spin axis trying to keep up with the instantaneous figure axis set by the beetles. Our analysis begins to answer the questions "how big are the beetles?" and "how fast are they

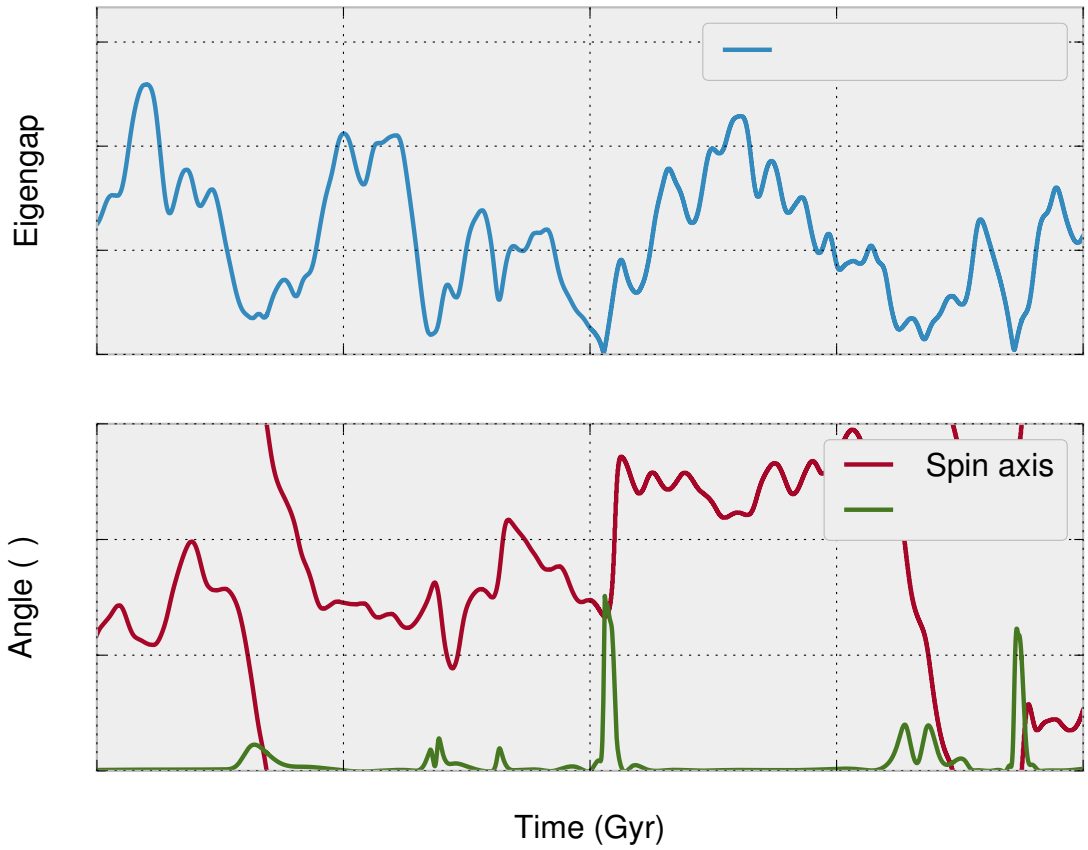

Figure 2.4: Top: Time series of principal moments for 2D annular convection at Ra $\sim 10^8$. Bottom: Time series of spin axis and mismatch angle θ. When the two moments are close to each other (small eigengap), the mismatch angle becomes large, and the rate of polar wander is significantly larger. At ∼1 Gyr the gap goes to zero and there is a nearly 90° TPW event, with $\sim 80°$ degrees of polar wander in ∼30 Myr. However, there are several other large TPW events which happen when the eigengap is small.

crawling?"

We may plug in the estimate for Λ_{ij} (Equation (2.41)) into Equation (2.17) to find the strikingly simple expression

$$\frac{\kappa}{R^2}\,\dot{\Theta} \sim -\frac{1}{m}\sin 2\theta. \tag{2.48}$$

Surprisingly, Γ and Ra have completely dropped from the prefactor in the scaling. Response timescales for relaxation of the mismatch angle go down at high Rayleigh numbers. At the same time, however, coherence in the temperature structure goes down, reducing the amount of power in the degree-two part of the field responsible for driving TPW. That these two effects cancel is something of a coincidence due to the simple estimate of the smallest lengthscales of the problem. Scalings for lengthscales of convection in fluids with temperature dependent viscosity (e.g. Solomatov, 1995) or pseudoplastic rheology (e.g. Korenaga, 2010) have different functional dependencies on Ra or additional nondimensional parameters. However, a common feature in most scalings is that typical lengthscales are still some power-law of Rayleigh number $d \propto \mathrm{Ra}^{-\beta}$. With this form, our scaling for TPW rate has the following dependence on Ra:

$$\frac{\kappa}{R^2}\,\dot{\Theta} \sim -\frac{\mathrm{Ra}^{1-3\beta}}{m}\sin 2\theta. \tag{2.49}$$

In general, β is some small number between one-fourth and one-third, so we expect that more complicated estimates for $d(\mathrm{Ra})$ will still result in a weak dependence of the prefactor in Equation (2.49) on the Rayleigh number.

We then suggest that the most important parameters are m, which acts as the brakes on the system, and the mismatch angle θ. Whereas the prefactor $\mathrm{Ra}^{1-3\beta}$ in Equation (2.49) has a weak dependence on Ra, the misalignment angle θ is expected to be strongly dependent on it.

Indeed, we can identify two endmember behaviors of Equation (2.49). When convection is not sufficiently chaotic to create a large θ we are in the regime where the planet's rotation axis closely tracks that of the convective moment. This is the regime considered in Steinberger and O'Connell (1997), Roberts and Zhong (2007), and Zhong et al. (2007), and can be considered the "slow TPW" regime. When convection is more chaotic, however, there may be large excursions in θ, which are driven by large values for $|\mathbf{\Psi}|$ when $(\lambda_i - \lambda_j)$ is small, according to Equation (2.47). In this case a dramatic increase in the rate of TPW is possible. If $\theta = 90°$, this corresponds to IITPW (Kirschvink et al., 1997). This, however, is a special case in the large θ, "fast TPW" regime.

As an example, we may consider the early Earth, when the mantle was presumably hotter and less viscous, leading to a higher Rayleigh number. We would then predict that convection was more vigorous, leading to a less stable $\theta(t)$, and thus more TPW and more frequent "fast TPW" events.

For Cenozoic Earth we can substitute direct estimates of the important parameters into Equation (2.17). Typical values for the time constant T_1 are of order 30 kyr (Ricard et al., 1993). Estimates of the present day non-hydrostatic moment of inertia (due to mantle

density anomalies, corresponding to $\Lambda_{31} I_0$ in the preceding scaling) are in the neighborhood of $10^{-5} I_0$, while the hydrostatic moment of inertia (corresponding to $C - A$) is $3 \times 10^{-3} I_0$ (Chambat and Valette, 2001). A key question is whether convection is sufficiently chaotic to enter the large θ regime. Richards et al. (1997) have argued that the convective planform of Earth has been stable for the last few hundred million years. On the other hand, we know that there have been large reorganizations of that planform during Earth history, so this recent geologic stability may not hold in general (Evans, 2003). Our numerical simulations show that large values for θ are possible in a vigorously convecting mantle. Allowing for such a large mismatch angle ($\theta = 45°$) we may estimate the maximum polar wander rate

$$\max(\dot{\Theta}) = \frac{(\lambda_3 - \lambda_1)}{(C - A)} \frac{1}{T_1} \sim 6°/\text{Myr}, \tag{2.50}$$

which corresponds to about 66 cm/yr 90° from the TPW axis. This is similar to the rates discussed by Cambiotti et al. (2011), (though our rate is larger since we allow for the possibility of a larger mismatch angle), and is within the range suggested by some interpretations of paleomagnetic data. The bulk viscosity of Earth's mantle is uncertain by up to a factor of ten (Mitrovica and Forte, 2004), which results in a corresponding uncertainty for the relaxation time T_1 and the maximum polar wander rate.

Thus far we have restricted our discussion to planets with lithospheres lacking long-term elastic strength. For this case the long-time limit of the planetary figure is coaxial with the convective moment of inertia. This assumption is not necessarily true in all cases. Earth's lithosphere is pervasively fractured and hydrated, and may not have much strength when subjected to rotational changes on geologic timescales. However, a planet with a stagnant lid (such as Mars) may have considerable strength, preventing the figure of the planet from reaching the fluid limit of Equation (2.8).

The theory of TPW response for the case of elastic lithospheres has been developed in, among other places, Matsuyama et al. (2006), Creveling et al. (2012), and Chan et al. (2014). The formalism developed in Section 2.4 can still be applied to this case, though the response to internal variations in the moment of inertia becomes more limited (and potentially richer, as in the oscillatory motions suggested by Creveling et al. (2012)).

2.6 Conclusion

We have developed a framework for discussing the rates of true polar wander for a convecting planet from a perspective of scaling and fluid dynamics. We identified a small number of dimensionless parameters which describe the system, and showed how they affect the overall dynamics of the system.

The most important parameters are the Rayleigh number and m, which acts as a damper to TPW. The dependence on the Rayleigh number is more complicated, since it is a control on both the forcing of TPW and the response, which act in opposite directions. Overall, however, we expect that more vigorously convecting planets should be less rotationally stable, and experience more TPW. This perspective allows us to consider not only the polar

wandering of Phanerozoic Earth, but also allows us to hypothesize about polar wandering during the Archean and Proterozoic, or on other planetary bodies.

2.A Degree-two moments

There is a connection between the moment of inertia of a rotating object and the degree-two density structure. The moment of inertia tensor may be written in index notation

$$I_{ij} = \int_V \rho \left(r_q r_q \delta_{ij} - r_i r_j \right) dV \tag{2.51}$$

where $\mathbf{r}$ is the Eulerian coordinate, ρ is the density, and V is the volume of the material. It is useful to enter the principal axes of the moment of inertia:

$$\mathbf{I} = \mathbf{1} \begin{bmatrix} \lambda_1 \\ \lambda_2 \\ \lambda_3 \end{bmatrix} = \mathbf{1} \begin{bmatrix} \int_V \rho(y^2 + z^z) dV \\ \int_V \rho(x^2 + z^2) dV \\ \int_V \rho(x^2 + y^2) dV \end{bmatrix} \tag{2.52}$$

where $\mathbf{1}$ is the identity matrix, and λ_1, λ_2, and λ_3 are the principal moments. From Equation (2.15) we see that the important quantities are the differences between the principal moments, $(\lambda_3 - \lambda_1)$, $(\lambda_3 - \lambda_2)$ and $(\lambda_2 - \lambda_1)$. These quantities may be rewritten in terms of degree-two real spherical harmonics (e.g. Dahlen et al., 1999). The relevant (fully normalized) harmonics are, in Cartesian coordinates:

$$\begin{aligned} Y_{20} &= \frac{1}{4}\sqrt{\frac{5}{\pi}} \frac{2z^2 - x^2 - y^2}{r^2} \\ Y_{22} &= \frac{1}{4}\sqrt{\frac{15}{\pi}} \frac{x^2 - y^2}{r^2}. \end{aligned} \tag{2.53}$$

Solving for $(\lambda_i - \lambda_j)$ in terms of these harmonics, we find

$$\begin{aligned} (\lambda_2 - \lambda_1) &= 4\sqrt{\frac{\pi}{15}} \int_V \rho r^2 Y_{22} \, dV \\ (\lambda_3 - \lambda_1) &= 2\sqrt{\frac{\pi}{15}} \int_V \rho r^2 \left(Y_{22} - \sqrt{3} Y_{20} \right) dV \\ (\lambda_3 - \lambda_2) &= -2\sqrt{\frac{\pi}{15}} \int_V \rho r^2 \left(Y_{22} + \sqrt{3} Y_{20} \right) dV. \end{aligned} \tag{2.54}$$

Up to the normalization constants, these expressions are identical to multipole expansions, picking out the degree-two part of the density field laterally, and low-order polynomials radially. When density is a function of temperature, we can insert the equation of state, Equation (2.22), into Equation (2.54) and integrate over a reference spherical volume V_S.

This allows us to drop the terms which integrate to zero due to the orthogonality of spherical harmonics, and we are left with:

$$\begin{aligned}(\lambda_2 - \lambda_1) &= -4\sqrt{\frac{\pi}{15}}\alpha\rho_0 \int_{V_S} Tr^2 Y_{22}\, dV \\ (\lambda_3 - \lambda_1) &= -2\sqrt{\frac{\pi}{15}}\alpha\rho_0 \int_{V_S} Tr^2 \left(Y_{22} - \sqrt{3}Y_{20}\right) dV \\ (\lambda_3 - \lambda_2) &= 2\sqrt{\frac{\pi}{15}}\alpha\rho_0 \int_{V_S} Tr^2 \left(Y_{22} + \sqrt{3}Y_{20}\right) dV.\end{aligned} \tag{2.55}$$

We normalize the differences in eigenvalues by the reference moment I_0:

$$I_0 = \frac{2}{3}\int_{V_S} \rho_0 r^2\, dV. \tag{2.56}$$

Dividing Equation (2.55) by I_0 and nondimensionalizing the integrals results in a factor of $\Gamma = \alpha\Delta T$ and a normalized set of degree-two coefficients for the temperature field, which we abbreviate as $T_{\text{degree-two}}$:

$$\Lambda_{ij} \sim \Gamma T_{\text{degree-two}}. \tag{2.57}$$

2.B Derivation of the polar wander rate equation

Here is the tedious algebra for deriving Equation (2.15). We begin with the scalar equation Equation (2.14). Let the prefactors $\frac{1}{(C-A)T_1}$ be denoted by A:

$$\dot{\boldsymbol{\omega}} \cdot \dot{\boldsymbol{\omega}} = \dot{\Theta}^2 = A^2 \left[(\mathbf{E}\cdot\boldsymbol{\omega})^2 - (\boldsymbol{\omega}\cdot\mathbf{E}\cdot\boldsymbol{\omega})^2 .\right] \tag{2.58}$$

Since this is a scalar equation, we can arbitrarily choose a coordinate system in which to evaluate it. It is most convenient to choose the principal axes of $\mathbf{E}$, where

$$\mathbf{E} = \begin{bmatrix} \lambda_1 & 0 & 0 \\ 0 & \lambda_2 & 0 \\ 0 & 0 & \lambda_3 \end{bmatrix} \tag{2.59}$$

$$\boldsymbol{\omega} = \begin{bmatrix} \sin\theta\cos\phi \\ \sin\theta\sin\phi \\ \cos\theta \end{bmatrix}. \tag{2.60}$$

As a warm-up, consider the case where $\phi = 0$, then

$$\boldsymbol{\omega} = \begin{bmatrix} \sin\theta \\ 0 \\ \cos\theta \end{bmatrix} \tag{2.61}$$

We can evaluate some of the terms of the scalar equation for $\dot{\Theta}^2$:

$$\mathbf{E} \cdot \boldsymbol{\omega} = \begin{bmatrix} \lambda_1 \sin\theta \\ 0 \\ \lambda_3 \cos\theta \end{bmatrix} \tag{2.62}$$

$$(\mathbf{E} \cdot \boldsymbol{\omega})^2 = \lambda_1^2 \sin^2\theta + \lambda_3^2 \cos^2\theta \tag{2.63}$$

$$\boldsymbol{\omega} \cdot \mathbf{E} \cdot \boldsymbol{\omega} = \lambda_1 \sin^2\theta + \lambda_3 \cos^2\theta \tag{2.64}$$

$$(\boldsymbol{\omega} \cdot \mathbf{E} \cdot \boldsymbol{\omega})^2 = \lambda_1^2 \sin^4\theta + \lambda_3^2 \cos^4\theta + 2\lambda_1\lambda_3 \sin^2\theta \cos^2\theta \tag{2.65}$$

Therefore, plugging these into the scalar equation for $\dot{\boldsymbol{\omega}}^2$, we find:

$$\begin{aligned} \frac{\dot{\Theta}}{A^2} &= (\mathbf{E} \cdot \boldsymbol{\omega})^2 - (\boldsymbol{\omega} \cdot \mathbf{E} \cdot \boldsymbol{\omega})^2 \\ &= \lambda_1^2 \sin^2\theta + \lambda_3^2 \cos^2\theta - \lambda_1^2 \sin^4\theta - \lambda_3^2 \cos^4\theta - 2\lambda_1\lambda_3 \sin^2\theta \cos^2\theta \\ &= \lambda_1^2 \sin^2\theta(1 - \sin^2\theta) + \lambda_3^2 \cos^2\theta(1 - \cos^2\theta) - 2\lambda_1\lambda_3 \sin^2\theta \cos^2\theta \\ &= \lambda_1^2 \sin^2\theta \cos^2\theta + \lambda_3^2 \cos^2\theta \sin^2\theta - 2\lambda_1\lambda_3 \sin^2\theta \cos^2\theta \\ &= (\lambda_1^2 + \lambda_3^2 - 2\lambda_1\lambda_3) \sin^2\theta \cos^2\theta \\ &= \frac{1}{2}(\lambda_3 - \lambda_1)^2 \sin 2\theta \end{aligned} \tag{2.66}$$

which is equivalent to Equation (2.17).

Now consider the more general case where $\phi \neq 0$. Again, we evaluate some of the terms of the scalar equation for $\dot{\boldsymbol{\omega}}^2$:

$$\mathbf{E} \cdot \boldsymbol{\omega} = \begin{bmatrix} \lambda_1 \sin\theta \cos\phi \\ \lambda_2 \sin\theta \sin\phi \\ \lambda_3 \cos\theta \end{bmatrix} \tag{2.67}$$

$$(\mathbf{E} \cdot \boldsymbol{\omega})^2 = \lambda_1^2 \sin^2\theta \cos^2\phi + \lambda_2^2 \sin^2\theta \sin^2\phi + \lambda_3^2 \cos^2\theta \tag{2.68}$$

$$\boldsymbol{\omega} \cdot \mathbf{E} \cdot \boldsymbol{\omega} = \lambda_1 \sin^2\theta \cos^2\phi + \lambda_2 \sin^2\theta \sin^2\phi + \lambda_3 \cos^2\theta \tag{2.69}$$

$$\begin{aligned} (\boldsymbol{\omega} \cdot \mathbf{E} \cdot \boldsymbol{\omega})^2 =& \lambda_1^2 \sin^4\theta \cos^4\phi + \lambda_2^2 \sin^4\theta \sin^4\phi + \lambda_3^2 \cos^4\theta \\ &+ 2\lambda_1\lambda_2 \sin^4\theta \cos^2\phi \sin^2\phi \\ &+ 2\lambda_1\lambda_3 \sin^2\theta \cos^2\theta \cos^2\phi \\ &+ 2\lambda_2\lambda_3 \sin^2\theta \cos^2\theta \sin^2\phi \end{aligned} \tag{2.70}$$

Again, plugging these into the scalar equation for $\dot{\Theta}^2$, we find:

$$\begin{aligned}\frac{\dot{\Theta}^2}{A^2} &= (\mathbf{E}\cdot\boldsymbol{\omega})^2 - (\boldsymbol{\omega}\cdot\mathbf{E}\cdot\boldsymbol{\omega})^2 \\ &= \lambda_1^2\sin^2\theta\cos^2\phi + \lambda_2^2\sin^2\theta\sin^2\phi + \lambda_3^2\cos^2\theta \\ &\quad - \lambda_1^2\sin^4\theta\cos^4\phi - \lambda_2^2\sin^4\theta\sin^4\phi - \lambda_3^2\cos^4\theta \\ &\quad - 2\lambda_1\lambda_2\sin^4\theta\cos^2\phi\sin^2\phi \\ &\quad - 2\lambda_1\lambda_3\sin^2\theta\cos^2\theta\cos^2\phi \\ &\quad - 2\lambda_2\lambda_3\sin^2\theta\cos^2\theta\sin^2\phi.\end{aligned} \tag{2.71}$$

After a lot of simplification, we get

$$\begin{aligned}\frac{\dot{\Theta}^2}{A^2} =& \frac{1}{4}\sin^2 2\theta\left[(\lambda_3-\lambda_1)^2\cos^2\phi + (\lambda_3-\lambda_2)^2\sin^2\phi\right] + \\ & \frac{1}{4}\sin^4\theta\sin^2 2\phi\,(\lambda_2-\lambda_1)^2\end{aligned} \tag{2.72}$$

which is Equation (2.15).

Chapter 3

Time integration of free surfaces in viscous flows

3.1 Introduction

Surface topography in simulations of mantle convection and other geodynamic processes is an important observable, allowing insights into Earth's internal density structure, rheology, and geoid perturbations (e.g. Richards and Hager, 1984; Hager et al., 1985; Baumann et al., 2014). Historically, most simulations have been performed with free-slip boundary conditions at the surface, with dynamic topography calculated as a postprocessing step (e.g. Jarvis and Peltier, 1982; Zhong et al., 2000).

There have been several approaches to treating real free surfaces in geodynamic simulations. Zhong et al. (1996) introduced a pseudo-free-surface formulation, where the free surface coordinate was treated as an extra variable that was integrated in time. In this formulation, the free surface is approximated on the undeformed Eulerian grid by applying pressure boundary conditions on the reference surface. The pressure is determined by a first-order Taylor series approximation of the hydrostatic pressure profile predicted by the surface topography.

A large number of studies have approximated free surfaces in the interior of the domain by using the 'sticky air' approximation (see Crameri et al. (2012a) and references therein). In this approximation there is a low-viscosity, low-density layer in the fluid (termed 'air', though its viscosity is much higher) above the free surface, effectively decoupling it from the boundary. Typically a free-slip boundary condition is used above the sticky air, though an open boundary may be preferable (Hillebrand et al., 2014).

Finally, one can use a true free surface, where a stress-free boundary condition is applied on the boundary of the domain. In this case, there can be flow in and out of the domain, so the boundary must move in time. A true free surface has mathematical elegance in that the boundary condition of the domain more closely matches the boundary conditions which one is trying to model, but it typically requires a deformable domain with frequent remeshing to avoid ill-conditioned cells (i.e., cells that are inverted or have large aspect ratios).

Recently, the nature of surface boundary conditions have been shown to be important for controlling the dynamics of subduction zone modeling. In a benchmark study Schmeling et al. (2008) performed extensive testing on the effect of a free surface on the sinking of a slab. They found that the nature of the free surface had a large effect on the dynamics of the slab, affecting both the shape and the timing of sinking. Most of the participating codes in that benchmark used the sticky air approximation. They found that the specific properties of the sticky air layer controlled the shape and timing of the slab. Furthermore, the viscosity averaging scheme for areas of transitional composition was extremely important, as the simulation of the subducting slab entrained significant amounts of the sticky air. Crameri et al. (2012a) conducted comparisons between sticky air and true free surface models, demonstrating a range of parameters for sticky air which can mitigate some of the difficulties that it introduces. A study by Quinquis et al. (2011) found that free surface boundary conditions have a large effect on trench migration in a subduction zone, and Crameri et al. (2012b) found that a free surface combined with a weak crust is important for producing one-sided subduction zones.

All of the approaches to free surface simulations have been subject to an instability which has been variously termed a "sloshing," or "drunken sailor" instability (Kaus et al., 2010; Duretz et al., 2011; Kramer et al., 2012). This instability, arising from the large density contrast typical at a free surface (compared with the much smaller internal density contrasts), severely limits the maximum stable timestep for free surface computations. Frequently, the maximum stable timestep is several orders of magnitude smaller than that for an otherwise equivalent model with free-slip boundary conditions.

Several studies have attempted to alleviate the timestepping requirements imposed by the sloshing instability. Since the most expensive part of geodynamic simulations is typically the Stokes solve, most free surface calculations have preferred to use explicit timestepping methods for the free surface. Kaus et al. (2010) proposed a quasi-implicit scheme which modifies the discretized Stokes matrix, giving it better stability properties. Popov and Sobolev (2008), Kramer et al. (2012), and Furuichi and May (2015) explored methods for solving the transport of the free surface implicitly.

The paper is organized as follows. After introducing the problem in Section 3.2, we derive an approach to analyze free surface schemes based on the normal modes in Section 3.3 and Section 3.4. In Section 3.5 we use this approach to look at the quasi-implicit stabilization proposed in Kaus et al. (2010). Then, we propose a new time marching scheme for free surface computations with good stability properties (Section 3.6). Finally, we describe the implementation of a free surface in the mantle convection software `ASPECT` in Section 3.7, before showing some numerical results and benchmarks in Section 3.8.

3.2 Governing equations

We begin with the incompressible momentum conservation equations for creeping incompressible flow:

$$\begin{aligned} \nabla \cdot \mathbf{T} &= \rho \mathbf{g} \\ \nabla \cdot \mathbf{u} &= 0, \end{aligned} \tag{3.1}$$

where $\mathbf{u}$ is the fluid velocity, ρ is the fluid density, and $\mathbf{g}$ is the force due to gravity. $\mathbf{T}$ is the stress tensor for a Newtonian fluid, defined by

$$\mathbf{T} = 2\eta\varepsilon(\mathbf{u}) - p\mathbf{I}, \tag{3.2}$$

where η is the viscosity, $\varepsilon(\mathbf{u}) = \frac{1}{2}(\nabla\mathbf{u} + (\nabla\mathbf{u})^T)$ is the strain-rate tensor, and $\mathbf{I}$ is the identity tensor. Substituting the stress tensor into Equation (3.1) gets the familiar form of the Stokes equation:

$$\nabla \cdot (2\eta\varepsilon(\mathbf{u})) - \nabla p = \rho\mathbf{g}. \tag{3.3}$$

For the purposes of this analysis it is useful to define a hydrostatic reference state where the velocity $\mathbf{u}$ is zero:

$$-\nabla p_0 = \rho_0 \mathbf{g}, \tag{3.4}$$

where p_0 is the reference hydrostatic pressure and ρ_0 is a reference density profile (which may vary with depth). The total pressure and density can then be decomposed into variations about their reference values: $\rho = \rho_0 + \rho'$, $p = p_0 + p'$. Using this, the hydrostatic reference state (Equation (3.4)) may be subtracted from Equation (3.3).

This gives rise to the following time dependent, coupled system with unknowns $\mathbf{u}(t)$ and $\mathbf{p}(t)$:

$$\begin{aligned} \nabla \cdot (2\eta\varepsilon(\mathbf{u})) - \nabla p' &= \rho'\mathbf{g} \qquad \text{in } \Omega(t) \\ \nabla \cdot \mathbf{u} &= 0 \qquad \text{in } \Omega(t) \end{aligned} \tag{3.5}$$

defined on the bounded, moving domain $\Omega(t) \subset \mathbb{R}^d$ with boundary $\partial\Omega = \Gamma_0 \cup \Gamma_F$ split into fixed (Dirichlet) and free surface parts Γ_0 and Γ_F, respectively. The boundary conditions are given by

$$\begin{aligned} \mathbf{u} &= 0 \qquad \text{on } \Gamma_0 \\ \mathbf{T} \cdot \mathbf{n} &= 0 \qquad \text{on } \Gamma_F. \end{aligned} \tag{3.6}$$

For the sake of economy, we neglect inhomogeneous stress boundary conditions, though it would be straightforward to include them. We also defer discussion of free slip boundary conditions. The domain at time t is defined by advecting a reference configuration Ω_0 by the domain velocity $\mathbf{u}(t)$

$$\Omega(t) = \Omega_0 + \int_{t_0}^{t} \mathbf{u}(t)\ \mathrm{d}t. \tag{3.7}$$

We defer the discussion of the velocity of the discretized domain to Section 3.7.1. Finally, we denote the displacement at time t by $\zeta = \int_{t_0}^{t} \mathbf{u}_{\text{surface}}(t) \cdot \mathbf{n}\ \mathrm{d}t$, leading to the evolution equation

$$\frac{\mathrm{d}\zeta}{\mathrm{d}t} = \mathbf{u} \cdot \mathbf{n} \quad \text{on } \Gamma_F. \tag{3.8}$$

3.3 Eigenvalue analysis

In order to better understand the time evolution of the system in Equation (3.5), we will consider the eigenvalues of a simplified homogeneous system where we neglect variations in density ($\rho' = 0$):

$$\begin{aligned} \nabla \cdot (2\eta\varepsilon(\mathbf{u})) - \nabla p' &= 0 \\ \nabla \cdot \mathbf{u} &= 0. \end{aligned} \tag{3.9}$$

We will proceed with this analysis within a finite element framework, though similar arguments should work for other discrete methods. We transform the governing equations into the weak form amenable to finite elements via standard operations (e.g. Zienkiewicz and Taylor, 1977) to get

$$\int_{\Omega(t)} 2\eta\varepsilon(\mathbf{w}) \colon \varepsilon(\mathbf{u}) - \int_{\Omega(t)} p' \nabla \cdot \mathbf{w} - \int_{\Gamma_F(t)} \mathbf{w} \cdot \mathbf{T} \cdot \mathbf{n} = 0 \tag{3.10}$$

$$\int_{\Omega(t)} q \nabla \cdot \mathbf{u} = 0, \tag{3.11}$$

where $\mathbf{w}$ and q are suitably chosen test functions and the integrals over $\Omega(t)$ and $\Gamma_F(t)$ are over the volume of the domain and the free surface, respectively. Note that since the free surface can move, the shape of the domain is a function of time.

The integral over the surface in Equation (3.10) accounts for boundary stresses, which should be zero when evaluated on a true free surface. Rather than analyzing finite deformation to the free surface (a nonlinear problem), we will make the analytically useful approximation of small deformations about the hydrostatic reference surface and analyze their stability. We will therefore evaluate the integrals in Equation (3.10) over the hydrostatic reference surface and introduce a temporary auxiliary variable ζ which represents the (small) topography of the free surface relative to that reference surface. On the reference surface the gravity vector is opposite the direction of the surface normal $\mathbf{g} = -g\mathbf{n}$. The stress on this reference surface can be approximated by using the first order Taylor series expansion of the hydrostatic pressure profile:

$$\mathbf{T} \approx \frac{\partial \mathbf{T}}{\partial \mathbf{n}} \cdot \mathbf{n}\zeta = -\rho_0 g \zeta \mathbf{I}. \tag{3.12}$$

Equation (3.10) then becomes

$$\int_{\Omega(t)} 2\eta\varepsilon(\mathbf{w}) \colon \varepsilon(\mathbf{u}) - \int_{\Omega(t)} p' \nabla \cdot \mathbf{w} + \int_{\Gamma_F(t)} \rho_0 g \zeta \mathbf{w} \cdot \mathbf{n} = 0. \tag{3.13}$$

We would like to analyze the time evolution of the normal modes of this system: each mode corresponds to the relaxation of topography with a characteristic wavelength and relaxation time. These times are determined by the model geometry, gravity, viscosity structure, and density structure. We denote the normal modes by $[\mathbf{u}_i, p'_i, \zeta_i]^T$, with relaxation times τ_i, where the subscript corresponds to the ith normal mode.

The equations decouple for the normal modes, and Equation (3.8) then becomes

$$\frac{\mathrm{d}}{\mathrm{d}t}\zeta_i(\mathbf{x},t) = \frac{\mathrm{d}}{\mathrm{d}t}\zeta_i(\mathbf{x})e^{-t/\tau_i} = -\frac{\zeta_i(\mathbf{x},t)}{\tau_i} = \mathbf{u}_i \cdot \mathbf{n}. \tag{3.14}$$

This can then be used to eliminate ζ from the Stokes system:

$$\int_{\Omega(t)} 2\eta\varepsilon(\mathbf{w}) \colon \varepsilon(\mathbf{u}_i) - \int_{\Omega(t)} p_i' \nabla \cdot \mathbf{w} = \tau_i \int_{\Gamma_F(t)} \rho_0 g(\mathbf{u}_i \cdot \mathbf{n})(\mathbf{w} \cdot \mathbf{n}). \tag{3.15}$$

Equations (3.10), (3.11), and (3.15) are continuous forms of the governing equations which must be discretized in space and time in order to be solved numerically. In particular, we must decide at which timestep (or combination of timesteps) we will integrate over the domain $\Omega(t)$. We denote discrete times by t^n, where n is the timestep number, and $t^{n+1} = t^n + \Delta t$. It is most convenient to integrate over the domain at the current timestep $\Omega^n \equiv \Omega(t^n)$ instead of the unknown $\Omega^{n+1} \equiv \Omega(t^n + \Delta t)$. This corresponds to an explicit scheme. However, as we will see, the implicit scheme of integrating over the (unknown) domain at the next timestep Ω^{n+1} will give a stable timestepping scheme, at the cost of making the problem nonlinear (Furuichi and May, 2015).

When these equations are spatially discretized using finite elements (see, e.g. Kronbichler et al., 2012) we get

$$\begin{bmatrix} A & B^T \\ B & 0 \end{bmatrix} \begin{bmatrix} \mathbf{u}_i^h \\ p_i^h \end{bmatrix} = \tau_i \begin{bmatrix} M & 0 \\ 0 & 0 \end{bmatrix} \begin{bmatrix} \mathbf{u}_i^h \\ p_i^h \end{bmatrix}, \tag{3.16}$$

where $\mathbf{u}_i^h$ and p_i^h are finite-dimensional representations of $\mathbf{u}_i$ and p_i', and the domain integrals are performed over a discrete approximation of the domain shape (such as a linear finite element basis) which we denote by $\hat{\Omega}$. M is the discretization of the bilinear form on the right-hand side of Equation (3.15). The form of Equation (3.16) does not depend on whether we choose $\hat{\Omega}^n$ or $\hat{\Omega}^{n+1}$ for the domain integration.

Equation (3.16) is a generalized eigenvalue problem for the normal modes of the system. It has strictly positive eigenvalues (see Appendix 3.A). It is rather more difficult to solve than a standard eigenvalue problem because the matrix on the right-hand-side is not invertible. It may, however, be transformed into a standard eigenvalue problem. By defining

$$C = \begin{bmatrix} A & B^T \\ B & 0 \end{bmatrix} \quad D = \begin{bmatrix} M & 0 \\ 0 & 0 \end{bmatrix} \quad \mathbf{y}_i = \begin{bmatrix} \mathbf{u}_i^h \\ p_i^h \end{bmatrix} \tag{3.17}$$

and then multiplying both sides by $\tau_i^{-1} C^{-1}$ we get

$$(C^{-1}D)\mathbf{y}_i = \tau_i^{-1}\mathbf{y}_i. \tag{3.18}$$

This eigenvalue equation can be solved for the normal modes and relaxation times of the Stokes system with a free surface.

3.4 Time integration of the free surface

Armed with the normal modes and relaxation times of the Stokes system, we can write down the formal solution to Equation (3.8). Let the initial surface topography be represented by a linear combination of its normal modes

$$\zeta(\mathbf{x}, t = 0) = \sum_i a_i \zeta_i(\mathbf{x}), \tag{3.19}$$

then the time evolution of the free surface is given by

$$\zeta(\mathbf{x}, t) = \sum_i a_i \zeta_i(\mathbf{x}) e^{-t/\tau_i}. \tag{3.20}$$

Of course, most finite element (or finite difference, or finite volume) geodynamic simulations do not resolve the solution and surface topography into its normal modes and integrate those separately. Indeed, analytical solutions for the normal modes are only known for simple geometries and rheologies. Instead, one typically obtains a velocity solution and then advect the free surface with the local velocity. The normal mode solution is instructive, however. Each mode has the form of a decay equation with characteristic decay time τ_i. The decay equation is the archetypical example of a stiff ordinary differential equation. If we were to numerically integrate this in time with a forward Euler method, we would find the timestep criterion for stability (e.g. LeVeque, 2007) to be

$$\Delta t \leq 2\tau_{\min}, \tag{3.21}$$

where $\tau_{\min}$ is this minimum decay time. The maximum stable timestep is limited by the minimum relaxation timescale. If a larger timestep than this is taken then those modes will become unstable. The modes with the smallest relaxation times are usually those with the largest lengthscales (Schubert et al., 2001), and so it will be those which become unstable first, a phenomenon which has been called a "sloshing", or "drunken sailor" instability (Kaus et al., 2010).

3.5 Analysis of quasi-implicit stabilization

The relaxation timescales for surface topography tend to be considerably shorter than those for convection or tectonic deformation, so the stability requirements for a forward Euler scheme are quite onerous. On the other hand, an implicit time marching scheme requires solving a nonlinear system for the new surface position, or assembling a larger system with surface topography unknowns (e.g. Kramer et al., 2012).

Kaus et al. (2010) proposed a scheme whereby the body forces on the domain are evaluated on a prediction of the shape of the domain at a later time. The continuous weak form of the right-hand-side body forces in is then

$$\mathbf{f}_{\text{body}} = \int_{\Omega^n + \Delta\Omega} \rho \mathbf{w} \cdot \mathbf{g}. \tag{3.22}$$

We can approximate the shape prediction by time integrating the domain evolution equation (Equation (3.7)):

$$\Delta\Omega \approx \theta\Delta t\mathbf{u}, \tag{3.23}$$

where θ is a free parameter that corresponds to the magnitude of the correction, where zero is no stabilization and one is fully (quasi) implicit.

One can approximately expand the integral in Equation (3.22) using Reynold's transport theorem to find

$$\int_{\Omega^n+\Delta\Omega} \rho\mathbf{w}\cdot\mathbf{g} \approx \int_{\Omega^n} \rho\mathbf{w}\cdot\mathbf{g} + \theta\Delta t\int_{\Gamma_F^n} \rho(\mathbf{w}\cdot\mathbf{g})(\mathbf{u}\cdot\mathbf{n}). \tag{3.24}$$

The volume integral is the same as that of the unstabilized problem, but now we obtained an additional surface integral. It has the form of a velocity-dependent surface stress pushing down on the domain, and can be thought of as an artificial viscous damping of the surface. Since the term depends on the velocity, it enters the Stokes system matrix as a stabilization term. Empirically, it has been found to be successful at damping instabilities (Kaus et al., 2010; Quinquis et al., 2011; Duretz et al., 2011).

The surface integral in Equation (3.24) is almost the same as that on the right hand side of Equation (3.15), which was discretized as the matrix M. By making two approximations we can connect it with the formalism developed in Section 3.3. First, when the current position of the surface is near to the reference surface (i.e., the slope is not too steep) then gravity is approximately in the direction of the surface normal: $\mathbf{g} \approx -g\mathbf{n}$. Furthermore, in Equation (3.15) we considered response of the surface in a homogeneous system where there were no lateral density variations, while Equation (3.24) uses the total density. In most geodynamic simulations lateral density variations are small compared to the total density. For the purposes of stabilization we may approximate $\rho \approx \rho_0$. Inserting these two approximations, we find that the stabilization term may be written as

$$-\theta\Delta t\int_{\Gamma_F^n} \rho_0 g(\mathbf{w}\cdot\mathbf{n})(\mathbf{u}\cdot\mathbf{n}), \tag{3.25}$$

where the integral is now identical to that which discretizes to M.

If we discretize the Stokes system with the quasi-implicit stabilization term, we find a new generalized eigenvalue problem:

$$\begin{bmatrix} A+\theta\Delta t M & B^T \\ B & 0 \end{bmatrix}\begin{bmatrix}\mathbf{u}_i^h \\ p_i^h\end{bmatrix} = \tau_i^S \begin{bmatrix} M & 0 \\ 0 & 0\end{bmatrix}\begin{bmatrix}\mathbf{u}_i^h \\ p_i^h\end{bmatrix}, \tag{3.26}$$

where τ_i^S indicate the eigenvalues of the stabilized system. This system may be rearranged:

$$\begin{bmatrix} A & B^T \\ B & 0 \end{bmatrix}\begin{bmatrix}\mathbf{u}_i^h \\ p_i^h\end{bmatrix} = \left(\tau_i^S - \theta\Delta t\right)\begin{bmatrix} M & 0 \\ 0 & 0\end{bmatrix}\begin{bmatrix}\mathbf{u}_i^h \\ p_i^h\end{bmatrix}. \tag{3.27}$$

This is precisely the same generalized eigenvalue problem as Equation (3.16), so its eigenvalues must be the same. This allows us to write the eigenvalues of the stabilized

problem in terms of those of the unstabilized problem:

$$\tau_i^S = \tau_i + \theta\Delta t. \tag{3.28}$$

Essentially, the stabilization term lengthens every relaxation time for the system by an amount $\theta\Delta t$. This correspondingly lengthens the maximum stable timestep for the forward Euler method:

$$\Delta t \leq \frac{2}{1-\theta}\tau_{\min}. \tag{3.29}$$

Note that as θ goes to one this scheme should become unconditionally stable, but nonlinear effects and discretization errors due to finite deformation of the surface could prevent that stability.

The lengthening of relaxation times due to the quasi-implicit stabilization has an unequal effect on the modes. They are all lengthened by the same amount, which is a much bigger fraction of the total relaxation time for the shorter-time modes than the longer-time ones. Therefore the shorter-time modes are effectively damped more. This can be seen as an attractive feature of the scheme, since those are the least stable modes, though it can result in less accurate time-marching of the longest wavelengths of the system.

3.5.1 Numerical determination of $\tau_{\min}$

It can be useful to determine the minimum relaxation time $\tau_{\min}$ for a particular simulation setup, both to determine an appropriate timestep and as a check on the eigenvalue analysis above. As discussed in Section 3.3, the generalized eigenvalue problem given by Equation (3.26) is difficult to solve because the matrix on the right-hand-side is not invertible. However, we may convert Equation (3.26) to a standard eigenvalue problem in the same manner as before. Introducing C_S as the Stokes system matrix with the stabilization term included, and with D and $\mathbf{y}_i$ the same as in Equation (3.17), we find

$$(C_S^{-1}D)\mathbf{y}_i = \frac{1}{\tau_i^S}\mathbf{y}_i. \tag{3.30}$$

Several things are of note about this eigenvalue equation which help in solving it. The matrix D is a mass matrix which is only nonzero on the free surface, so it is mostly empty, and, in general, it is not necessary to explicitly form the matrix in order to apply it. Second, applying the inverse of C_S amounts to solving the Stokes system, so any existing geodynamical code can already do this. Third, it is now an equation for the inverse of τ_i^S, and so solving for the minimum relaxation time is now equivalent to finding the *maximum* eigenvalue of Equation (3.30).

All of these factors mean that power iteration (see, e.g., Golub and Van Loan (2012)), which finds the dominant eigenvalue/eigenvector pair, is an attractive option for finding $\tau_{\min}$. We have tested the effectiveness of power iteration for finding the minimum relaxation time on a problem for which there is an analytical solution. We also use it to confirm Equation (3.28). Following Kramer et al. (2012) we model the relaxation of surface topography in

a two-dimensional Cartesian box with an isoviscous fluid. The setup is shown in Figure 3.1. The eigenvectors of this system are given by infinitesimal sinusoidal perturbations to the free surface

$$\zeta(x,0) = \zeta_0 \cos(kx), \tag{3.31}$$

where $k = 2\pi n/L$, and n is a wavenumber which is an integer multiple of 1/2. For an infinitesimal perturbation of this form, the relaxation time τ is given by

$$\tau = \frac{Dk + \sinh(Dk)\cosh(Dk)}{\sinh^2(Dk)} \frac{2k\eta}{\rho g}, \tag{3.32}$$

where D is the layer depth, η is the viscosity, ρ is the density, and g is the acceleration due to gravity.

The eigenvector with the minimum relaxation time for this system $\tau_{\min}$ corresponds to $n = 1/2$ (which, as expected, has the form of the fluid sloshing back and forth). Figure 3.2 shows the results of the power iteration, where colored circles indicate the numerical solution and black dots show the analytical solution using equation (3.28). In most cases the iteration converges to better than $\sim 10^{-5}$ relative accuracy in about 20 iterations (and fewer with a good initial guess).

3.6 A novel time-integration scheme

The implementation of such a scheme results in a slightly asymmetric matrix, which can be more difficult to solve, requiring either changes to the solver/preconditioner, or symmetrization of the stabilization term (Kaus et al., 2010). An alternative would be to construct a time-integration scheme that remains stable at larger timesteps. The reason that forward Euler integration performs so badly with the decay of topography is that at larger timesteps it overshoots its equilibrium position. This overshoot causes it to lurch back to the *other* side of equilibrium, overshooting even more. We would like to construct an explicit scheme that accounts for following properties which we know the system has:

- In the absence of forcing, topography always decreases (Appendix 3.A).
- Relaxation of small amplitude topography takes the form of exponential decay (Section 3.3).
- The decay mode with the shortest relaxation time is the least stable (Section 3.4).

3.6.1 Nonstandard finite-differences

A general expression for the evolution of a free surface from time t^n to time t^{n+1} is

$$\mathbf{x}(t^{n+1}) = \mathbf{x}(t^n) + \int_{t^n}^{t^{n+1}} \mathbf{u}(t)\, \mathrm{d}t, \tag{3.33}$$

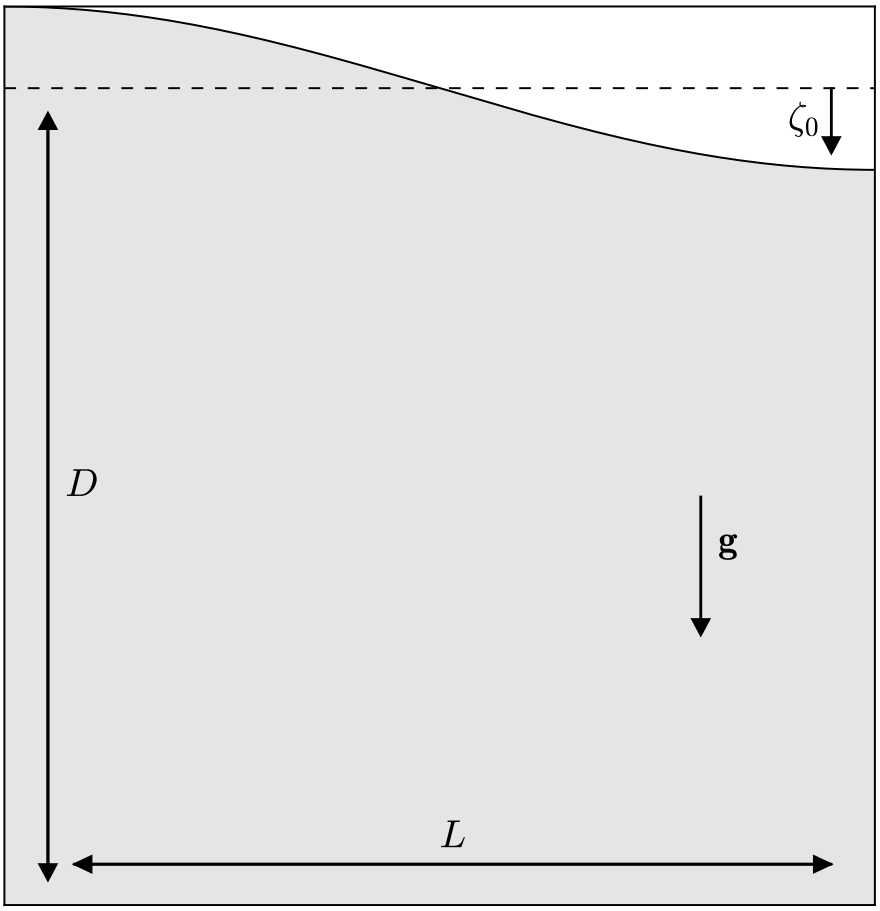

Figure 3.1: Setup for the power iteration test (Section 3.5.1) and for the free surface relaxation benchmark (Section 3.8.1). A 2D box with an isoviscous fluid has sinusoidal initial topography, with amplitude ζ_0 and wavenumber n. The box has depth D and length L. For our tests $\rho = \eta = g = D = L = 1$, and $n = 1/2$. For the power iteration test there is no initial perturbation ($\zeta_0 = 0.0$), and for the surface relaxation benchmark $\zeta_0 = 0.005$.

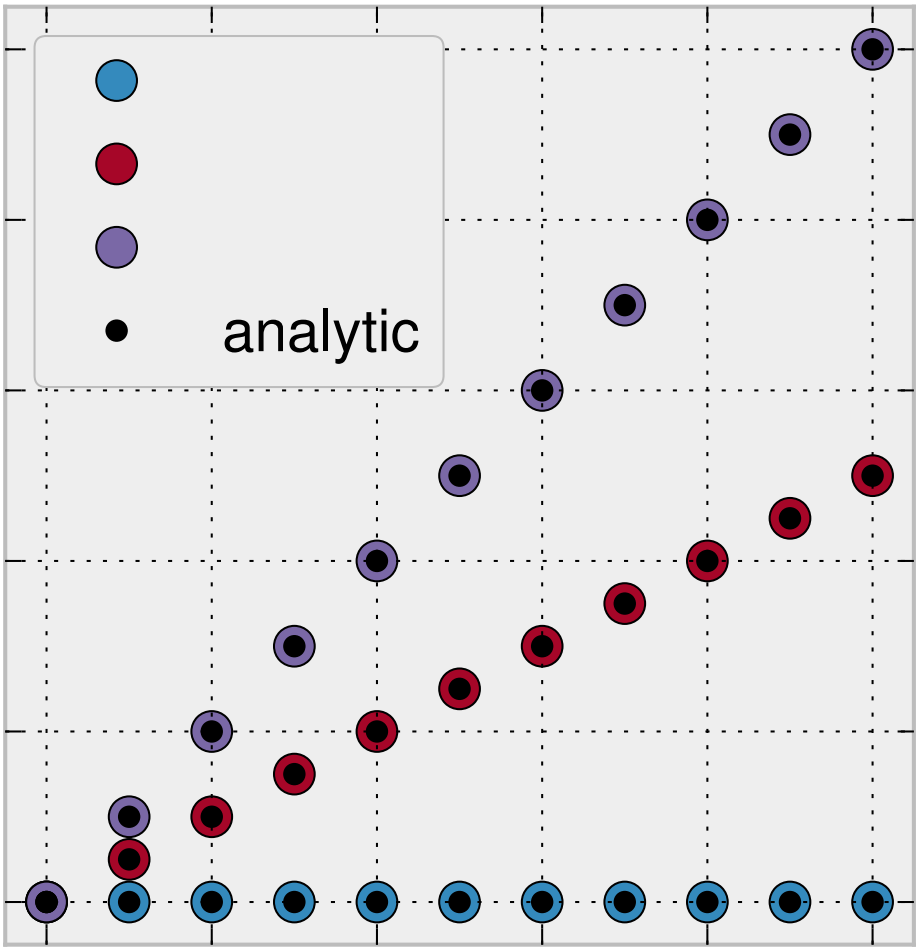

Figure 3.2: The effect of quasi-implicit stabilization on the minimum relaxation time of a fluid in a 2D Cartesian box with a free surface (see Figure 3.1), as well as the result of power iteration to find the minimum relaxation time. The x-axis shows the timestep normalized by minimum relaxation time of the unstabilized problem $\tau_{\min}$. The y-axis shows the stabilized relaxation time τ_S, also normalized by $\tau_{\min}$. Colored circles show the relaxation times found by numerical solution of Equation (3.30) with different values of the stabilization parameter θ. Black dots show the relaxation times calculated using Equation (3.28). The stabilized timescale is lengthened for larger timesteps and for larger values of θ. For this test case, power iteration typically attains better than 1% accuracy in 5-10 iterations.

where $\mathbf{x}$ is the location of the free surface. If we approximate $\mathbf{u}(t) \approx \mathbf{u}(t^n)$, we of course recover the forward Euler scheme. However, we can make another choice based on our knowledge of the system behavior. We can approximate $\mathbf{u}(t)$ as

$$\mathbf{u}(t) = \mathbf{u}(t^n)e^{-(t-t^n)/\tau^*}, \tag{3.34}$$

where τ^* is some as-yet undetermined positive constant which we will refer to as the "stabilization timescale". This form of $\mathbf{u}$ automatically decays in time, and as we shall see, has much better stability properties than forward Euler integration. Using Equation (3.34) in Equation (3.33) and integrating, we find

$$\mathbf{x}(t^{n+1}) = \mathbf{x}(t^n) + \mathbf{u}(t^n)\tau^* \left(1 - e^{-\Delta t/\tau^*}\right). \tag{3.35}$$

The quantity $\tau^*(1 - e^{-\Delta t/\tau^*})$ acts as a pseudo-timestep for advecting the free-surface. Equation (3.35) is what is known as a nonstandard finite-difference model, based on constructing unusual discrete models for differential equation integration. The theory has been developed in, among others, a series of papers by Mickens (1994, 2002, 2005).

3.6.2 Stability of the scheme

The parameter τ^* sets how quickly $\mathbf{u}$ decays in Equation (3.34), and a good choice is crucial for accuracy and stability. A shorter decay time corresponds to more stabilization, but if it becomes too short, the surface velocity will become overdamped. In general, we will want to choose τ^* so that it is as close as possible to the relaxation time of the least stable mode, or $\tau_{\min}$.

To investigate the stability of this scheme we consider a velocity solution comprised of a single normal mode of the system $\mathbf{u} = a_i\mathbf{u}_i$. This will decay exponentially with relaxation time τ_i, or

$$\frac{\mathrm{d}a_i}{\mathrm{d}t} = -\frac{a_i}{\tau_i}. \tag{3.36}$$

Applying the nonstandard finite difference scheme, we find

$$a_i^{n+1} = a_i^n \left[1 - \frac{\tau^*}{\tau_i}\left(1 - e^{-\Delta t/\tau^*}\right)\right]. \tag{3.37}$$

In order for the scheme to be stable, the quantity in brackets must remain bounded as it is repeatedly multiplied by itself, or

$$\left|1 - \frac{\tau^*}{\tau_i}\left(1 - e^{-\Delta t/\tau^*}\right)\right| \leq 1. \tag{3.38}$$

The stability of this scheme is determined by the choice of τ^*. It has a region of unconditional stability, where

$$\tau^* \leq 2\tau_i. \tag{3.39}$$

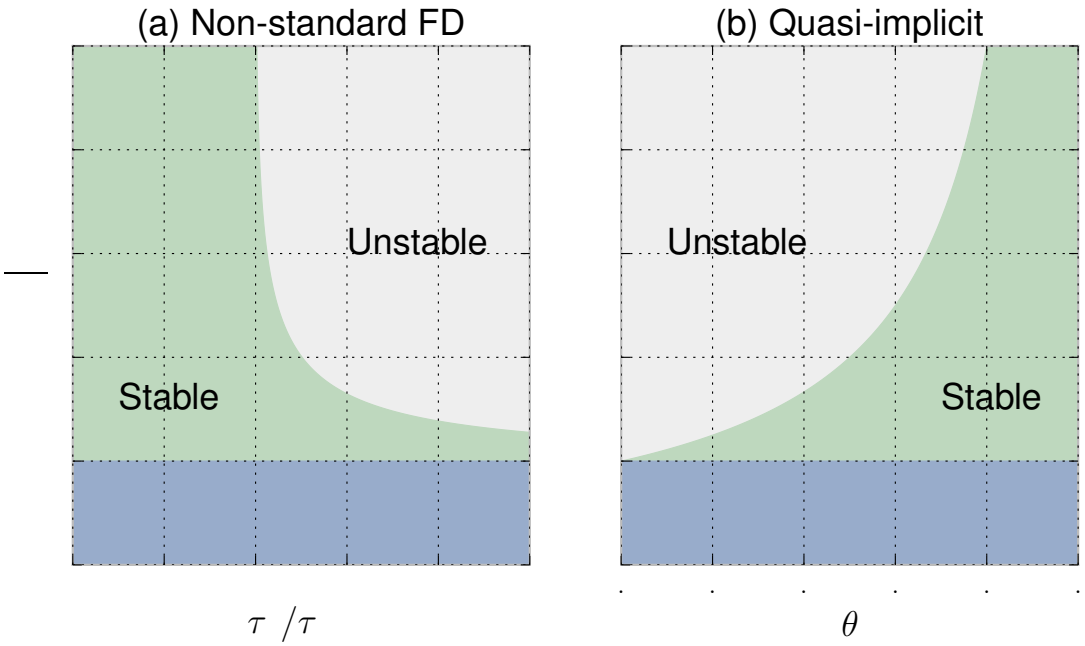

Figure 3.3: (a) Stability region for the nonstandard finite difference scheme (green, Equations (3.39) and (3.40)). On the x-axis is the value of the stabilization timescale, in units of the minimum relaxation time $\tau_{\min}$. On the y-axis is the value of the timestep, also in units of the minimum relaxation time. For $\tau^* \leq 2\tau_{\min}$ the nonstandard finite difference scheme is unconditionally stable. (b) Stability region for the quasi-implicit scheme (green, Equation (3.29)). Again, the y axis is in units of the minumum relaxation time. The x-axis shows the value of the stabilization parameter θ. For $\theta = 1$ the quasi-implicit scheme is unconditionally stable. In both cases the stability region for the forward Euler scheme (Equation (3.21)) is also shown in blue.

Otherwise, the scheme is conditionally stable, with the timestep limited by

$$\Delta t \leq -\tau^* \log\left(1 - 2\frac{\tau_i}{\tau^*}\right). \tag{3.40}$$

The stability region is plotted in Figure 3.3. Equations (3.39) and (3.40) are derived in Appendix 3.B.

3.6.3 Accuracy and asymptotics of the scheme

It is important to note that even though we derived the nonstandard finite difference scheme assuming a decaying exponential for $\mathbf{u}$, it is formally a first-order accurate scheme. As such, it is capable of capturing arbitrary motions of the free surface, while allowing larger timesteps than the forward Euler scheme.

Again we may take one of the normal modes as an example and inspect the difference between the nonstandard finite-difference scheme and the analytical solution after one

timestep:

$$\begin{aligned} a_i(\Delta t) - a_i^1 &= a_i(0)e^{-\Delta t/\tau_i} - a_i(0)\left[1 - \frac{\tau^*}{\tau_i}\left(1 - e^{-\Delta t/\tau^*}\right)\right] \\ &= a_i(0)\left[e^{-\Delta t/\tau_i} - 1 + \frac{\tau^*}{\tau_i}\left(1 - e^{-\Delta t/\tau^*}\right)\right]. \end{aligned} \tag{3.41}$$

Note that when $\tau_i = \tau^*$ the nonstandard finite difference scheme is exact. The exponentials may be expanded to find

$$a_i(\Delta t) - a_i^1 = a_i(0)\left(\frac{\Delta t}{\tau_i}\right)^2\left(1 - \frac{\tau_i}{\tau^*}\right) + O(\Delta t^3). \tag{3.42}$$

The local truncation error is quadratic in Δt, similar to the forward Euler schem. Summing this error over many timesteps results in a factor of Δt^{-1}, which results in a global truncation error that is linear in Δt (e.g. LeVeque, 2007), demonstrating the first-order accuracy. The choice of τ^* controls the size of the coefficient on the truncation error for the scheme. The error for a given mode becomes considerably smaller when τ^* is close to its natural relaxation times.

It is helpful to take a closer look at the pseudo-timestep introduced in Equation (3.35): $\tau^*(1 - e^{-\Delta t/\tau^*})$. As the timestep Δt goes to zero, the pseudo timestep approaches Δt, recovering the forward Euler scheme. However, as Δt gets larger, the pseudo-timestep does not increase as quickly, reflecting the decaying nature of the normal modes (in fact, the pseudo-timestep is bounded between Δt and τ^*). Likewise, as the stabilization timescale τ^* goes to infinity, we also recover the forward Euler scheme, in what is essentially the unstabilized problem. But as τ^* goes to zero, the pseudo-timestep also goes to zero. This corresponds to over-stabilizing the problem. With too short of a stabilization timescale the free surface is never advected at all (which is a very stable situation, if not very accurate!).

3.6.4 Choice of τ^*

As discussed above, a full geodynamic simulation will have a spectrum of relaxation times. For complete stability, the parameter τ^* should be chosen such that every mode is stable. In practice, this means that a good choice is

$$\tau^* \approx \tau_{\min}. \tag{3.43}$$

Unfortunately, for many models the minimum relaxation time will not be known beforehand. In order to use the nonstandard finite difference scheme, the value of τ^* would need to be calculated or estimated first. There are several possible ways to determine this value:

- Direct solution of Equation (3.16). Solution of the whole spectrum is expensive when only the minimum relaxation time is required, which means that power iteration on the standard eigenvalue problem (Equation (3.18)) can be enough.

- Analytical formulae. Several geometry and viscosity model combinations have analytical solutions for relaxation spectra. Even if the user's model is not precisely the same (e.g., has some lateral viscosity variations), an analytical approximation may be sufficient.

- Scaling. In general, we expect the relaxation times to scale with $\tau \sim \frac{\eta}{\rho g L}$, where the density, gravity, viscosity, and lengthscale L are all representative values. A small amount of experimentation near this value of τ can find an appropriate relaxation time.

The first point deserves a bit more attention, since it provides the most general method for determining $\tau_{\min}$. We discussed the numerical determination of $\tau_{\min}$ in Section 3.5.1 by solving Equation (3.18) via power iteration. Each iteration requires a solution of the Stokes system (the C matrix), and we have found that $\sim$10 iterations is usually enough to obtain a reasonable estimate of $\tau_{\min}$. This can be done during preprocessing, so over the course of the simulation the cost of determining $\tau_{\min}$ would be negligible.

As a simulation progresses, there is the possibility that its viscosity or density structure will change, and as such its minimum relaxation time will evolve. This, of course, means that the best choice of τ^* can change over the course of a simulation. If $\tau_{\min}$ does not change significantly, the initial estimate can be fine. Otherwise, one can periodically check the evolution and redetermine $\tau_{\min}$ by solving Equation (3.18) during the model run.

In Section 3.8 we show examples the numerical solution of $\tau_{\min}$ and its evolution in time.

3.7 Implementation in ASPECT

We have implemented the ability to run free surface simulations in the mantle convection software ASPECT (Bangerth et al., 2015b; Kronbichler et al., 2012). ASPECT, based on the open source, finite element library deal.II (Bangerth et al., 2015a), is designed to be highly flexible and modular, with the ability for user-defined rheologies, geometries, and gravity models. The implementation of the free surface, therefore, needs to be general enough to work for many combinations of these models, including those which may not have been written yet. In particular, it cannot rely on assumptions regarding the shape of the domain.

Furthermore, ASPECT allows for computations in both 2D and 3D, so the implementation must be sufficiently dimension independent to work in both cases. We implement the free surface within an arbitrary Lagrangian-Eulerian (ALE) formulation (e.g Fullsack, 1995; Donea et al., 2004).

ASPECT is a parallelized, distributed memory code with adaptive mesh refinement (see Bangerth et al. (2011) for details). The free surface implementation works with these features. We store the mesh vertex positions in a fully distributed vector. This vector is continually updated and redistributed across processes upon mesh adaptation (which is handled by the adaptive octree library p4est). We also provide adaptive refinement indicators

based on being near to the free surface or when the free surface slope is steep to allow for accurate interface tracking.

3.7.1 Remeshing

The mesh velocity in normal direction at the free surface (with unit normal $\mathbf{n}$) has to be consistent with the velocity of the Stokes velocity solution $\mathbf{u}(t)$:

$$\mathbf{u}_{\text{mesh}}(t) \cdot \mathbf{n} = \mathbf{u}(t) \cdot \mathbf{n} \quad \text{on} \quad \Gamma_F \tag{3.44}$$

In ALE calculations the internal mesh velocity is undetermined. In general, one wants to smoothly deform the mesh so as to preserve its regularity, avoiding inverted or otherwise poorly conditioned cells. The mesh deformation can be calculated in many different ways, including algebraic (e.g. Thieulot, 2011) and PDE based approaches.

We choose to implement remeshing based on solving Laplace's equation for the mesh velocity. We solve the equation

$$\nabla^2 \mathbf{u}_{\text{mesh}} = 0 \tag{3.45}$$

subject to the boundary conditions

$$\begin{aligned} \mathbf{u}_{\text{mesh}} &= 0 && \text{on } \Gamma_0. \\ \mathbf{u}_{\text{mesh}} &= (\mathbf{u} \cdot \mathbf{n})\,\mathbf{n} && \text{on } \Gamma_F, \\ \mathbf{u}_{\text{mesh}} \cdot \mathbf{n} &= 0 && \text{on } \Gamma_{FS}, \end{aligned} \tag{3.46}$$

where Γ_{FS} is the part of the boundary with free slip boundary conditions, given by

$$\begin{aligned} \mathbf{u} \cdot \mathbf{n} &= 0 \\ \mathbf{T} \cdot \mathbf{n} - (\mathbf{n} \cdot \mathbf{T} \cdot \mathbf{n})\mathbf{n} &= 0 \qquad \text{on } \Gamma_{FS}. \end{aligned} \tag{3.47}$$

This scheme has the advantage of working for many different domain geometries and combinations of boundary conditions. For moderate mesh deformation, the mesh stays smooth and well conditioned, though it breaks down for large deformations.

3.7.2 Surface advection

With a deformable domain there is the danger that small errors in free surface motion can result in poor overall mass conservation in time. In some scenarios, the total volume of the mesh can fluctuate significantly over hundreds or thousands of timesteps. Consistency with the Stokes solution requires

$$\mathbf{u}_{\text{mesh}} \cdot \mathbf{n} = \mathbf{u} \cdot \mathbf{n}. \tag{3.48}$$

Unfortunately the normal vectors are not well defined on the mesh vertices, which is where the mesh velocity is defined. One could instead advect the mesh in the direction of the local

vertical, or in some weighted average of the cell normals adjacent to a given vertex, but we have found that these schemes do not necessarily have good mass conservation properties.

A better approach is to perform an L_2 projection of the normal velocity $\mathbf{u} \cdot \mathbf{n}$ onto the free surface Γ_F. Multiplying the boundary conditions (Equation (3.46)) by a test function $\mathbf{w}$ and integrating over the free surface part of the boundary, we find

$$\int_{\Gamma_F} \mathbf{w} \cdot \mathbf{u}_{\text{mesh}} = \int_{\Gamma_F} (\mathbf{w} \cdot \mathbf{n}) (\mathbf{u} \cdot \mathbf{n}) . \tag{3.49}$$

When discretized, this forms a linear system which can be solved for the mesh velocity $\mathbf{u}_{\text{mesh}}$ at the free surface. A new system to solve is not ideal, but this system, being nonzero over only the free surface, is relatively computationally inexpensive to solve.

This weak solution to the boundary conditions (Equation (3.46)) is able to borrow the accuracy of the Stokes solve for Equation (3.11), and we have found it to conserve mass more accurately than algebraic techniques for evaluating the mesh-normal velocity. Similar results were found by Fullsack (1995).

3.8 Numerical results

3.8.1 Relaxation of sinusoidal topography

We demonstrate the convergence of the nonstandard finite difference model by comparison with an analytical solution. As in Section 3.5.1 we consider the relaxation of sinusoidal surface topography in a two-dimensional Cartesian box with an isoviscous fluid. The setup is shown in Figure 3.1.

For an initial topography given by Equation (3.31), the relaxation time τ is given by Equation (3.32), and the time evolution of the surface topography is given by

$$\zeta(x, t) = \zeta(x, 0) e^{-t/\tau}. \tag{3.50}$$

This solution is only valid for infinitesimal topography. However, for small initial topography ζ_0 it seems to be sufficiently accurate to test convergence orders up to quadratic (Kramer et al., 2012; Furuichi and May, 2015). We estimate the error E by time-integrating the L_2 difference between the numerical and analytical solutions at the center point of the free surface, over a time interval T (which we choose to be 4τ):

$$E = \frac{1}{T} \int_0^T \| \zeta_{\text{numeric}}(L/2, t) - \zeta_{\text{analytic}}(L/2, t) \|_2 \, \mathrm{d}t. \tag{3.51}$$

Figure 3.4a shows the convergence of the nonstandard finite difference scheme with respect to timestep size. The scheme is first order in time, with improving accuracy as the value of τ^* approaches the relaxation time of the relevant mode τ_i. Interestingly, if $\tau^* = \tau_i$ the advection scheme becomes exact (Mickens, 2002). At this point the magnitude of the error plummets and is no longer a strong function of the timestep. The remaining error

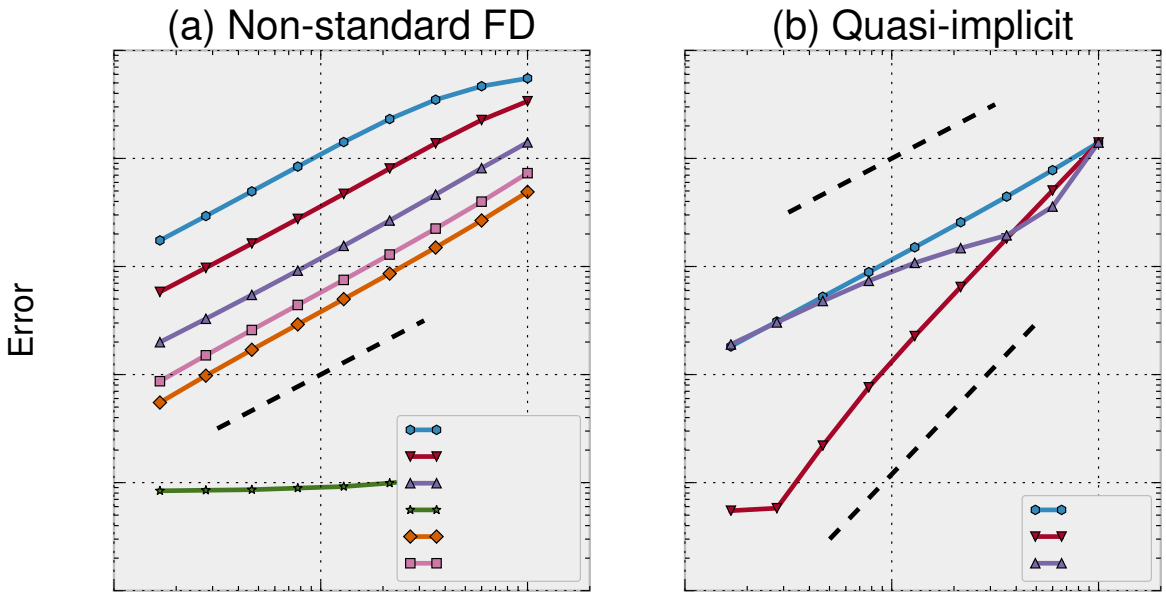

Figure 3.4: Convergence tests for the benchmark shown in Figure 3.1. (a) Convergence test with timestep size for the nonstandard finite difference scheme. Comparison with the slope-one line confirms that it is first-order in time. In the case that the stabilization timescale τ^* is equal to the analytic relaxation time the error becomes very small, as the time integration scheme becomes exact (Mickens, 2002). (b) Convergence test with timestep size for the quasi-implicit scheme. For $\theta = 1$ and $\theta = 0$ the scheme is first-order accurate (though the latter is just an unstabilized forward-Euler scheme). For $\theta = 0.5$ the scheme appears second order accurate on this benchmark.

is likely due to error in the linear approximation for the analytical solution, the spatial discretization, or the linear solver tolerance.

Figure 3.4b shows the convergence of the quasi-implicit scheme as a function of timestep Δt. When $\theta = 0$, it corresponds to the unstabilized forward Euler scheme, and is first order in time. When $\theta = 1$ it is also first order in time, but allows for a much larger timestep. When $\theta = 0.5$ the quasi-implicit guess for the body force is good enough that it actually seems to achieve the second-order convergence of a trapezoidal scheme, though it has not been shown that this extends to more complicated models.

Figure 3.5 shows in more detail the effects of the choice of τ^*. In a narrow region close to the true value of $\tau_{\min}$ the error becomes very small, but in a broader region nearby the errors are larger. The excellent accuracy when the stabilization timescale τ^* is close to one of the natural relaxation timescales allows for tuning of the scheme to track specific long-wavelength modes, such as those due to rotational or tidal deformation.

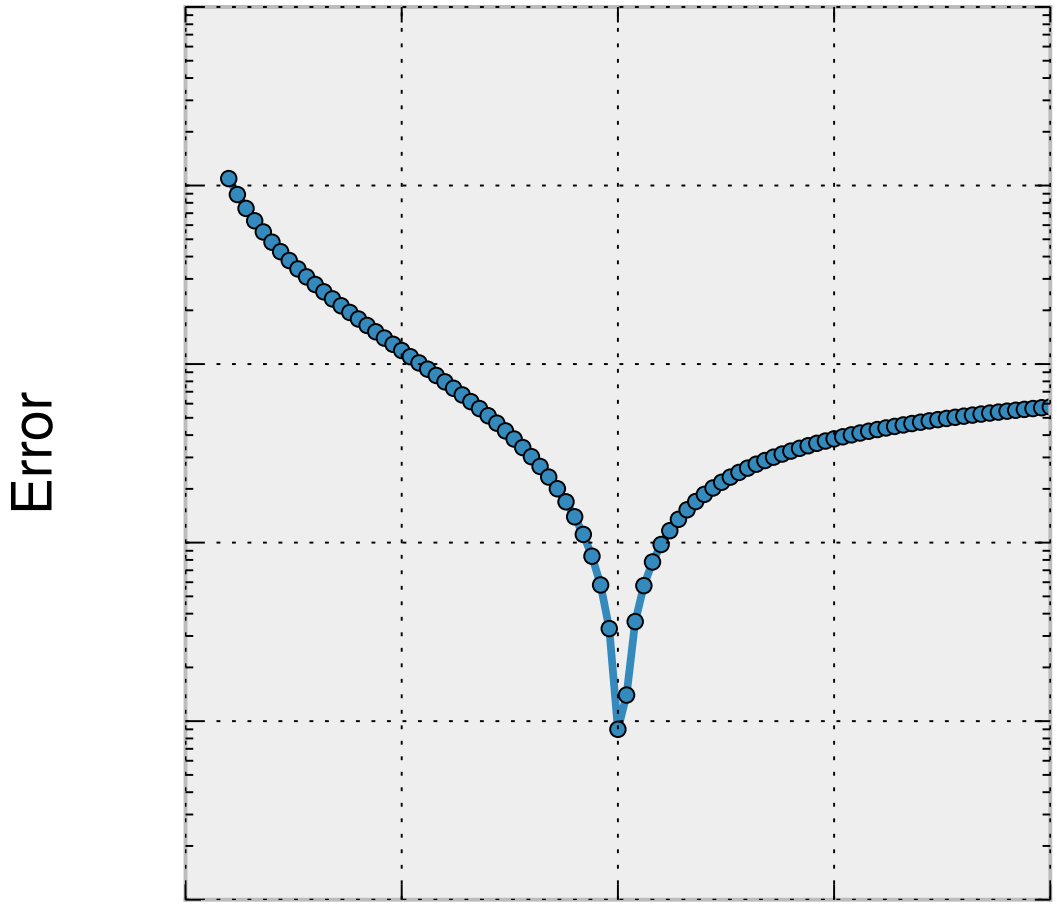

Figure 3.5: Sensitivity of the nonstandard finite difference scheme to τ^*. As the relaxation parameter τ^* approaches the relaxation time of the benchmark case the error reduces. The sharp cusp at $\tau^* = \tau_{\min}$ corresponds to the almost spectral accuracy of the time marching scheme for that case.

3.8.2 Rayleigh-Taylor test

We also consider the time evolution of the Rayleigh-Taylor benchmark described in Kaus et al. (2010). In this benchmark a dense, viscous layer with a sinusoidal initial perturbation drips into a less dense, less viscous mantle. The benchmark setup is shown in Figure 3.6. In all cases we use adaptive mesh refinement with five global refinement levels and four adaptive refinement levels, corresponding to ∼1 km cells at the most refined level. We refine according to compositional gradients, as well as near to the free surface.

Figure 3.7 shows the maximum depth of the interface between the dense and light fluid through time. The blue line shows the results using forward Euler timestepping with a very small timestep of 500 yrs, and is used as a reference solution. Nonstandard finite difference timestepping and quasi-implicit timestepping both converge to the reference solution, though from different directions. For the nonstandard finite difference simulations we recomputed the value of the minimum relaxation time $\tau_{\min}$ every 50 timesteps using power iteration, and reset the value of τ^* to $\tau_{\min}$.

The behavior of the two schemes is similar, though at the same CFL number quasi-implicit timestepping is slightly more accurate. On the other hand, with our implementation we have found that nonstandard finite difference timestepping can allow for larger timesteps than quasi-implicit timestepping while remaining stable.

We also used the Rayleigh-Taylor benchmark to investigate the effect of making a poor choice for τ^*, shown in Figure 3.8. We include four cases, all using adaptive timestepping with CFL=0.2. As a reference solution we include the case where we update τ^* to be equal to $\tau_{\min}$ every 50 timesteps, allowing for time variations in the viscosity and density structure to change the minimum relaxation time. We also show the case where we do not update τ^* over the course of the simulation, and two cases where we use the wrong value by a factor of two in either direction.

Over the course of the Rayleigh-Taylor benchmark, $\tau_{\min}$ varies by about 25%, as shown in Figure 3.8b. The case where we use the initial value of $\tau_{\min}$ for τ^* gives nearly identical results, whereas the cases where we choose values ∼50% off in either direction give significantly different (though not wildly so) results.

In many simulations we expect that the geometry, density, and viscosity structure of the model will not change enough that the τ^* would need to be updated frequently (if ever).

3.8.3 Mesh adaptivity

We also investigate the advantages of combining adaptive mesh refinement with free surface computations. Crameri et al. (2012a) performed a community benchmark of a setup for which there is no analytic solution. In this benchmark, a buoyant blob rises beneath a viscous lid with a free surface, deflecting the boundary upwards, reminiscent of the dynamic topography due to a rising plume (for the full setup, see Crameri et al. (2012a)). Figure 3.9 shows the convergence of the maximum topography at 3 Myr to its value in a high resolution simulation, both with and without adaptive mesh refinement.

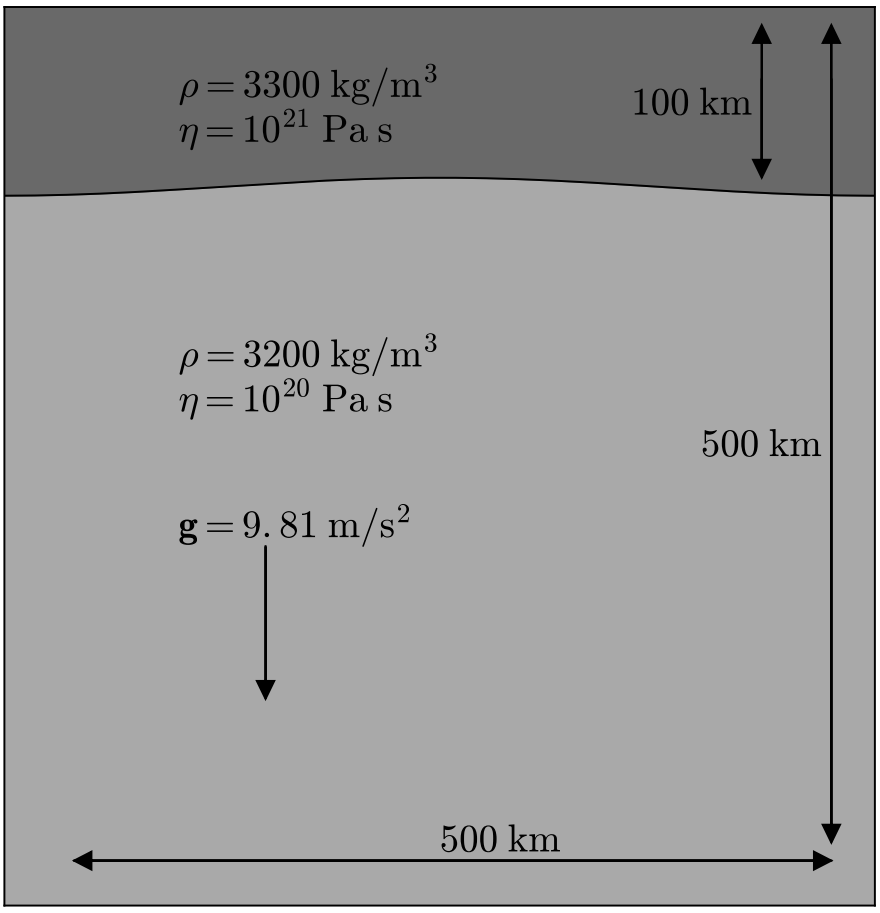

Figure 3.6: Setup for the Rayleigh-Taylor test. A denser, more viscous layer of lies on top of the mantle. The overlying layer has a thickness of 100 km, and a sinusoidal perturbation on its base with and amplitude of 5 km.

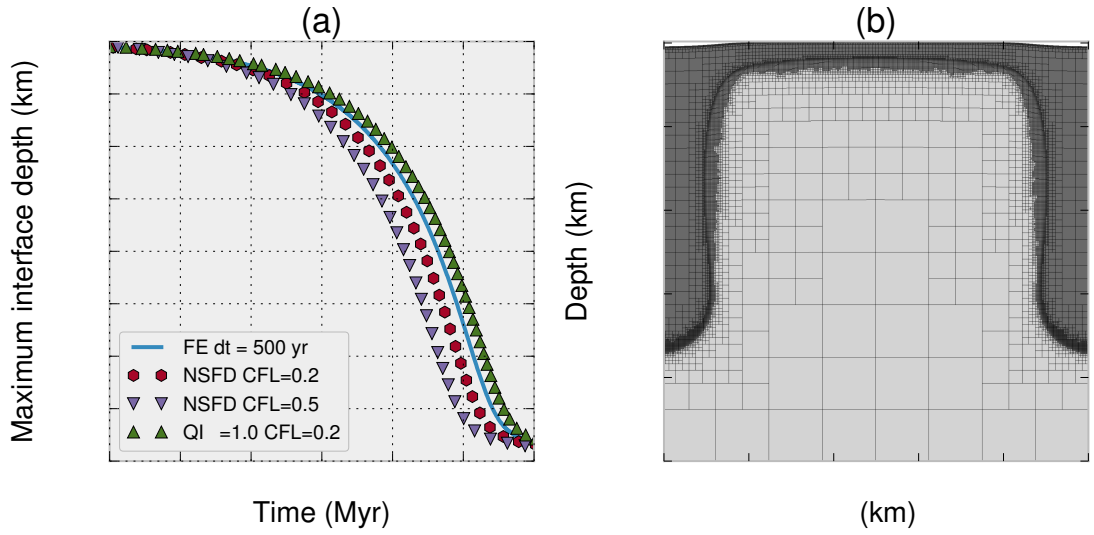

Figure 3.7: Rayleigh-Taylor test. (a) Maximum depth of the drip. The blue line is the result using forward Euler (FE) integration of the free surface with a small 500 yr timestep, and is used as a reference solution. The symbols are for several different runs with different timestepping parameters, using both quasi-implicit (QI) and nonstandard finite difference (NSFD) schemes. As the timestepping gets smaller, both schemes converge to the reference solution (though from different directions). (b) Result of the small timestep forward Euler simulation after 5 Myr, including the adaptive mesh.

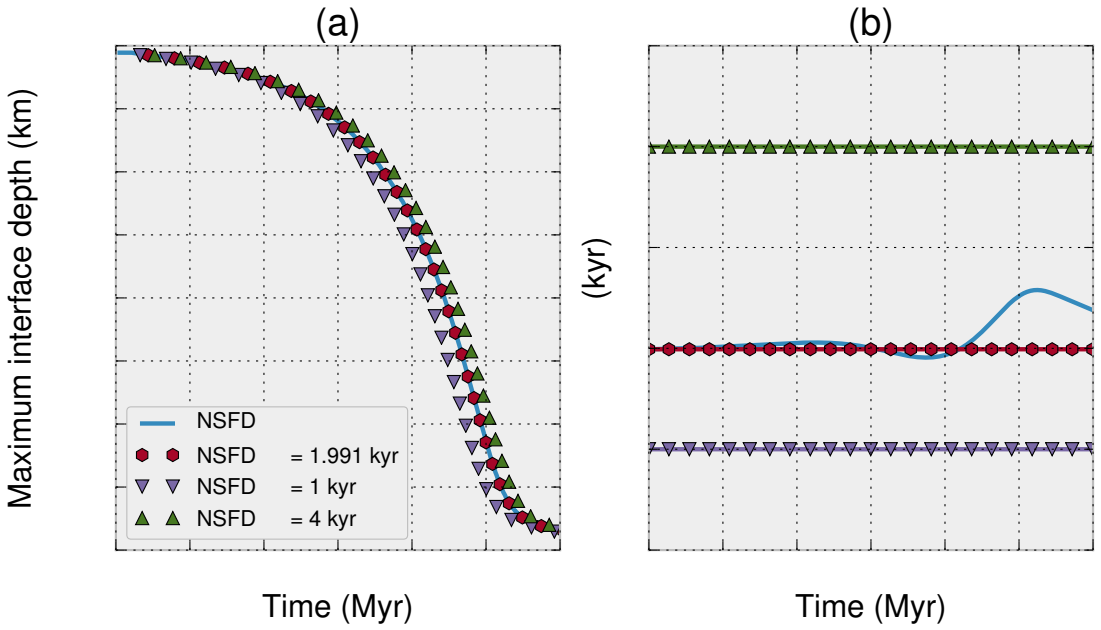

Figure 3.8: Effect of the choice of τ^* on the Rayleigh-Taylor test. (a) Maximum depth of the drip. In all cases adaptive timestepping is used with CFL=0.2. The blue line serves as a reference solution, and shows the result when the smallest relaxation timescale $\tau_{\min}$ is recalculated every 50 timesteps, and then the stabilization timescale τ^* is set to that value. The red hexagons show the result when we do not update τ^*, instead keeping it at the inital value of $\tau_{\min}$. The results are indistinguishable from those of the first case. The triangles show the results when we make a poor choice of τ^*, by a factor of two in either direction. In these cases there is a significant difference from the reference solution. (b) Evolution of the minimum relaxation timescale over the course of the simulation. It does experience significant changes, but not by orders of magnitude, so it is unsurprising that using the initial value is sufficient for this case.

For the uniform refinement cases each point is generated by running the benchmark with a different global refinement level. For the adaptive case each point is generated by allowing the mesh to be refined according to gradients in density and composition, where the maximum refinement level is limited to the same refinement level of the corresponding global refinement simulation. In both the uniform and the adaptive cases, the smallest cell size in the most refined case is $\sim$1 km. We refine every ten timesteps according to gradients in the density and compositional fields.

We run simulations using both quasi-implicit and nonstandard finite difference schemes for the free surface. We use a very small timestep for this test of 500 yr (note that this is significantly smaller than the smallest relaxation time of $\sim$ 14 kyr), so most timestepping schemes should be stable and accurate, including forward Euler. We choose this step for two reasons: (1) The primary purpose of this test is to investigate the savings due to using adaptive mesh refinement with a free surface, and (2) Crameri et al. (2012a) found that a timestep of several hundred years was required to achieve full convergence.

The convergence with and without adaptive mesh refinement have essentially the same behavior, but the adaptive case requires fewer degrees of freedom by a factor of approximately an order of magnitude. More complex models will have more detail and so we may be less able to aggressively coarsen them, but we still expect that adaptive mesh refinement will result in significant computational savings.

3.9 Conclusion

We have analyzed stability of free surface boundary conditions in geodynamic simulations and demonstrated the cause of sloshing instabilities using a normal mode analysis. This perspective on the problem allowed us to construct an explicit finite difference scheme which is first order accurate in time and is unconditionally stable. The nonstandard finite difference scheme is simple to implement, and requires no modifications to the system matrix.

The normal mode perspective on the problem also provides insights into the effect of the quasi-implicit stabilization scheme proposed by Kaus et al. (2010). The relaxation time of each mode is lengthened by an amount $\theta\Delta t$, and the maximum allowable timestep is correspondingly lengthened.

It is not clear that the non-standard finite difference scheme is superior to the quasi-implicit scheme. For $\theta = 0.5$ the quasi-implicit scheme is more accurate, but has a smaller stability region. For $\theta = 1$ the two schemes are comparably accurate, with a slight advantage to the quasi-implicit scheme. However, we have found that the nonstandard finite difference scheme allows for larger stable timesteps, if the modeler is willing to pay the price of reduced accuracy for a particular simulation.

Finally, we have described the implementation of free surface boundary conditions in the open source mantle convection software `ASPECT`. Both the quasi-implicit scheme and the nonstandard finite difference scheme are available. The implementation is sufficiently general to accommodate many different geometries, rheologies, and gravity models. Furthermore, it

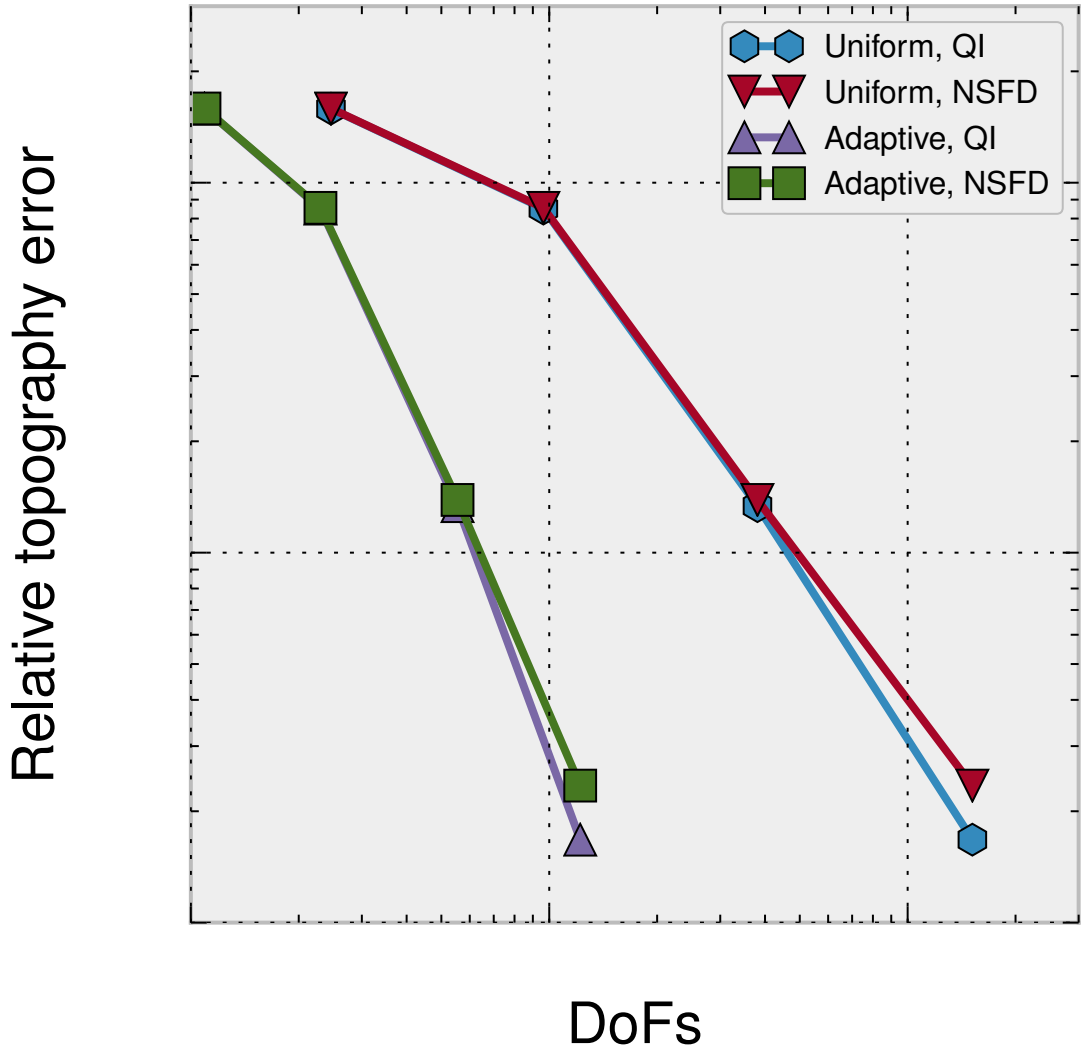

Figure 3.9: Convergence with degrees of freedom (DoFs) for the Crameri et al. (2012a) Case 2 benchmark, for both uniform and adaptive mesh refinement. The timestep Δt is 500 yr. We compare the maximum topography at 3 Myr with its value at high resolution (∼398 m). For the adaptive cases we perform mesh refinement according to the sum of density and composition gradients. Quasi-implicit (QI) and nonstandard finite difference (NSFD) timestepping converge similarly, but the adaptive mesh refinement simulations require significantly fewer unknowns. For NSFD timestepping we used a τ^* of 14.825 kyr, as determined by an analytical solution of the long-wavelength relaxation time of the free surface for this particular model setup (Crameri et al., 2012a).

runs in parallel and with adaptive mesh refinement.

The improved understanding of free surface boundary conditions in geodynamic models will allow for modelers to make more informed choices about timestepping and free surface stabilization techniques for use in simulations related to dynamic topography, active tectonics, gravity anomalies, and geomorphologic processes.

3.A The relaxation spectrum is positive definite

On physical grounds, we expect the relaxation spectrum described in Section 3.3 to have only positive eigenvalues τ_i. An imaginary eigenvalue would have an oscillitory component, which we do not expect in creeping flows (oscillation being usually due to inertia). A negative eigenvalue would grow exponentially, which would violate conservation of energy. Here we demonstrate the positivity of the relaxation time spectrum. We could proceed with either the continuous or the discretized version of the governing equations, but choose the continuous form here. We begin with the homogeneous Stokes equation (Equation (3.3)):

$$\nabla \cdot (2\eta\varepsilon(\mathbf{u})) - \nabla p = \rho\mathbf{g}. \tag{3.52}$$

We can transform this into the mechanical energy equation by multiplying it by $\mathbf{u}$ and integrating over the domain:

$$\int_{\Omega(t)} \mathbf{u} \cdot \nabla \cdot (2\eta\varepsilon(\mathbf{u})) - \int_{\Omega(t)} \mathbf{u} \cdot \nabla p = 0. \tag{3.53}$$

Integrating by parts and applying boundary conditions yields

$$-\int_{\Omega(t)} 2\eta\varepsilon(\mathbf{u}) : \varepsilon(\mathbf{u}) + \int_{\Omega(t)} p\nabla \cdot \mathbf{u} - \int_{\Gamma_F(t)} \mathbf{u} \cdot \mathbf{T} \cdot \mathbf{n} = 0. \tag{3.54}$$

Where the integrals correspond to the viscous dissipation, the work done by pressure, and the work done by boundary stresses, respectively. Since we are using the incompressible approximation, the second integral is zero. On a true free surface the boundary stresses are zero, but we make the same approximation used in Equation (3.12) and map the stress onto the reference surface, finding

$$-\int_{\Omega(t)} 2\eta\varepsilon(\mathbf{u}) : \varepsilon(\mathbf{u}) + \int_{\Gamma_F(t)} \rho_0 g\zeta \mathbf{u} \cdot \mathbf{n} = 0. \tag{3.55}$$

We can now eliminate ζ from the equation in the same way that was used in Equation (3.15), thereby introducing the relaxation time τ_i:

$$-\int_{\Omega(t)} 2\eta\varepsilon(\mathbf{u}) : \varepsilon(\mathbf{u}) + \tau_i \int_{\Gamma_F(t)} \rho_0 g(\mathbf{u} \cdot \mathbf{n})^2 = 0. \tag{3.56}$$

This equation may be solved for τ_i:

$$\tau_i = \frac{\int_{\Omega(t)} 2\eta\varepsilon(\mathbf{u}) : \varepsilon(\mathbf{u})}{\int_{\Gamma_F(t)} \rho_0 g(\mathbf{u} \cdot \mathbf{n})^2}. \tag{3.57}$$

The top and bottom of the right hand side are both strictly positive numbers so the τ_i must also be positive, demonstrating the positive definiteness of the system. A similar analysis can be performed for the discrete system. There is the possibility for velocities which do not move the free surface at all, in which case the bottom integral goes to zero, and the relaxation time becomes infinite. One example of this is the case of shear flow with a free upper surface and periodic horizontal boundary conditions. Since we are usually interested in the smallest relaxation times, these infinite eigenvalues are not usually a problem.

3.B Stability criterion of the NSFD scheme

We begin from Equation (3.38):

$$\left|1 - \frac{\tau^*}{\tau_i}\left(1 - e^{-\Delta t/\tau^*}\right)\right| \leq 1. \tag{3.58}$$

Timestepping involves repeated multiplication by this quantity. In order for the scheme to be stable, this repeated multiplication must not tend to infinity. Taking the positive value of the absolute value yields the criterion of

$$-\frac{\tau^*}{\tau_i}\left(1 - e^{-\Delta t/\tau^*}\right) \leq 0, \tag{3.59}$$

which can be rearranged to find

$$e^{-\Delta t/\tau^*} \leq 1, \tag{3.60}$$

which is simply a statement that the timestep must be postive.

Taking the negative value of the absolute value yields

$$\frac{\tau^*}{\tau_i}\left(1 - e^{-\Delta t/\tau^*}\right) \leq 2 \tag{3.61}$$

which can be rearranged to find

$$1 - 2\frac{\tau_i}{\tau^*} \leq e^{-\Delta t/\tau^*}. \tag{3.62}$$

For positive τ_i and τ^* the left hand side is strictly less than one. If the left hand side of Equation (3.62) is less than zero, then the stability criterion is true regardless of step size, which occurs when

$$\tau^* \leq 2\tau_i. \tag{3.63}$$

This is Equation (3.39). If the left hand side of Equation (3.62) is between zero and one, the expression is more complicated. Taking the log of both sides:

$$\Delta t \leq -\tau^* \log\left(1 - 2\frac{\tau_i}{\tau^*}\right). \tag{3.64}$$

This is Equation (3.40). It can be convenient to express this in terms of the dimensionless quantities $\Delta t/\tau_i$ and τ^*/τ_i:

$$\frac{\Delta t}{\tau_i} \leq -\frac{\tau^*}{\tau_i} \log\left(1 - 2\frac{\tau_i}{\tau^*}\right). \tag{3.65}$$

Chapter 4

Bayesian inversion for paleomagnetic reconstruction and plate kinematics

4.1 Introduction

Plate tectonics is the motion of near-rigid blocks of lithosphere across the surface of Earth, separated by narrow regions of deformation in spreading centers, transform faults, and subduction zones. The rigidity of plates means that the motion of most of Earth's surface can be described by a set of Euler poles which specify the position and magnitude of the rotation axis for a given plate (cf. Cox and Hart, 2009). Individual points on a plate undergoing rigid rotation are described by small circle paths.

Euler poles are ubiquitous in describing current plate motions (e.g. DeMets et al., 1990; Argus et al., 2011) due to their simplicity and compactness. Furthermore, there are good reasons to think that plate motions remain constant, or approximately so, over millions to tens of millions of years. This consistency of motion is most dramatically seen in the shape of oceanic fracture zones and in hotspot tracks across the lithosphere. These features form gently curving arcs over large portions of Earth's surface which are well described by small circles, consistent with finite Euler rotations of the plate for an extended period of time. As such, the combination of an Euler pole plus a time interval for which it is active (often called a "stage pole") is a convenient description of plate motions through Earth history.

The stage pole description of plate motions is therefore a convenient way of reconstructing plate tectonic history, and is widely used in both continental reconstruction (e.g. Boyden et al., 2011) and in geodynamical modeling (e.g. McNamara and Zhong, 2005; Bull et al., 2014; Rudolph and Zhong, 2014). Most reconstructions of plate motions over the past 200 million years rely heavily on fitting Euler pole rotations to oceanic fracture zones, hotspot tracks, seafloor magnetic isochrons, and, to a lesser extent, paleomagnetic data (Müller et al., 1993; Seton et al., 2012). However, as we look further back in Earth history, many of the records on which these plate tectonic reconstructions rely largely disappear due to the subduction of oceanic lithosphere. Before ∼200 Ma there is no record of oceanic crust, and the paleomagnetic record from continental rocks is the dominant remaining evidence.

It is more challenging to reconstruct past plate motions from the paleomagnetic record for a number of reasons, including (1) the data are often sparser, (2) traditional paleomagnetic analysis constraints paleolatitude and the orientation of the continental block but has no way of constraining paleolongitude without additional assumptions, and (3) some paleomagnetic poles have poor age control.

Gordon et al. (1984) noted that apparent polar wander paths (APW paths) have arcing trajectories similar to fracture zones and hotspot tracks, which is to be expected if similar tectonic processes are responsible for creating them. They therefore suggested fitting small circles to paleomagnetic poles tracks, which would furnish Euler poles for the plate in question for that time period. This model for understanding APW paths, called paleomagnetic Euler pole (PEP) analysis, has the attractive feature of providing a complete description of the plate motion, including paleolongitudinal changes and speeds. However, it has the drawback of being somewhat difficult to estimate, uncertainties in the fit were not easily computed, and it did not incorporate age uncertainties. A rigorous treatment of the uncertainties requires significant computational effort. With a few exceptions (e.g. Beck, 1989; Tarling and Abdeldayem, 1996; Bryan and Gordon, 1986; Beck and Housen, 2003; Smirnov and Tarduno, 2010), PEP analysis has not seen wide adoption.

Herein we extend paleomagnetic Euler pole analysis by placing it within a Bayesian statistical framework, and demonstrate how to invert for PEPs using Markov Chain Monte Carlo (MCMC) methods. This framework has the advantage of naturally incorporating uncertainties in the paleomagnetic pole positions, as well as widely disparate age uncertainties that commonly occur in APW paths. The resulting stage poles for which we invert are not a single answer, but are instead a distribution of possible answers, furnishing uncertainties as part of the solution process. Iaffaldano et al. (2012) employed a similar Bayesian approach to inverting for finite plate rotations. They used seafloor data to reconstruct India's Cenozoic convergence with Asia, incorporating uncertainty sources into the inversion.

The paper is organized as follows: in Section 4.2 we review different approaches for interpreting APW paths. In Section 4.3 we describe the formalism of Bayesian inversions and Markov Chain Monte Carlo methods. In Section 4.4 we describe the statistical model which we will be inverting. In Section 4.5 we demonstrate the inversion on several synthetic data sets. In Sections 4.6 and 4.7 we show examples using paleomagnetic data from Australia and Laurentia, including interpretations of plate speeds.

4.2 Interpretation of APW paths

A sequence of paleomagnetic poles from the same continental block form an APW path, which can then be used to develop plate tectonic reconstructions and models of plate speeds through time. Interpretation of these paths becomes difficult in the case of limited, highly uncertain, or conflicting data, and when the age of paleomagnetic poles are poorly known. A number of approaches to dealing with uncertainty in APW paths have been developed, which we briefly review here by.

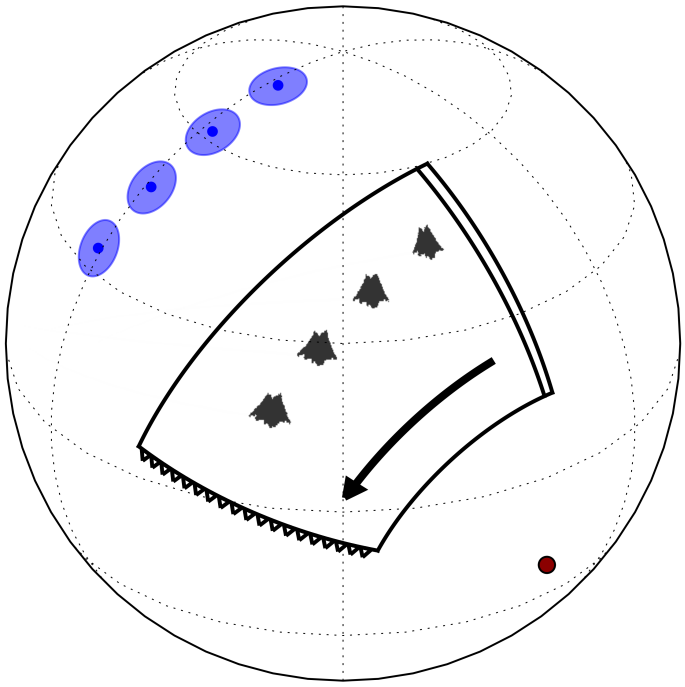

Figure 4.1: Conceptual model for a paleomagnetic Euler pole. A finite rotation of the plate around an Euler pole (red circle) results in long, arcuate oceanic fracture zones and hotspot tracks which describe small circles on the globe. The same finite rotation produces a small circle in the APW path, which is illustrated by blue paleomagnetic poles. By fitting a small circle to the APW path we may recover the Euler pole that produced the rotation. Adapted from Gordon et al. (1984)

4.2.1 Latitudinal drift

Due to the rotational symmetry of Earth's dominantly dipolar magnetic field, paleomagnetic poles do not directly constrain the paleolongitude of the continental block in question (Butler, 1992). The simplest analysis of an APW path is thus to compare the paleolatitudes implied by successive poles. The difference in paleolatitudes gives a minimum angular distance over which the block has traveled. If the two poles are well-dated, this difference also furnishes a rate of latitudinal motion.

It is also possible to estimate confidence bounds on the rate of latitudinal drift by bootstrap resampling (e.g. Tarduno et al., 1990) or by taking a Monte Carlo approach. Swanson-Hysell et al. (2014b) generated samples from Fisher distributions for a pair of poles from the Proterozoic Midcontinent Rift of North America to estimate the range of implied latitudinal drift rates. They also sampled from the age uncertainties, assuming Gaussian distributions on the radiometric dates, which incorporated the age uncertainties of the poles. With samples of pole position and ages, they were able to estimate the 95% confidence estimates on the rate of latitudinal drift.

Whether using point estimates of the latitudinal drift rate or using Monte Carlo estimates, the latitudinal drift interpretation of APW paths remains limited as it represents a minimum estimate. It has no control over longitudinal drift rate, nor does it naturally extend to APW paths with more than two poles, especially if two coeval poles are not in agreement.

4.2.2 Spherical splines

When considering APW paths with many poles, it becomes more difficult to perform latitudinal comparisons between pairs of poles. It is not always clear which pairs of poles to compare in cases where there are many overlapping paleomagnetic poles, often of unclear age progression and variable reliabilities.

One approach to deal with these uncertainties is to fit a spline through the set of paleomagnetic poles, constraining the path to lie on the surface of a sphere. This approach was pioneered by Torsvik et al. (1992) using the spherical spline algorithm developed by Jupp and Kent (1987). This approach has the advantage of allowing the weighting of the data by their uncertainties. The uncertainty assigned to a paleomagnetic pole can be the 95% confidence interval on the pole, but it can also be augmented by various quality screening factors, such as the quality ("Q") factor of Van der Voo (1990) (Torsvik et al., 1992). Even with the weighting of the paleomagnetic poles by uncertainty there can be unrealistic loops in the APW path generated by the spline fit. To combat this, the spline can also be computed under tension, penalizing curvature and producing a smoother path (Torsvik et al., 1996).

The spherical spline approach to interpreting APW paths has several attractive features. It produces a smooth path through the data, incorporates spatial uncertainties in the data, and may be efficiently computed. However, it does have some drawbacks. It is not easy to determine the appropriate uncertainty weighting and spline tension parameters for the fit,

and what effect those choices have on the result. Furthermore, the resulting fit does not have an uncertainty with a physically interpretable meaning (Torsvik et al., 1996). It also does not have a simple way of incorporating age uncertainties of the paleomagnetic poles. Finally, by their very nature, splines cannot represent the sharp hairpin cusps that characterize the abrupt shifts in motion that plates sometimes undergo (Irving and Park, 1972; Gordon et al., 1984).

4.2.3 Running means

An alternative method for developing APW paths is to perform a running Fisher mean on the poles with a moving window (Van der Voo and Torsvik, 2001; Torsvik et al., 2008). In such an analysis, paleomagnetic poles in a compilation are averaged in steps of 1-10 Myr with a 10-30 Myr window size. Like spherical splines, the running mean approach has the ability to effectively damp the effect of outlier poles that could lead to spurious loops in the APW path, with the width of the moving window controlling the amount of smoothing. Furthermore, it enforces an age progression in the averaged poles. Torsvik et al. (2008) also investigated the effects of combining running means with spherical splines, by first computing a set of mean poles and then fitting a spline through those means.

The running mean approach shares many of the drawbacks of the spline approach. It is not obvious how to best choose the window size, and different window sizes are likely appropriate for different data sets. It is also unclear how to interpret the resulting uncertainties in the path that are reported as the Fisher A_{95} ellipse of the mean of the poles. It, too, does not easily incorporate age uncertainties in the poles, nor the uncertainty in pole positions.

4.2.4 Paleomagnetic Euler poles

Paleomagnetic Euler poles (PEP, introduced in Section 4.1, also known as the "small circle" method, were first described by Gordon et al. (1984). The model rests in recognizing that plate motions are well described by finite rotations around Euler poles which are approximately steady for millions or tens of millions of years. As a result, the APW path of the plate can also be described by Euler rotations, which produce small circles on Earth's surface.

By fitting a sequence of Euler poles to a small circle path, one specifies the position of the Euler pole which produces that circle. PEP analysis has the feature that it closely conforms to our model for how plates move. Since it specifies the Euler pole which produces a given small circle, this allows for an estimate of the full motion of a given plate, as well as the total plate speed (instead of just the latitudinal component of the speed).

On the other hand, PEP analysis has many of the same deficiencies that spline fits and running means have: it is not easy to compute uncertainties, especially in the presence of unknown ages of poles. Furthermore, one has the additional challenge and related uncertainty of deciding how many PEPs to include for a given sequence of paleomagnetic poles. In the

following sections we develop a Bayesian statistical approach to PEP analysis which attempts to address some these deficiencies.

4.3 Bayesian inversion

4.3.1 A general description of inverse problems

The central question motivating inverse problems is "How probable is a particular model, given my observations?". We represent a vector of individual observations by the data vector $\mathbf{d}$, and a model by the vector of model parameters $\mathbf{m}$, so the above question can be expressed as the function $P(\mathbf{m}|\mathbf{d})$. Traditional frequentist approaches to an inverse problem often proceed by maximizing the likelihood function, defined by the probability of the data given a particular model (e.g Aster et al., 2005):

$$\mathcal{L}(\mathbf{m}|\mathbf{d}) \equiv P(\mathbf{d}|\mathbf{m}). \tag{4.1}$$

The likelihood function replaces something that is difficult to compute (namely, $P(\mathbf{m}|\mathbf{d})$) with something that is less difficult to compute. To compute $\mathcal{L}(\mathbf{m}, \mathbf{d})$ we need to have two things: a statistical model for uncertainties in the observations $\mathbf{d}$ and forward model that allows us to compute predictions. We denote the forward model by $\mathbf{g}$:

$$\mathbf{d}^p = \mathbf{g}(\mathbf{m}), \tag{4.2}$$

where the superscript "p" denotes a predicted value. If each of the observed data d_i are described by Gaussian random variables with standard deviations σ_i, the likelihood function is given by the product of the individual likelihoods of the observations:

$$\mathcal{L}(\mathbf{d}|\mathbf{m}) = \prod_i \exp\left(-\frac{(d_i - d_i^p)^2}{2\sigma_i^2}\right). \tag{4.3}$$

The likelihood function $\mathcal{L}$ is maximized by searching over the model parameter space. If the uncertainties in the observations are Gaussian, then maximizing the likelihood function is equivalent to the least squares solution (Aster et al., 2005).

A standard maximum likelihood fit will frequently overfit the observations, resulting in unrealistic solutions. In the context of APW paths, these overfit solutions may pass through every paleomagnetic pole, including less reliable ones, resulting in loopy or jerky paths. In order to address such overfitting, some form of regularization is usually included in the solution of the inverse problem, such as penalizing the magnitude or curvature of the solution. Both the running-mean and the spline under tension approaches to APW paths are a form of regularization on the problem.

4.3.2 Bayesian approach

The Bayesian approach to inverse problems takes a different strategy from the frequentist one. Rather than finding point estimates of a model fit, it treats the underlying model as a set of random variables with individual probability distributions. The probability distribution of the model $P(\mathbf{m}|\mathbf{d})$ given the data is then found by an application of Bayes theorem (cf. Sivia and Skilling, 2006):

$$P(\mathbf{m}|\mathbf{d}) = \frac{P(\mathbf{d}|\mathbf{m})\,P(\mathbf{m})}{P(\mathbf{d})}. \tag{4.4}$$

It is often unnecessary to calculate the denominator of Equation (4.4), which is just a normalization constant, leaving us with

$$P(\mathbf{m}|\mathbf{d}) \propto P(\mathbf{d}|\mathbf{m})\,P(\mathbf{m}). \tag{4.5}$$

The quantity $P(\mathbf{m}|\mathbf{d})$ is known as the posterior probability, and it represents our desired knowledge about the distributions of the parameters $\mathbf{m}$. The first factor on the right-hand-side of Equation (4.5) is identical to the likelihood function described in Section 4.3.1, and the second factor is known as the prior probability of the model.

The prior probability reflects the state of our knowledge and beliefs of the values of the model parameters prior to the consideration of our data. It also allows us to incorporate constraints that are not otherwise included in the forward model. In contrast with the classical statistical approach of regularization, the Bayesian inverse problem can (in effect) regularize the problem through the choice of prior distribution, by making choices of probability distributions that have less probability density in regions with less realistic values (Minson et al., 2013; Sambridge et al., 2013).

4.3.3 Markov chain Monte Carlo methods

It is usually impossible to calculate the posterior probability distribution in Equation (4.4) directly (Davidson-Pilon, 2015). It is much more tractable to generate a Markov chain which, upon convergence, generates samples from the desired posterior (Gelman et al., 2014). This approach defines a class of methods known as Markov chain Monte Carlo methods.

The literature on MCMC methods is extensive and we do not cover it here, but the interested reader can refer to Gelman and Rubin (1996), Sambridge et al. (2013), and Davidson-Pilon (2015). A number of high-quality open source software packages for implementing MCMC models exist, including WinBUGS (Lunn et al., 2000), PyMC (Patil et al., 2010), and Stan (Carpenter et al., 2016). We make extensive use of PyMC in this work.

4.3.4 Distributions on a sphere

In order to proceed with a Bayesian description of the problem, every parameter in the model should be described by some statistical distribution that determines the probability that the parameter takes a specific value. Parameters like pole ages can be described by

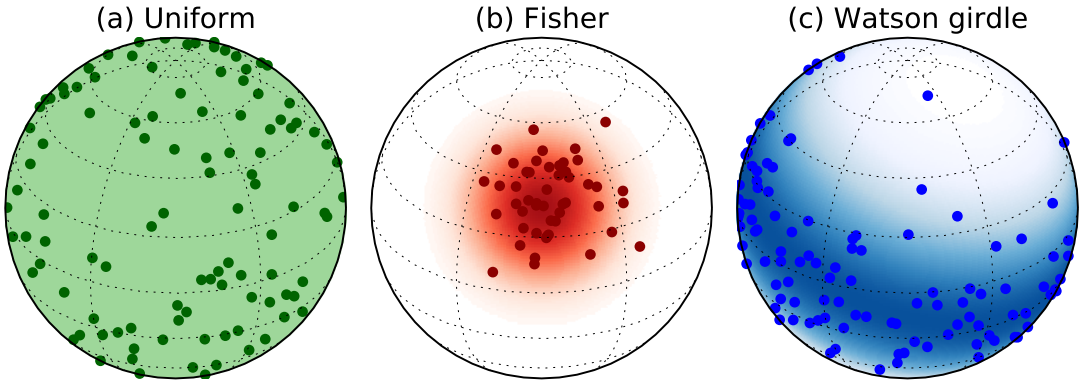

Figure 4.2: Probability densities for distributions of directional data, as well as samples drawn from them. All are plotted using an orthographic projection. (a) Uniform distribution. (b) Fisher distribution. The center of the distribution is at 30°N, 30°E, with concentration parameter of $\kappa = 20$. (c) Watson girdle distribution. The pole of symmetry is at 70°N, 90°E, with a concentration parameter of $\kappa = -5$.

familiar 1D probability distributions (such as uniform or normal distributions), whereas Euler pole locations are described by 2D distributions of directional data on the surface of a sphere. We review several of these distributions here. For a comprehensive discussion of spherical probability distributions, see Fisher et al. (1987). Plots of the following distributions, as well as samples drawn from them, are shown in Figure 4.2.

Uniform distribution

The simplest probability distribution on a sphere is the spherical uniform distribution. It has a probability density given by

$$\rho_U(\phi, \psi) = \frac{1}{4\pi}, \tag{4.6}$$

where ρ_U is the probability density, ϕ is the longitude, and ψ is the latitude (we will also refer to the Cartesian unit vector $\hat{\mathbf{x}}$ as a concise representation of ϕ and ψ). Most non-uniform distributions on a sphere reduce to the uniform distribution in some limit. We will use this distribution when we want to specify an uninformative prior distribution for directional parameters.

Fisher distribution

The Fisher distribution (also called the von Mises-Fisher distribution) is the analogue of a 2D normal distribution on a sphere. The probability density ρ_F at a point $\hat{\mathbf{x}}$ is given by

$$\begin{aligned}\rho_F(\phi, \psi; \kappa_F, \hat{\boldsymbol{\mu}}) &= \frac{1}{C_F} \exp\left(\kappa_F \hat{\mathbf{x}}^T \hat{\boldsymbol{\mu}}\right) \\ &= \frac{1}{C_F} \exp\left(\kappa_F \cos\theta\right),\end{aligned} \tag{4.7}$$

where κ_F is the concentration of the distribution, $\hat{\boldsymbol{\mu}}$ the unit vector for the mean direction of the distribution, and C_F is a normalization coefficient. It can be alternatively parameterized using θ, which is the angle between $\hat{\mathbf{x}}$ and $\hat{\boldsymbol{\mu}}$. The normalization factor is given by

$$C_F = \frac{\kappa_F}{4\pi \sinh \kappa_F}. \tag{4.8}$$

When κ_F goes to zero, the Fisher distribution is equivalent to the spherical uniform distribution.

The uncertainty of most paleomagnetic poles are calculated assuming a Fisher distribution, and we will use this distribution to calculate the likelihood function for pole directions in the model.

Watson girdle distribution

Whereas the Fisher distribution concentrates probability density near around a pole on the surface of the sphere, the Watson girdle probability distribution is concentrated in a belt orthogonal to the pole. It is useful for characterizing planar data, and is given by

$$\begin{aligned}\rho_W(\phi, \psi; \kappa_W, \hat{\boldsymbol{\mu}}) &= \frac{1}{C_W} \exp\left(\kappa_W (\hat{\mathbf{x}}^T \hat{\boldsymbol{\mu}})^2\right) \\ &= \frac{1}{C_W} \exp\left(\kappa_W \cos^2\theta\right),\end{aligned} \tag{4.9}$$

where κ_W is the concentration of the girdle, C_W is a normalization coefficient, and the other parameters are identical to those in the Fisher distribution. The Watson distribution is girdle-shaped only when κ_W is a negative number, which is the only case we consider here. The normalization factor is given by

$$C_W = \left[{}_1F_1\left(\frac{1}{2}, \frac{3}{2}, \kappa_W\right)\right]^{-1}, \tag{4.10}$$

where ${}_1F_1()$ is Kummer's confluent hypergeometric function, which is available in most software libraries of special mathematical functions. As with the Fisher distribution, when κ_W goes to zero, the Watson distribution is equivalent to the spherical uniform distribution.

4.4 A model for PEP inversion

4.4.1 Forward model

A forward model describes how we generate predicted observations, given a set of model parameters (Equation (4.2)). The forward model for PEP analysis in this study is essentially unchanged from that of Gordon et al. (1984). We describe plate motions (and hence paleomagnetic pole motions) with a series of Euler poles. Each Euler pole has three parameters: a latitude, a longitude, and a rotation rate.

We also must specify the ages where we switch from one Euler pole to the next (the cusps, or "hairpins" of Irving and Park (1972)). In the context of parameter inversion these are often known as "changepoints."

Finally, we need a starting position on the globe, which, in practice, can be sampled from the Fisher distribution of the oldest paleomagnetic pole in the dataset. The starting point contributes two parameters (a latitude and a longitude).

Therefore, a model with n_e Euler rotations will have $3n_e$ parameters for the poles, $(n_e - 1)$ parameters for the changepoints, and 2 parameters for the starting location. The number parameters for which we are inverting is then given by

$$\begin{aligned} N &= 3n_e + (n_e - 1) + 2 \\ &= 4n_e + 1. \end{aligned} \tag{4.11}$$

For each Euler pole $\boldsymbol{\omega}_i$ the velocity $\mathbf{v}$ of a point $\mathbf{p}$ on the surface of the globe is given by

$$\mathbf{v} = \boldsymbol{\omega}_i \times \mathbf{p}. \tag{4.12}$$

Finite rotations can be performed by constructing Euler angle rotation matrices (cf. Goldstein, 1965). We generate synthetic paleomagnetic pole positions from the forward model by stringing together finite rotations through the stage poles until the age of the paleomagnetic pole is reached. These positions can then be compared to the actual paleomagnetic poles in our dataset.

4.4.2 Choice of prior distributions

Bayesian analysis requires us to specify prior probability distributions for each of the model parameters in the inverse problem. These distributions reflect our state of belief about the values of the parameters before we begin, and allow us the option of incorporating information otherwise not captured by the model. To avoid biasing the results of the model towards a specific posterior distribution, we usually try to choose prior distributions that are as uninformative as possible. Depending upon the context, and the type of parameter, that choice may vary. The central parameters in the paleomagnetic Euler pole problem are the Euler pole positions, the Euler pole magnitudes, the changepoints, the starting point, and the paleomagnetic pole ages, which we treat in turn. We use the notation $x \sim y$ to indicate that the parameter x is drawn from distribution y.

Euler pole directions: The first parameter we consider is the position of the Euler poles, which should be drawn from a spherical probability distribution. The least informative prior distribution for the i'th Euler pole is the uniform spherical distribution:

$$\hat{\boldsymbol{\omega}}_i \sim \rho_U. \tag{4.13}$$

essentially allowing the Euler pole to be anywhere on the globe with equal probability.

An interesting alternative choice is to inform our prior distribution for Euler pole position based on current plate motions. It has long been observed that, to first order, plate motions are well explained by slab-pull torques acting along subduction zones, and to a lesser extent, ridge push and continental keel effects (Forsyth and Uyeda, 1975; Gordon et al., 1978; Richardson, 1992). This observation is explained by the fact that plate tectonics is the surface expression of Earth's convection.

We can then ask the question of whether the Euler pole for a given plate is more likely to be on top of the plate (corresponding to a spinning motion for that plate) or far away from that plate (corresponding to motion across the surface of Earth). Given that tectonic plates are the surface expression of convection, we can hypothesize that the second possibility is more likely because a spinning plate has no divergence (i.e., spreading centers and subduction zones, (Forte and Peltier, 1987; Gable et al., 1991)). Without spreading centers or subduction zones the plate motion does not contribute to convection.

To test this hypothesis, we generated position samples on the surface of Earth and computed the angular distance between that point and the Euler pole for the plate in which that point resides. We used the NNR-MORVEL56 model for current plate motions Argus et al. (2011) and restricted our analysis to the fourteen largest plates. We then fit those angular distance samples to a Watson girdle distribution (Equation (4.9)), inverting for the concentration parameter κ_W. If an Euler pole position has no preference for being a particular angular distance from a point on a plate, then κ_W should be close to zero, corresponding to a uniform distribution. We find that the distribution is best fit with $\kappa_W \approx -0.8$, which corresponds to the Euler pole probability density being roughly twice as large 90° away from a given point than on top of the point (see Figure 4.3).

Euler pole magnitudes: The magnitude of each Euler pole is a strictly positive number, specifying the rotation rate of that pole (negative rotations can be accommodated by flipping an Euler pole to the antipode). There are several possibilities for the prior distribution for the rates. In order to not bias the inversion towards a particular rate, we can choose a uniform prior distribution with large support:

$$|\boldsymbol{\omega}_i| \sim U(0, 4), \tag{4.14}$$

where $U(\cdot, \cdot)$ is a uniform distribution between two values, and is specified in degrees per Myr. Typical rotation rates for present day plate motions are under 1°/Myr (Argus et al., 2011), which corresponds to rates of about 11 cm/yr at a position 90° from the pole.

Another option is to choose a weakly informative prior distribution for the Euler pole magnitudes informed by recent plate motions (similar to the Watson girdle prior distribution

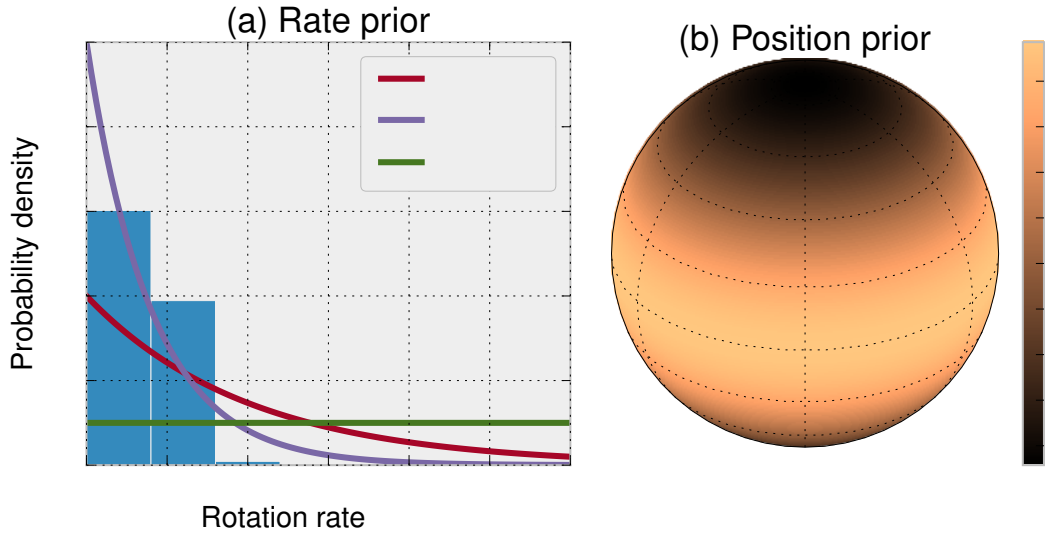

Figure 4.3: Informative prior distributions for Euler poles. (a) Prior probabilities for rotation rates. The histogram is the angular rotation rate from one thousand samples from the surface of Earth, using the NNR-MORVEL56 model. A fit to this sample set with an exponential distribution yields a scale parameter of $\lambda \approx 2.5$. We also show the distribution for $\lambda = 1.0$, which imposes less regularization on the rate, and a uniform $U(0, 4)$ distribution, which has no preference for slower speeds. (b) Prior probability density for the position of the Euler poles, with the north pole as the site latitude and longitude. We again sampled one thousand points on Earth's surface, calculating the angular distance between that point and the Euler pole for its plate. If we model the probability distribution as being drawn from a Watson distribution, then these angular distances correspond to colatitudes, where the pole is the sampled point. Fitting the resulting angular distribution to a Watson girdle distribution finds $\kappa_W \approx -0.8$. Since the Watson distribution is rotationally symmetric, longitudes do not contribute to the fit. For $\kappa_W \approx -0.8$ the probability density is roughly twice as large at the equator as at the pole.

for the directions). Zahirovic et al. (2015) found, based on Cenozoic and Mesozoic plate reconstructions, that plate speeds much higher than 15 cm/yr were unlikely. A reasonable choice of distribution for strictly positive numbers is the exponential distribution, given by

$$\rho_E(|\boldsymbol{\omega}_i|) = \lambda \exp(-\lambda|\boldsymbol{\omega}_i|), \tag{4.15}$$

which has higher probability density at lower values, and falls off exponentially. We sampled the current plate rates on Earth's surface according to NNR-MORVEL56 and fit those to an exponential distribution. The best fitting scale parameter λ for current plate rates is $\lambda \approx 2.5$. Making this choice of prior distribution for Euler pole rotation rates can be seen as a form of regularization on plate speeds.

Changepoints: Changepoints occur sequentially between the oldest (at age $a_{\max}$) and youngest (at age $a_{\min}$) paleomagnetic poles. We choose a uniform distribution as a prior for

these changepoints:

$$c_i \sim U(a_{\min}, a_{\max}), \tag{4.16}$$

where c_i is the i'th changepoint.

Starting position: Finally, the starting position $\hat{\mathbf{x}}_{\text{start}}$ for the set of Euler pole rotations needs a prior distribution. We could choose another uniform distribution, but a more reasonable choice is to start from near the oldest paleomagnetic pole in the dataset. We therefore choose the Fisher distribution of the oldest paleomagnetic pole as a reasonable prior distribution for a start point:

$$\hat{\mathbf{x}}_{\text{start}} \sim \rho_F(\kappa_{F0}, \hat{\boldsymbol{\mu}}_{\mathbf{0}}), \tag{4.17}$$

where κ_{F0} and $\hat{\boldsymbol{\mu}}_0$ are the concentration parameter and mean direction of the oldest paleomagnetic pole in the dataset.

Pole ages: One of the major advantages of Bayesian analysis is the ability to naturally incorporate uncertainties in as many parameters as we need. Previous approaches to modeling APW paths have the drawback that they do not easily account for uncertainties in the age of paleomagnetic poles. In our approach, we can include age uncertainty by including the age of the poles and associated uncertainty as parameters in our model.

There are many different ways to constrain the ages of the geologic units from which we obtain paleomagnetic poles, including radiometric dating, biostratigraphy, magnetostratigraphy, cross-cutting relationships, and stratigraphic relations. Here we concentrate on poles that are either interpreted to be the age of a single radiometric date or are interpreted to be bracketed stratigraphically between two dates (derived radiometrically or by using other age control such as biostratigraphy). If a geologic unit has been radiometrically dated, we can model the age of the j'th paleomagnetic pole a_j as a normal distribution with mean μ_j and standard deviation σ_j:

$$a_j \sim N(\mu_j, \sigma_j), \tag{4.18}$$

where $N(.,.)$ denotes a normal distribution.

Frequently, however, the geologic unit from which we obtain a paleomagnetic pole is not well dated, but its age can be constrained to lie between those of well-dated units stratigraphically above and below it. In this case, we argue that a uniform distribution between those ages is a reasonable choice of prior distribution:

$$a_j \sim U(a_{\text{young}}, a_{\text{old}}), \tag{4.19}$$

where a_{young} and a_{old} are the ages of the lower and upper age constraints, respectively.

To summarize our choices for prior distributions:

- Euler pole positions: spherical uniform distribution, or a Watson girdle distribution with $\kappa_W \approx -0.8$.
- Euler pole magnitudes: Uniform distribution between 0° and 4°/Myr, or an exponential distribution with $\lambda \approx 2.5$.

- Changepoints: uniform distribution between $a_{\min}$ and $a_{\max}$.
- Paleomagnetic pole ages: normal or uniform distribution, depending on the type of age control for the geologic unit.

4.4.3 Likelihood

In addition to the choice of prior distributions we need a statistical description of the observations. This description will allow us to calculate the likelihood function, which, when combined with the prior distributions, allows us to evaluate Bayes' theorem (Equation (4.5)).

In the case of APW paths, our observations are paleomagnetic poles. The most common statistical distribution for describing paleomagnetic poles is the Fisher distribution (though others are possible, such as the Kent or Bingham distributions, c.f. Tauxe et al. (2010)). Given the set of model parameters $\mathbf{m}$ and the forward model $\mathbf{g}(\mathbf{m})$, described in Section 4.4.1, we can calculate the predicted paleomagnetic pole unit vectors $\hat{\mathbf{x}}_i^p$. For a set of n paleomagnetic poles, the likelihood is then given by the product of the probabilities of each observation:

$$P(\mathbf{d}|\mathbf{m}) = \prod_{i=1}^{n} \frac{1}{C_{F,i}} \exp\left(\kappa_{F,i} \hat{\mathbf{x}}_i^{pT} \hat{\boldsymbol{\mu}}_i\right). \tag{4.20}$$

4.5 Example inversions

Before proceeding with inversions for paleomagnetic Euler poles using real paleomagnetic data, it is useful to consider a few examples of inversions for synthetic datasets. We have implemented the forward model described in Section 4.4.1 in Python, and used the package PyMC (Patil et al., 2010) to perform the Monte Carlo inversion. We use a Metropolis-Hastings sampler, starting from a fit to the maximum a posteriori (MAP) probability. In most cases shown here we generate 10^6 samples, discarding the first 20% to avoid potential bias in the posterior due to a poor starting point. Our code for the inversions has an open-source GPL license and may be found at `https://github.com/ian-r-rose/mcplates`.

In all of the inversions we show here, we choose $\kappa_W = 0$ for the Watson concentration parameter in the Euler pole direction prior distribution (that is, equivalent to a uniform distribution on a sphere), and $\lambda = 2.5$ for the scale parameter in the Euler pole magnitude prior distribution.

4.5.1 One Euler rotation

We begin by trying to recover the Euler pole for a single rotation. We generate an idealized synthetic APW track of four poles by starting from a pole at 0° N, 30° E, and rotating around an Euler pole at 0° N, 0° E for 180 Myr at a rate of 1°/Myr. We produce paleomagnetic poles at 190 Ma, 130 Ma, 70 Ma, and 10 Ma, and prescribe A_{95} of 10° to each pole (where A_{95} indicates the 95% angular confidence interval for the pole position).

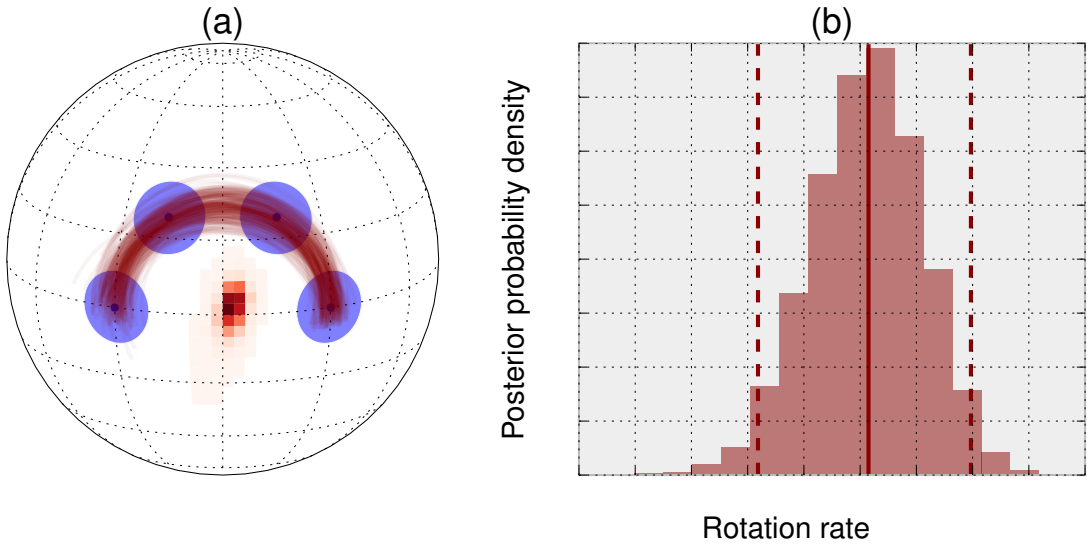

Figure 4.4: Inversion for a single paleomagnetic Euler pole. (a) Four paleomagnetic poles are generated during a net 180° rotation about an Euler pole at 0°N, 0°E over 180 Myr, for a rotation rate of 1°/Myr. The red distribution is the probability density function recovered by MCMC inversion, and the red lines are a sampling of 200 synthetic APW paths generated by the inversion. (b) Posterior probability density for the rotation rate of the Euler pole recovered by the inversion. The solid line shows the median of the distribution (1°/Myr), and the dashed lines show the 95% credible interval ($0.8° - 1.2°$/Myr).

The results of the inversion are shown in Figure 4.4. The Bayesian approach successfully recovers a posterior probability distribution for the position of the Euler pole that includes the start pole, as well as a rate that is centered near the true value of 1°/Myr (Figure 4.4). The posterior distribution for the rate has a highest posterior density (HPD) credible interval at 95% (which we abbreviate from here as a 95% credible interval) between 0.8°/Myr and 1.2°/Myr, reflecting the resolving power of the inversion for data with the given uncertainties.

4.5.2 Two Euler rotations

We next consider an inversion for an APW path with two stage poles. Unlike the example in Section 4.5.1, this inversion also requires a changepoint. We generate five paleomagnetic poles from a starting point at 0° N, 60° W. The first rotation is around an Euler pole at 41° N, 60° W, and rotates at 1°/Myr for 130 Myr. The rotation rotation is around an Euler pole at 41° N, 60° E, rotates at the same rate for the same amount of time. The "observations" produced by the two stage model are shown in Figure 4.5. The inversion successfully recovers the Euler pole positions and rates, and the changepoint is centered near 130 Ma.

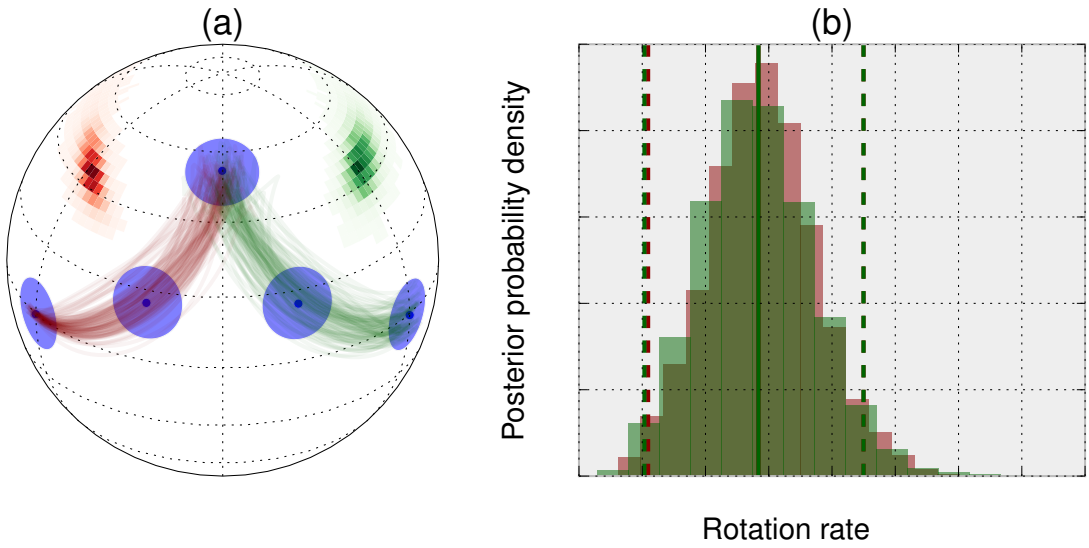

Figure 4.5: Inversion for two successive paleomagnetic Euler poles. (a) Five paleomagnetic poles are generated, beginning with a pole at 0°N, 60°W. The first Euler pole is located at 41°N, 60°W, and rotates at 1°/Myr for 130 Myr. The second Euler pole is located at 41°N, 60°E, and rotates at the same speed and for the same duration. The red and green distributions show the location of the first and second Euler poles (respectively) recovered by the MCMC inversion. The red and green lines are a sampling of 200 synthetic APW paths generated by the inversion. (b) Posterior probability density for the rotation rates of the Euler poles recovered by the inversion. The solid lines show the median values of the distributions ($\sim 0.97°$/Myr, and the dashed lines show the 95% credible intervals ($\sim 0.61° - 1.3°$/Myr). The two distributions are nearly identical, and centered on the true value of the rate.

4.5.3 Incorporating age uncertainty

A major benefit of the Bayesian approach to inverse problems is its great generality. As long as some effect can be described statistically and incorporated into our forward model, we can include it in the inverse problem.

In this case, we include uncertainties in the ages of the paleomagnetic poles. We use the same test case as in Section 4.5.1, but assign uncertain prior distributions to the ages of the poles. For the first and last poles we assume they are radiometrically dated with standard deviations of 2 Myr. However, we assume that the middle two poles have no age control, except that their respective rock units lie stratigraphically between the first and last poles. We thus assign Gaussian prior distributions to the first and last poles and uniform prior distributions to the middle two.

The primary effect of adding uncertainties to the ages of the poles is that they can help to constrain the location of the APW path without providing an unwanted constraint on the timing of the path. Figure 4.6 shows the prior and posterior distributions for the ages of the poles. We can see from the posterior distribution that the inversion successfully places the ages of the middle two poles at ~ 70 Ma and ~ 130 Ma, though with relatively wide 95% credible intervals. The posterior distributions for the Euler pole position and magnitude which we recover from this inversion are visually identical to those in Figure 4.4.

4.6 Application to Cenozoic Australian APW path

A first application of our model for PEP inversion is with the case of Cenozoic Australia. Australia's Cenozoic plate motions are relatively well constrained by oceanic fracture zones and hotspot volcanism (Müller et al., 1993; Seton et al., 2012). This gives us the opportunity to compare the results of our model to a one derived from an independent dataset.

The most reliable Cenozoic Australian paleomagnetic data comes from Idnurm (1985a) and Idnurm (1994). Additional paleomagnetic poles were developed prior to Idnurm's work, but they show considerably more scatter, and there are concerns that they do not adequately average secular variations (Idnurm, 1985a; Klootwijk, 2009). Idnurm (1985b) found that the latitude-age progression of the paleomagnetic data was significantly faster than that given by hotspot tracks. He proposed that the best explanation for this discrepancy was a long-lived departure of Earth's magnetic field from a geocentric axial dipole (GAD).

Here we reanalyze the available paleomagnetic data with our statistical model, which allows us to incorporate more recent models for Australia's plate motions and perform an accounting of the uncertainties within our Bayesian framework. The pole list we use is given in Table 4.1. We fit the paleomagnetic pole list to one and two PEPs, and compare them to the global plate motion model from Seton et al. (2012).

Figure 4.7 shows the results for a single Euler pole plotted on the globe, as well as modeled paleomagnetic poles drawn from the posterior distribution. Figure 4.8b shows the single Euler pole result plotted as latitude vs. age. Both the paleomagnetic data and the Seton et al. (2012) model show a speed-up in Australia's motion as it approaches the present

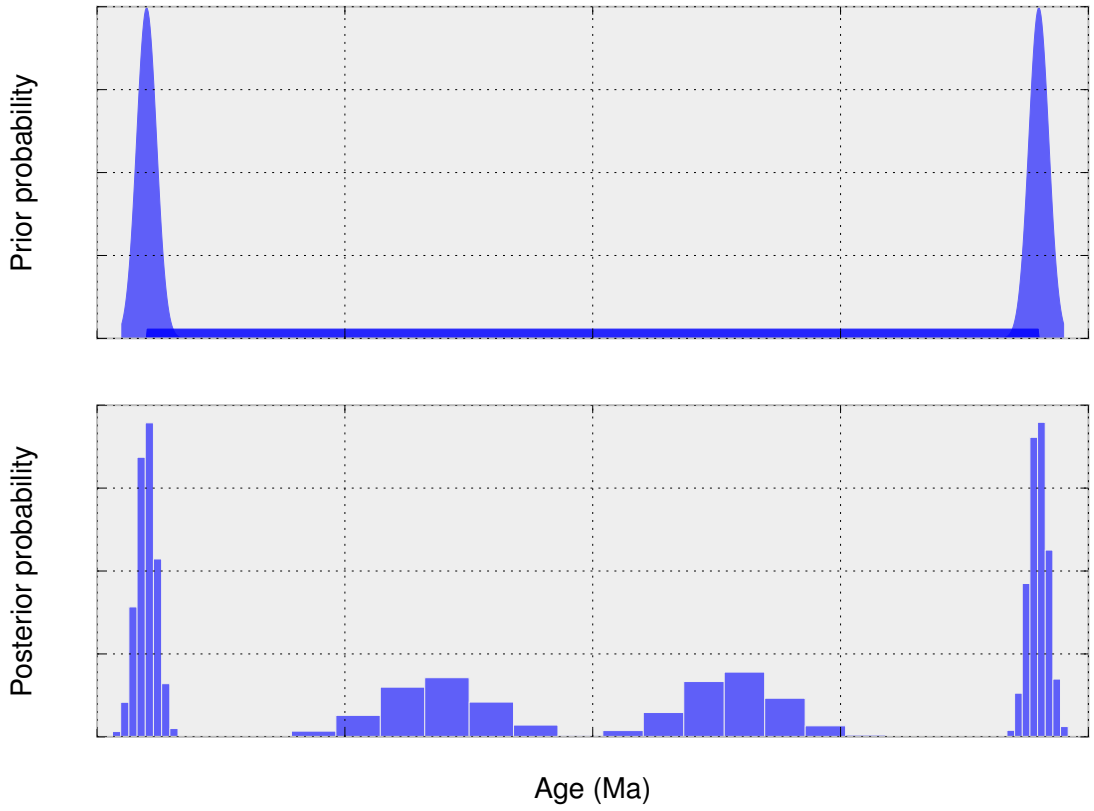

Figure 4.6: Probability distributions for the ages of the paleomagnetic poles in the one-Euler pole inversion test. Top: prior distributions. We presume the first and last poles to be radiometrically dated with one-sigma uncertainties of 2 Myr, and are assigned Gaussian prior distributions. The middle two poles are undated, and are only stratigraphically constrained to be between the first and last poles. Bottom: posterior distributions after 10^5 MCMC samples. The distributions of the first and last samples are largely unchanged, but the distributions for the middle two poles are centered on their true values of 70 Ma and 130 Ma. Importantly, the middle poles help to constrain the location of the Euler pole, but the wide prior distributions on their ages do little to constrain the rotation rates.

Pole	ψ_p	ϕ_p	A_{95}	Reference	Lower age (Ma)	Upper age (Ma)
Werriko Limestone, Newer Volcanics	83.2	283.6	6.2	Idnurm (1985a)	2	4
Port Campbell Limestone, Glenample Formation	77.2	303.5	4.2	Idnurm (1985a)	10	14
Point Addis Limestone	68.4	298.7	4.8	Idnurm (1985a)	23	28
Browns Creek Formation	65.5	292.5	2.5	Idnurm (1994)	34	39
North Rankin 1 Drillcore	61.7	298.4	5.1	Idnurm (1985a)	58	62

Table 4.1: Paleomagnetic poles used for the Australia inversion, as well as references. ψ_p and ϕ_p give the latitude and longitude of the mean pole position, and A_{95} gives the 95% angular confidence interval for that position. The paleomagnetic poles come primarily from sedimentary successions with biostratigraphic age control (with the exception of the Newer Volcanics, which erupted from $\sim 2-4$ Ma). Upper and lower age bounds come from estimates from Idnurm (1985a) and version 4.6 of the Global paleomagnetic database (GPMDB).

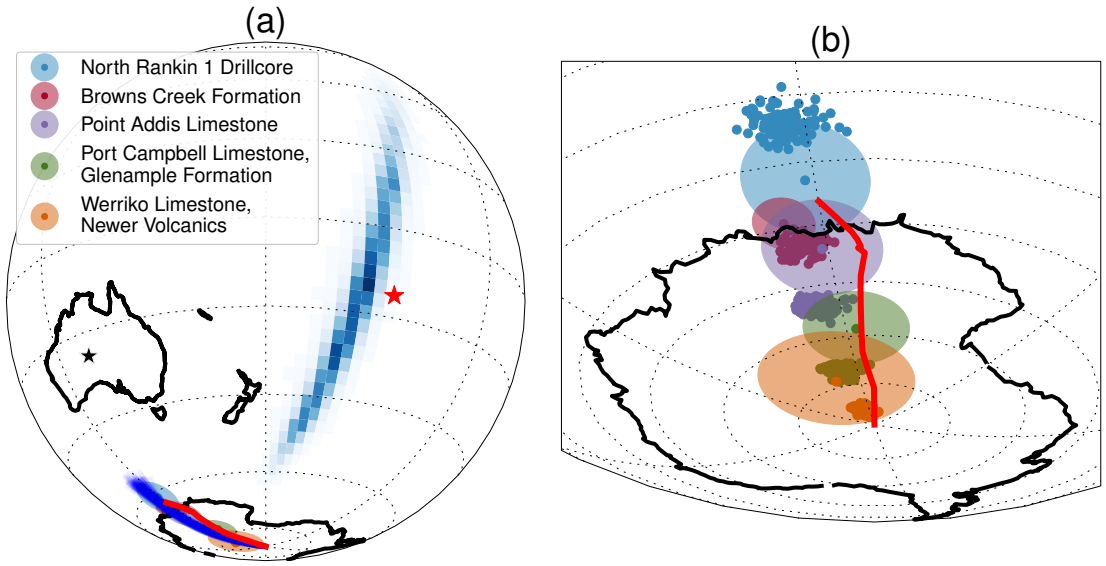

Figure 4.7: Australian Cenozoic APW path fit to one Euler rotation. (a) Euler pole position and sample tracks. The blue distribution shows the posterior distribution of Euler pole positions, and the blue paths show a sampling of paths drawn from the posterior. The red line shows the polar wander path derived from the global plate motion model of Seton et al. (2012), and the red star shows the average Euler pole from 0-60 Ma defined by the Seton et al. (2012) path. We calculate plate speeds referenced to Uluru, shown by the black star. (b) Paleomagnetic pole positions for draws from the posterior distribution of the inversion superimposed on observed pole positions and their uncertainty.

day, though the paleomagnetic data has systematically higher recent latitudes, implying faster plate speeds. While the single Euler pole fit does a reasonable job of fitting the azimuth of the plate motion model (Figure 4.7), it cannot fit a change in speed, and does not pass through all the paleomagnetic poles in Figure 4.8b.

The two-Euler pole inversion, shown in Figures 4.9-4.10 does a better job of fitting the paleomagnetic poles, preferring a change in speed at ~ 23 Ma. It shares some features with the Seton et al. (2012) model, including the overall azimuth and an increase in plate speed midway through the track. However, the $\sim 23 - 0$ Ma speeds are significantly faster than those from the global plate motion model, consistent with the conclusions of Idnurm (1985b). We conclude that the discrepancy between the Australian paleomagnetic data and Cenozoic plate motion models remains.

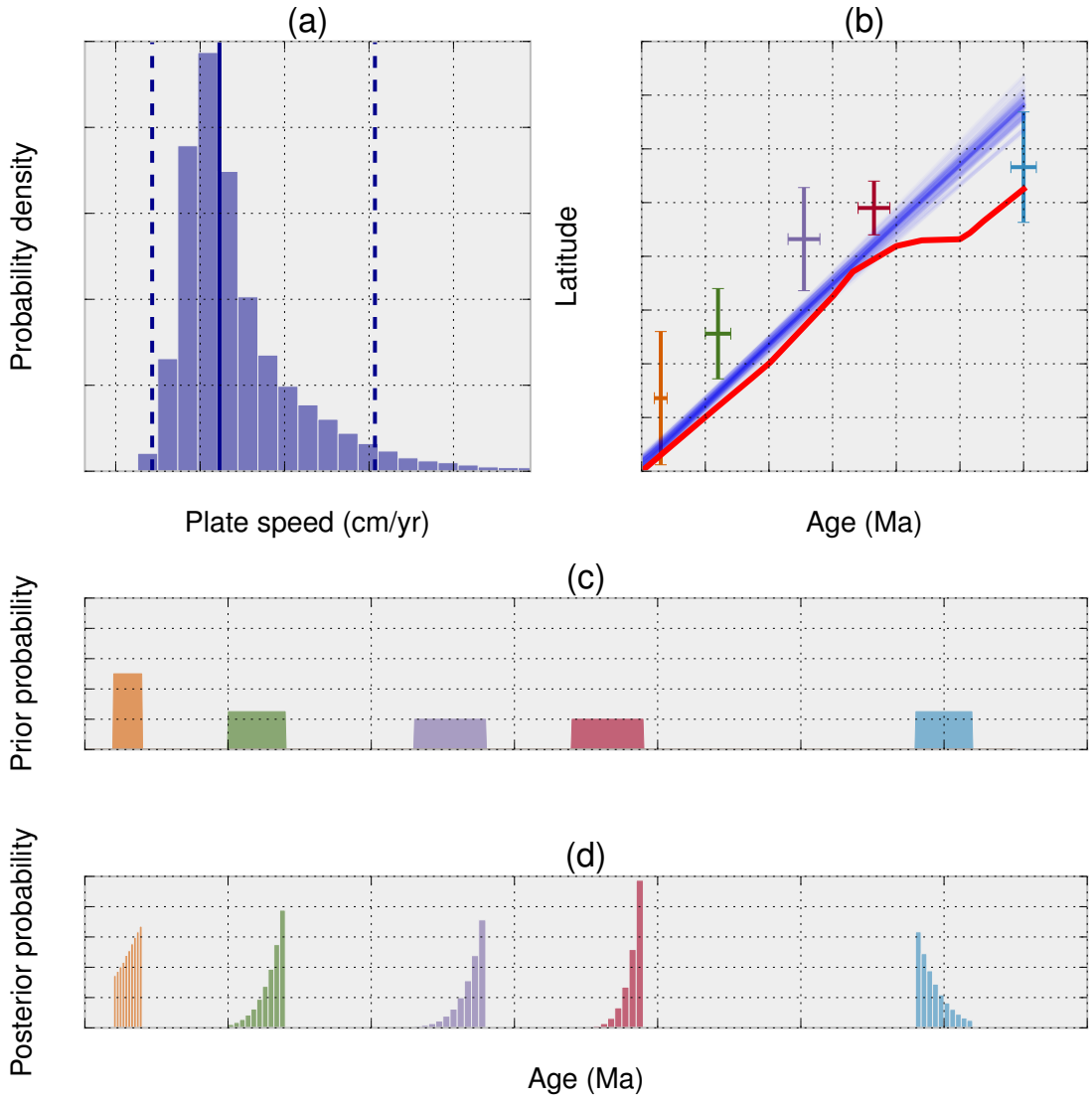

Figure 4.8: Results for Australian Cenozoic APW path with one Euler rotation. (a) Posterior distribution for plate speed. The solid line shows the median plate speed (6.2 cm/yr) and the dashed lines show the 95% credible interval (5.4-8.1 cm/yr). (b) Latitude vs. age. The paleomagnetic poles are shown as data points, with age and latitude uncertainty. The blue lines show a sampling of the posterior path distribution, and the red line shows the Seton et al. (2012) plate motion model. Note that the paleomagnetic poles are systematically above the Seton et al. (2012) model, and that the single Euler rotation path is not able to pass through all the data points. (c) Prior distributions for the ages of paleomagnetic poles. (d) Posterior distributions for the ages of paleomagnetic poles.

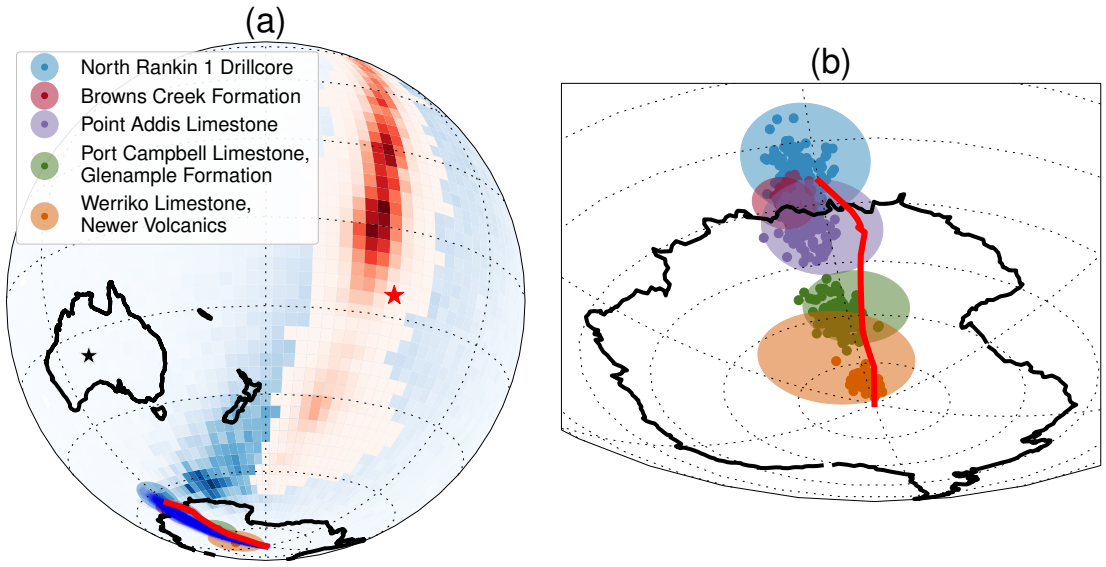

Figure 4.9: Australian Cenozoic APW path fit to two Euler rotations. (a) Euler pole locations and sample tracks. The blue distribution shows the posterior of positions for the first Euler pole, and the red distribution shows the posterior for the second Euler pole. The distribution of the first Euler pole is quite broad, reflecting the short length of the portion of the path that it is trying to fit (shorter paths provide less of a constraint on the position). The blue paths show a sampling of paths drawn from the posterior. As in Figure 4.7, the red line shows the polar wander path derived from the global plate motion model of Seton et al. (2012), and the red star shows the average Euler pole from 0-60 Ma defined by the Seton et al. (2012) path. (b) Paleomagnetic pole positions for draws from the posterior distribution of the inversion superimposed on observed pole positions and their uncertainty.

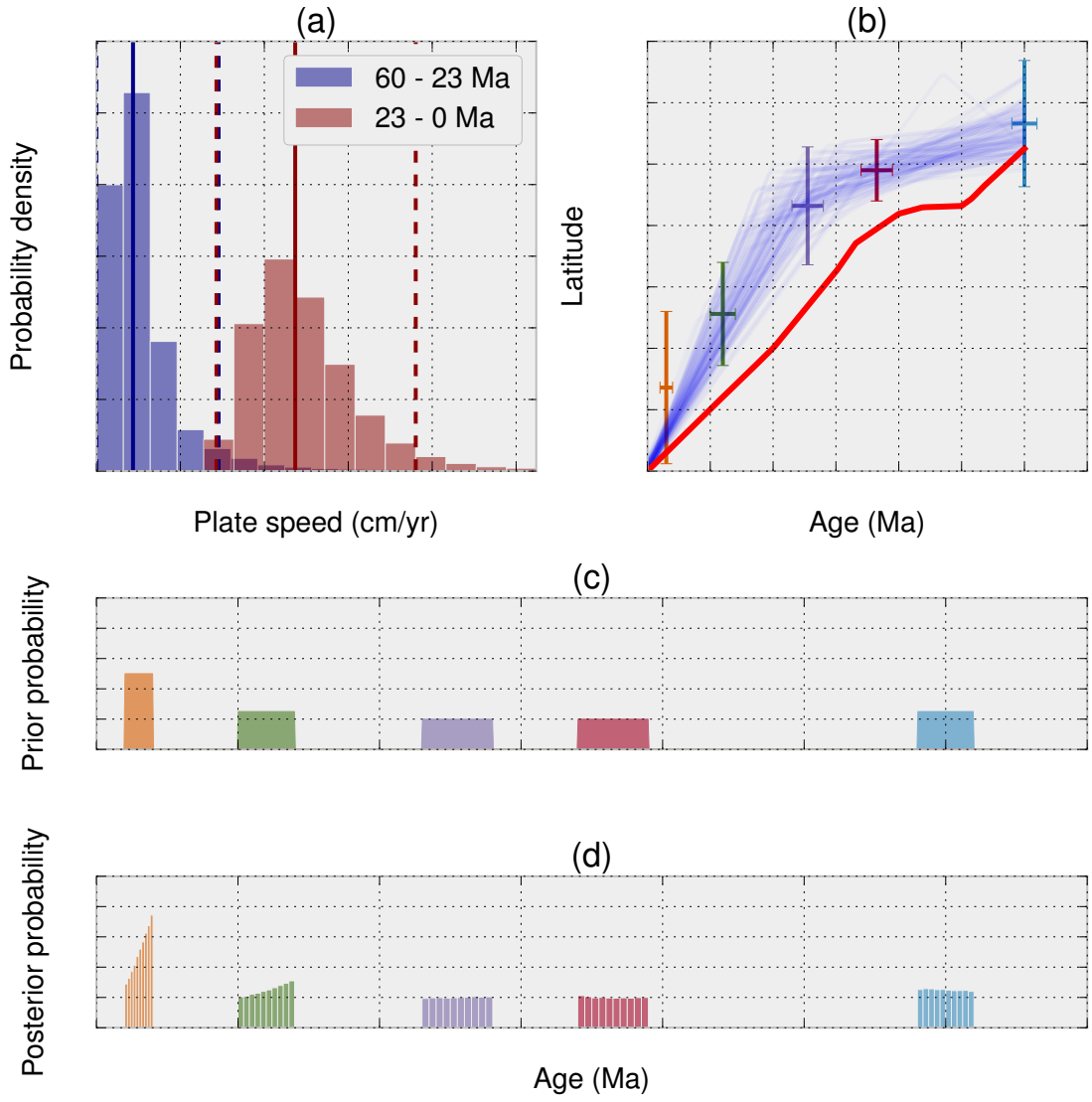

Figure 4.10: Results for Australian Cenozoic APW path with two Euler rotations. (a) Posterior distributions for plate speeds. The blue distribution shows the plate speeds for the first rotation, which occurs from approximately 60-23 Ma. The red distribution shows the plate speeds for the second rotation, which occurs from approximately 23-0 Ma. The changepoint is approximate, since it is also a random variable with its own posterior distribution. This inversion prefers a slow first rotation (2.2 cm/yr with a 95% credible interval of 0-7.3 cm/yr) and a fast second rotation (11.8 cm/yr with a 95% credible interval of 7.1-19 cm/yr). (b) Latitude vs. age. The paleomagnetic poles are shown as data points, with age and latitude uncertainty. The blue lines show a sampling of the posterior path distribution, and the red line shows the Seton et al. (2012) plate motion model. Compared to the single Euler pole fits (Figure 4.8b), the two Euler pole fit does a much better job of passing through the paleomagnetic poles. However, while the modeled APW paths are qualitatively similar to the Seton et al. (2012) path in shape, the 0-23 Ma segment rotates significantly faster (c) Prior distributions for the ages of paleomagnetic poles. (d) Posterior distributions for the ages of paleomagnetic poles.

4.7 Application to the Keweenawan track

4.7.1 Geologic context

The Keweenawan province is a Mesoproterozoic succession of volcanic and sedimentary rocks which outcrops in the region around Lake Superior, including on the Keweenaw Peninsula. The province represents the products of a failed rift zone in the middle of Laurentia which was active from about 1110 to 1080 Ma (Swanson-Hysell et al., 2014a; Fairchild et al., 2016). Geochronology and paleomagnetism from the Keweenawan province has been central to reconstructions of paleogeography and dynamics of the Mesoproterozoic Earth (e.g. Li et al., 2008; Evans, 2009).

Paleomagnetic studies of the Keweenawan province have long shown asymmetry between normal and reverse polarities of the magnetization, which has been interpreted to be a result of significant non-dipole behavior of Earth's magnetic field during the Mesoproterozoic (Pesonen and Nevanlinna, 1981; Nevanlinna and Pesonen, 1983; Pesonen and Halls, 1983). More recent high-resolution paleomagnetism has shown that the apparent reversal asymmetry is an artifact of temporal gaps in sampling (Swanson-Hysell et al., 2009; Kulakov et al., 2013). Instead, the paleomagnetic poles are symmetric with respect to polarity, but the paleomagnetic directions rapidly shallow over the course of the rifting period, corresponding to equatorward motion of Laurentia.

A consequence of this reinterpretation of the paleomagnetic data is that Laurentia's apparent polar wander rate, and thus its implied plate motion, is quite fast. A Monte Carlo approach (described in Section 4.2.1) by Swanson-Hysell et al. (2014b) found an implied latitudinal drift rate of ∼24 cm/yr, with a 95% confidence interval of 15.2-44.4 cm/yr. These rates are significantly faster than the fastest Cenozoic plate speeds (Zahirovic et al., 2015). Possible explanations for such fast rates include faster plate speeds in the Proterozoic (possibly due to decreased mantle viscosity in a hotter, younger Earth) or true polar wander (Swanson-Hysell et al., 2009).

Finally, there is some evidence from combined paleomagnetic/geochonologic studies that the APW rate during the Keweenawan rifting slowed down. Davis and Green (1997) inferred a change in minimum plate speed from ∼22 cm/yr to ∼8 cm/yr at around 1095 Ma. Similar conclusions were reached by Swanson-Hysell et al. (2009). However, more recent geochronology and paleomagnetism from the late stage volcanics of the Midcontinent Rift. Fairchild et al. (2016) have suggested that such a slowdown is not required, and that Laurentia's APW path had high rates throughout rifting.

4.7.2 Inversion for paleomagnetic Euler poles

We apply our Bayesian PEP analysis to the ∼1110-1080 Keweenawan paleomagnetic track. We would like to determine allowable plate speeds (not just the latitudinal components), while incorporating the highly variable uncertainties in the ages of the paleomagnetic poles. Furthermore, we want to test whether an abrupt slowdown in the APW path is re-

quired by the data, and if so, when it might have happened. The paleomagnetic poles we use, along with uncertainties and age constraints are given in Table 4.2.

Pole	ψ_p	ϕ_p	A_{95}	Pole reference	Age (Ma)	Lower age (Ma)	Upper age (Ma)	Age reference
Osler reverse (lower)	40.9	218.6	4.8	Swanson-Hysell et al. (2014b)		1105.15	1110	Swanson-Hysell et al. (2016)
Osler reverse (upper)	42.5	201.6	3.7	Swanson-Hysell et al. (2014b); Halls (1974)	1105.15 ± 0.33			Swanson-Hysell et al. (2016)
Mamainse lower reversed 1	49.5	227.0	5.3	Swanson-Hysell et al. (2009, 2014a)		1106	1112	Swanson-Hysell et al. (2014a)
Mamainse lower reversed 2	37.5	205.2	4.5	Swanson-Hysell et al. (2009, 2014a)		1102	1108	Swanson-Hysell et al. (2014a)
Mamainse lower normal and upper reversed	36.1	189.7	4.9	Swanson-Hysell et al. (2009, 2014a)	1100.36 ± 0.25			Swanson-Hysell et al. (2014a)
Mamainse upper normal	31.2	183.2	2.5	Swanson-Hysell et al. (2009, 2014a)		1092	1098	Swanson-Hysell et al. (2014a)
Grand Portage Basalts	46.6	201.5	6.8	Books (1968); Tauxe and Kodama (2009)		1105.28	1108	Swanson-Hysell et al. (2016)
North Shore Volcanic Group	35.8	182.1	3.1	Tauxe and Kodama (2009)		1094.2	1095.8	Schoene et al. (2006); Swanson-Hysell et al. (2016)
Portage Lake Volcanics	25.6	185.9	2.9	Books (1972); Hnat et al. (2006)		1091.67	1093.36	Swanson-Hysell et al. (2016)
Schroeder Lutsen Basalts	27.1	187.8	3.0	Tauxe and Kodama (2009); Fairchild et al. (2016)		1085	1091.5	Fairchild et al. (2016)
Lake Shore Traps	23.1	186.4	4.0	Diehl and Haig (1994); Kulakov et al. (2013)		1084	1091	Fairchild et al. (2016)
Michipicoten Island Formation	17.0	174.7	4.4	Palmer and Davis (1987); Fairchild et al. (2016)	1083.9 ± 0.4			Fairchild et al. (2016)
Freda	2.2	179.0	4.2	Henry et al. (1977)		1070	1085.5	Fairchild et al. (2016)

Table 4.2: Paleomagnetic poles used for the Keweenawan inversion, as well as references for their positions and ages. ψ_p and ϕ_p give the latitude and longitude of the mean pole position, and A_{95} gives the 95% angular confidence interval for that position. For poles with an associated radiometric date we give the age with 2σ error bars. For poles with stratigraphic age control we give upper and lower bounds on the age.

We invert the Keweenawan APW track for one, two, and three paleomagnetic Euler poles. Adding a third PEP did not improve the fit, and it left one Euler pole completely unconstrained. We interpret this as meaning that three PEPs is unnecessary given the data. Therefore we focus on the results with one and two PEPs.

The fit with a single PEP is shown in Figure 4.11. The posterior distribution of the Euler pole position is shown in in blue, and a sampling of the small-circle paths generated from the posterior distribution are plotted over the paleomagnetic poles. Figure 4.12(c) and 4.12(d) show the prior and posterior distributions for the ages of the poles, and Figure 4.12(a) shows the posterior distribution of the plate speed for Laurentia, calculated with respect to Duluth, MN (46.8°N, 92.1°W). The median plate speed for the one-Euler pole inversion is 26.5 cm/yr, with a 95% credible interval of 23.1-30.4 cm/yr.

The fit with two PEPs is shown in Figure 4.13. The posterior distribution of the position for the first Euler pole is shown in blue, and the posterior distribution of the position for the second Euler pole is shown in red. Figure 4.14(c) and 4.14(d) show the prior and posterior distributions for the ages of the poles, and Figure 4.14 shows the posterior distribution of the plate speeds for the two rotations. The inversion places the changepoint between the two Euler rotations at roughly 1098 Ma. Before the changepoint the inverted plate motion is much faster, with median at 30.0 cm/yr and a 95% credible interval of 22.9-39.1 cm/yr. After the changepoint the plate motion has a median of 13.9 cm/yr with a 95% credible interval of 9.9-22.5 cm/yr.

4.7.3 Plate speeds for Mesoproterozoic Laurentia

Both the one Euler pole and the two Euler pole fits are able to do a good job of fitting the APW path, with a few caveats. The one Euler pole inversion does least well fitting the Mamainse lower normal and upper reversed pole, and the North Shore Volcanic Group pole, with the recovered paths skirting the edges of those poles. Furthermore, neither inversion does has a great fit with the Michipicoten Island Formation pole. The two Euler pole case finds a well-constrained changepoint (see Figure 4.14b) at ∼1098 Ma. This slowdown in plate speed is consistent with the conclusions of Davis and Green (1997) and Swanson-Hysell et al. (2009), though the speeds in our model reflect overall plate speeds (rather than just latitudinal speeds) and naturally incorporate age uncertainties.

In both cases implied plate speeds from the early rift magmatism into the main stage are well over 20 cm/yr. These speeds are much higher than any plate speeds for the Cenozoic (Zahirovic et al., 2015), which could be explained by faster average plate motions in the Proterozoic. Alternatively, it could be due to a true polar wander (TPW) event (Evans, 2003; Swanson-Hysell et al., 2009), which can move the solid earth at faster rates than those taken be be the maximum for differential plate motions (Cambiotti et al., 2011). In Chapter 2 we performed a scaling analysis for rates of true polar wander and found that in a younger, more vigorously convecting planet, TPW becomes more likely. If we regard such high plate velocities as unlikely, then TPW becomes a good alternative explanation.

TPW is a difficult signal to disentangle from plate motions, since any given APW path

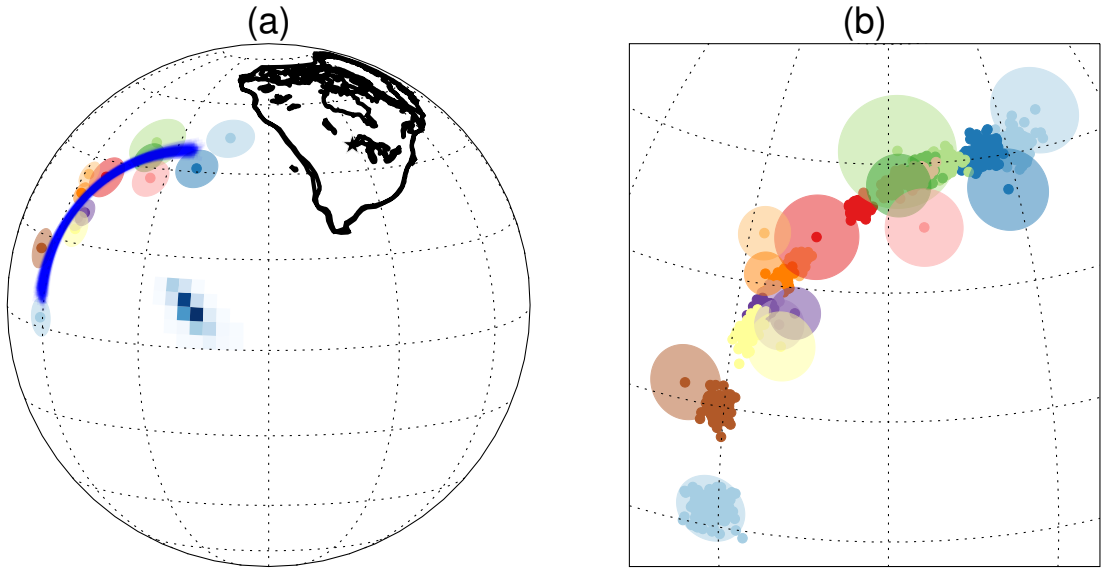

Figure 4.11: Inversion of the Keweenawan track for a single Euler rotation. See Figure 4.12b for pole labels. (a) Euler pole location and sample tracks. The posterior probability distribution is shown in blue, and a representative sample of the tracks generated by the inversion are drawn over the paleomagnetic poles. Also shown is the outline of Laurentia, with the location of Duluth drawn as a star. (b) Paleomagnetic pole positions for draws from the posterior distribution of the inversion superimposed on observed pole positions and their uncertainty.

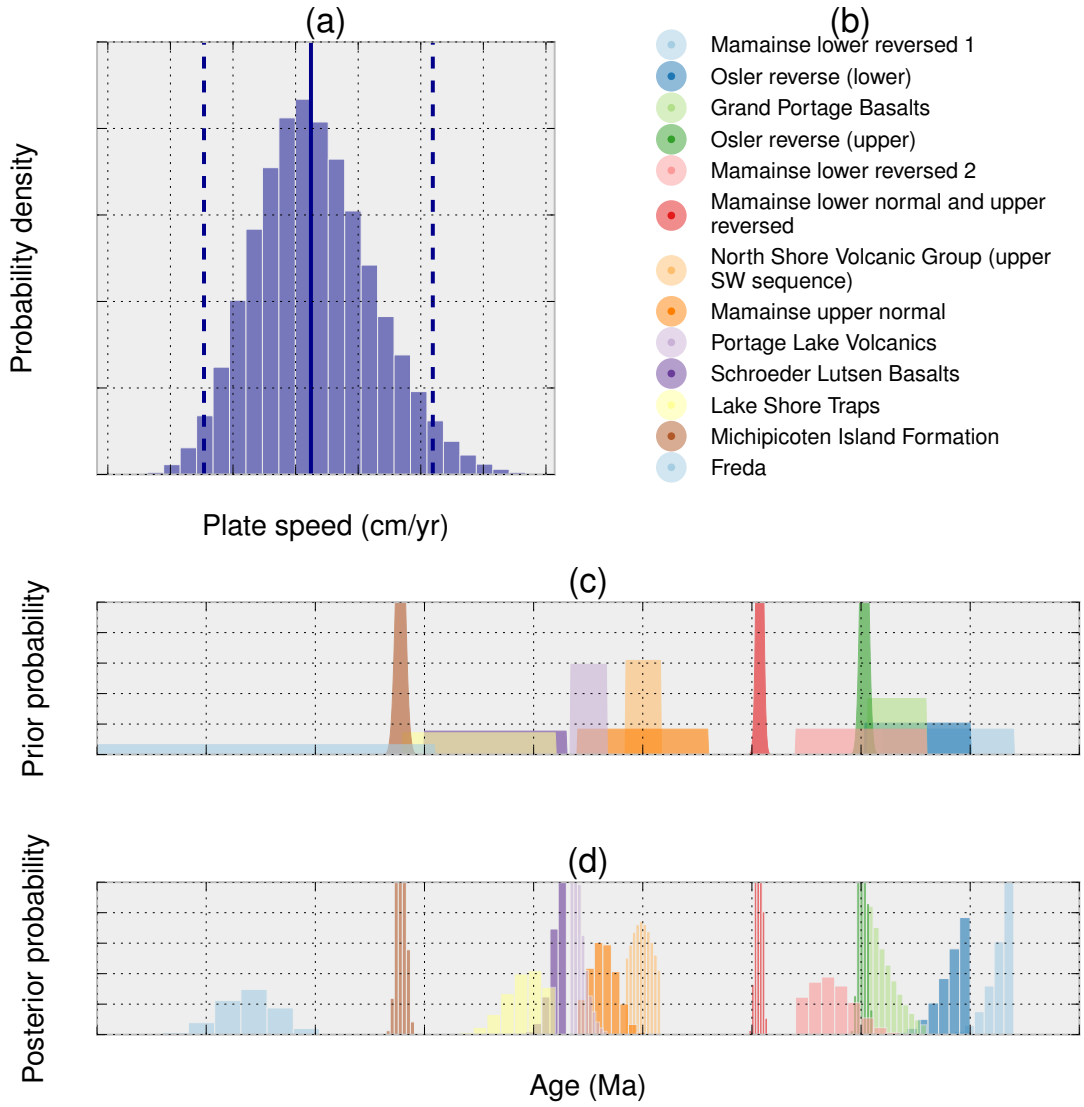

Figure 4.12: Keweenawan results for a single Euler pole inversion. (a) Laurentian plate speed distribution. The solid line shows the median plate speed (26.5 cm/yr) and the dashed lines show the 95% credible interval (23.1-30.4 cm/yr). (b) Legend for the poles used in the inversion. (c) Prior probability distributions for the ages of the Keweenawan paleomagnetic poles. Poles with radiometric ages are given Gaussian prior distributions. Poles with stratigraphic age control are given uniform prior distributions between their bracketing ages. (d) Posterior probability distributions for the ages.

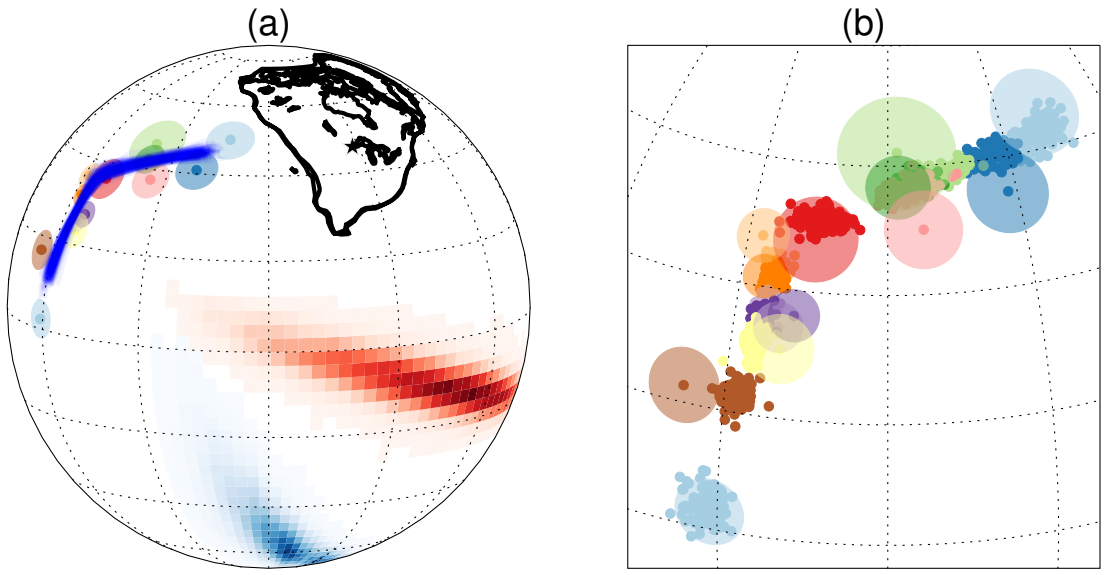

Figure 4.13: Inversion of the Keweenawan track for two Euler rotations. See Figure 4.12b for pole labels. (a) Euler pole locations and sample tracks. The posterior probability distribution of the first rotation is shown in blue, and the distribution for the second rotation is shown in red. A representative sample of the tracks generated by the inversion are drawn over the paleomagnetic poles. Also shown is the outline of Laurentia, with the location of Duluth drawn as a star. (b) Paleomagnetic pole positions for draws from the posterior distribution of the inversion superimposed on observed pole positions and their uncertainty.

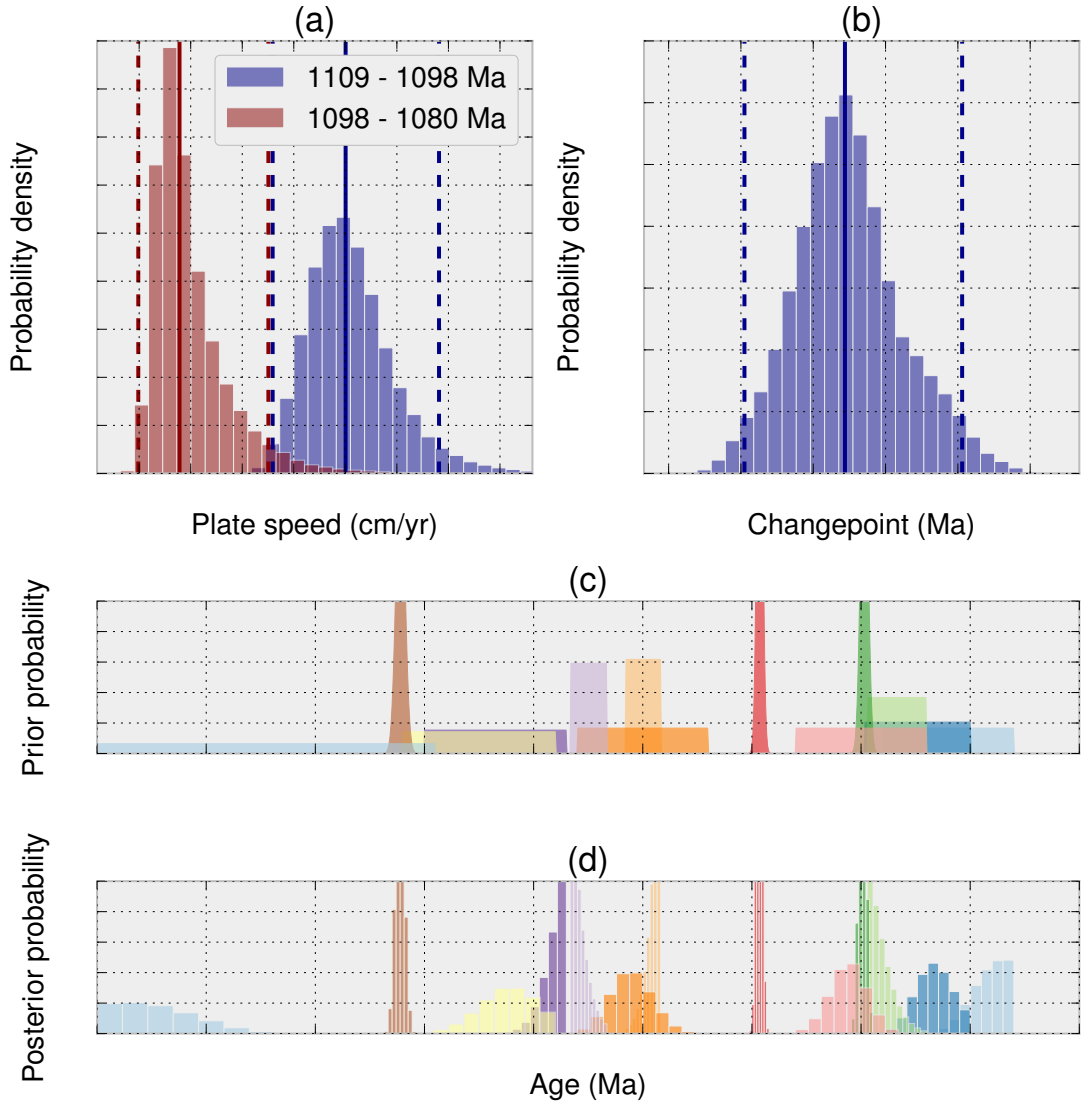

Figure 4.14: Keweenawan results for a two Euler pole inversion. (a) Laurentian plate speed distributions for a two-Euler pole inversion. The blue distribution shows the plate speeds for the first rotation, which occurs from approximately 1109-1098 Ma. The red distribution shows the plate speeds for the second rotation, which occurs from approximately 1098-1080 Ma. The changepoint is approximate, since it is also a random variable with its own posterior distribution. This inversion prefers a fast first rotation and a slower second rotation, though there is some overlap of the distributions. (b) Posterior probability distribution of the changepoint between the first and second rotations. Is median is 1099 Ma with a 95% credible interval of 1096-1102 Ma. (c) Prior probability distributions for the ages of the Keweenawan paleomagnetic poles. Poles with radiometric ages are given Gaussian prior distributions. Poles with stratigraphic age control are given uniform prior distributions between their bracketing ages. (d) Posterior probability distributions for the ages.

can be the result of TPW, plate tectonics, or some combination of the two. An Euler pole that describes true polar wander must be 90° from the spin axis, and if we assume that GAD holds, then the PEP for a true polar wander event must be 90° from the paleomagnetic poles. The PEP for which we invert in the single Euler pole case is well short of 90° from the poles, so it is unlikely to be due to TPW only. It can, however, be caused by a combination of plate motion and TPW.

The PEPs in the two Euler pole inversion do allow for Euler poles that are 90° from the paleomagnetic poles, and thus could be interpreted as primarily due to TPW. The first rotation is $2° - 4°$/Myr, and the second is $1° - 2°$/Myr. These TPW rates are well within the maximum rate estimate of 6°/Myr from Section 2.5, and only moderately higher than the Pleistocene estimates from Cambiotti et al. (2011).

4.8 Conclusions

We have extended the paleomagnetic Euler pole analysis of Gordon et al. (1984) by placing it within a Bayesian framework. This framework is sufficiently flexible so as to include any number of PEP rotations, and allows for appropriate uncertainties in the paleomagnetic pole positions and ages. The resulting posterior distributions provide rigorous uncertainties for the model parameters, and allow for estimates of the full plate motion (not just latitudinal changes). Regularization of the inversions is not accomplished by smoothing parameters, but is instead accomplished by choice of prior probability distributions for the Euler pole parameters, which have clear physical interpretations.

We have implemented the Bayesian inverse problem using Markov-chain Monte Carlo methods. Our code for this implementation is freely available online under an open source license.

We applied our method to two data sets. First, we considered the case of Cenozoic Australia, for which we have detailed plate motion models based on hotspot tracks and fracture zones. Our analysis successfully locates a region of allowable PEP positions which includes the average Euler pole from 0-60 Ma of Seton et al. (2012). However, the discrepancy in the rate of polar motion described by Idnurm (1985b) remains.

Second, we considered the Keweenawan APW track. Our inversions allow for, but do not require, a slowdown in the polar wander path at ~ 1098 Ma. In both cases, the implied Laurentian plate speed during rifting reaches values significantly greater than 20 cm/yr. Such a fast plate speed can be explained by faster Proterozoic plate speeds, or by a TPW event, or a combination of the two.

Future models for the inversion of past plate motions could include TPW as an explicit model parameter. Since TPW and plate motions are both described by finite rotations around Euler poles, it is very difficult to distinguish them, and there should be significant tradeoffs between the APW path being explained mostly by plate motions and mostly by TPW. There is hope for distinguishing them, however, by regularization via the prior distributions, and by the inclusion of more continental blocks in the inversion.

Chapter 5

Conclusion and outlook

The work in this dissertation has approached the topic of true polar wander from several directions, including scaling, numerics, and data analysis.

In Chapter 2 we analyzed TPW from the perspective of fluid dynamics. The rotating planet is most stable when the spin axis coincides with the axis of the largest moment of inertia. TPW is primarily a balance between the generation of anomalies in the moment of inertia tensor via convection and their decay via movement of the spin axis. Our scaling showed that the primary nondimensional numbers controlling TPW are the Rayleigh number Ra, and the Froude number m, defined by the ratio of centrifugal to gravitational forces.

The Froude number sets the size of the rotational bulge, which acts as the brakes on TPW. The dependence on the Rayleigh number is more complicated: at high Ra the flow becomes more chaotic, and the total power in the degree-two part of the density field (which is the part that controls TPW) goes down. However, at high Ra the characteristic response time for TPW also goes down, and these two effects largely cancel. Additionally, at higher Ra, the perturbations to the moment of inertia can produce larger angular differences between the axis of the maximum moment of inertia and the spin axis, which results in faster rates of TPW. The net effect of higher Ra, and the correspondingly more vigorous convection, is that TPW events become more likely. Gold (1955), and later Goldreich and Toomre (1969), used a metaphor of beetles crawling around on the surface of the globe, thereby shifting the moment of inertia and causing TPW. Within this metaphor, our analysis addresses the number, speed, and size of the beetles. As the Rayleigh number increases, we predict more beetles, which move more quickly, but are smaller.

In Chapter 3 we analyzed numerical methods for simulating viscous flows with a free surface boundary condition. Free surface boundary conditions are needed for simulating many tectonic and geomorphologic settings, and allow for the computation of gravity and moment of inertia perturbations in models with arbitrary viscosity structures. We explained the so-called "drunken sailor" numerical instability that has afflicted numerical models with free surfaces in terms of the spectrum of relaxation times for the system. This relaxation time spectrum can be found by solving a generalized eigenvalue problem. Using this framework, we showed that the commonly used quasi-implicit stabilization scheme works by lengthening

the relaxation times, allowing for longer timesteps.

Our spectral analysis also allowed for the construction of a new timestepping scheme that is rooted in nonstandard finite differences. It is first order accurate, and allows for much larger timestep sizes than the forward Euler scheme (if the numerical analyst is willing to forgo accuracy in the shortest timescales of the system).

In Chapter 4 we proposed a new method for analyzing paleomagnetic apparent polar wander paths. Commonly used methods such as spline fits and running means provide smooth, age progressive APW paths from paleomagnetic poles, but it is difficult to know what smoothing parameters are appropriate, or how to incorporate uncertainties in age and position of the poles. We proposed an extension of the paleomagnetic Euler pole method which uses Bayesian Markov chain Monte Carlo methods to address these difficulties. This approach naturally allows for the incorporation of uncertainties in the input data, and automatically provides uncertainties in the model parameters for which we invert. Furthermore, the forward model is rooted in the kinematic model used for the description of plate motions, allowing us to estimate past plate speeds and their uncertainties.

We applied our Bayesian PEP method to paleomagnetic poles from the Mesoproterozoic Keweenawan Midcontinent Rift zone, which has been interpreted to imply extremely fast plate speeds. Our inversions find that the implied plate speeds for Laurentia exceeded 22.9 cm/yr at a 95% credible interval. This speed is significantly faster than the highest plate speeds in models of Cenozoic plate motions. True polar wander, which has the potential to be much faster than plate speeds, is one possible explanation for such high rates.

Bibliography

Adhikari, S., Ivins, E. R., 2016. Climate-driven polar motion: 2003–2015. Science advances 2 (4), e1501693.

Argus, D. F., Gordon, R. G., DeMets, C., 2011. Geologically current motion of 56 plates relative to the no-net-rotation reference frame. Geochemistry, Geophysics, Geosystems 12 (11).

Aster, R. C., Borchers, B., Thurber, C. H., 2005. Parameter estimation and inverse problems. Elsevier, New York.

Bangerth, W., Burstedde, C., Heister, T., Kronbichler, M., 2011. Algorithms and Data Structures for Massively Parallel Generic Adaptive Finite Element Codes. ACM Trans. Math. Softw. 38 (2).

Bangerth, W., Heister, T., Heltai, L., Kanschat, G., Kronbichler, M., Maier, M., Turcksin, B., Young, T. D., 2015a. The `deal.II` Library, Version 8.2. Archive of Numerical Software 3.

Bangerth, W., Heister, T., et al., 2015b. ASPECT: Advanced Solver for Problems in Earth's ConvecTion. `https://aspect.dealii.org/`.

Barenblatt, G. I., 1996. Scaling, self-similarity, and intermediate asymptotics: dimensional analysis and intermediate asymptotics. Cambridge University Press.

Barrell, J., 1914. The status of hypotheses of polar wanderings. Science, 333–340.

Baumann, T. S., Kaus, B. J., Popov, A. A., 2014. Constraining effective rheology through parallel joint geodynamic inversion. Tectonophysics 631, 197–211.

Beck, M. E., 1989. Paleomagnetism of continental North America; Implications for displacement of crustal blocks within the Western Cordillera, Baja California to British Columbia. Geological Society of America Memoirs 172, 471–492.

Beck, M. E., Housen, B. A., 2003. Absolute velocity of North America during the Mesozoic from paleomagnetic data. Tectonophysics 377 (1), 33–54.

Books, K. G., 1968. Magnetization of the lowermost Keweenawan lava flows in the Lake Superior area. Tech. rep., United States Geological Survey.

Books, K. G., 1972. Paleomagnetism of some Lake Superior Keweenawan rocks. Tech. rep., US Govt. Print. Off.,.

Boyden, J. A., Müller, R. D., Gurnis, M., Torsvik, T. H., Clark, J. A., Turner, M., Ivey-Law, H., Watson, R. J., Cannon, J. S., 2011. Next-generation plate-tectonic reconstructions using GPlates. Geoinformatics: cyberinfrastructure for the solid earth sciences 9, 5–114.

Braginsky, S. I., Roberts, P. H., 1995. Equations governing convection in Earth's core and the geodynamo. Geophysical & Astrophysical Fluid Dynamics 79 (1-4), 1–97.

Bryan, P., Gordon, R. G., 1986. Rotation of the Colorado Plateau: An analysis of paleomagnetic data. Tectonics 5 (4), 661–667.

Bull, A. L., Domeier, M., Torsvik, T. H., 2014. The effect of plate motion history on the longevity of deep mantle heterogeneities. Earth and Planetary Science Letters 401, 172–182.

Butler, R. F., 1992. Paleomagnetism: magnetic domains to geologic terranes. Vol. 319. Blackwell Scientific Publications Boston.

Cambiotti, G., Ricard, Y., Sabadini, R., 2011. New insights into mantle convection true polar wander and rotational bulge readjustment. Earth and Planetary Science Letters 310 (3), 538–543.

Carpenter, B., Gelman, A., Hoffman, M., Lee, D., Goodrich, B., Betancourt, M., Brubaker, M. A., Guo, J., Li, P., Riddell, A., 2016. Stan: A probabilistic programming language. J Stat Softw.

Chambat, F., Ricard, Y., Valette, B., 2010. Flattening of the Earth: further from hydrostaticity than previously estimated. Geophysical Journal International 183 (2), 727–732.

Chambat, F., Valette, B., 2001. Mean radius, mass, and inertia for reference Earth models. Physics of the Earth and Planetary Interiors 124 (3), 237–253.

Chan, N.-H., Mitrovica, J., Daradich, A., Creveling, J., Matsuyama, I., Stanley, S., 2014. Time-dependent rotational stability of dynamic planets with elastic lithospheres. Journal of Geophysical Research: Planets 119 (1), 169–188.

Chen, J., Wilson, C., Ries, J., Tapley, B., 2013. Rapid ice melting drives Earth's pole to the east. Geophysical Research Letters 40 (11), 2625–2630.

Cox, A., Hart, R. B., 2009. Plate tectonics: how it works. John Wiley & Sons.

Crameri, F., Schmeling, H., Golabek, G., Duretz, T., Orendt, R., Buiter, S., May, D., Kaus, B., Gerya, T., Tackley, P., 2012a. A comparison of numerical surface topography calculations in geodynamic modelling: An evaluation of the 'sticky air' method. Geophysical Journal International 189 (1), 38–54.

Crameri, F., Tackley, P., Meilick, I., Gerya, T., Kaus, B., 2012b. A free plate surface and weak oceanic crust produce single-sided subduction on Earth. Geophysical Research Letters 39 (3).

Creer, K., Irving, E., Runcorn, S., 1954. The direction of the geomagnetic field in remote epochs in Great Britain. Journal of geomagnetism and geoelectricity 6 (4), 163–168.

Creer, K., Irving, E., Runcorn, S., 1957. Geophysical interpretation of palaeomagnetic directions from Great Britain. Philosophical Transactions of the Royal Society of London A: Mathematical, Physical and Engineering Sciences 250 (974), 144–156.

Creveling, J., Mitrovica, J., Chan, N.-H., Latychev, K., Matsuyama, I., 2012. Mechanisms for oscillatory true polar wander. Nature 491 (7423), 244–248.

Dahlen, F., Tromp, J., Lay, T., 1999. Theoretical Global Seismology. Physics Today 52, 61.

Darwin, G., 1887. On the influence of geological changes on the Earth's axis of rotation. Philosophical Transactions of the Royal Society.

Davidson-Pilon, C., 2015. Bayesian Methods for Hackers: Probabilistic Programming and Bayesian Inference, 1st Edition. Addison-Wesley Professional.

Davis, C., Kahan, W. M., 1970. The rotation of eigenvectors by a perturbation. III. SIAM Journal on Numerical Analysis 7 (1), 1–46.

Davis, D., Green, J., 1997. Geochronology of the North American Midcontinent rift in western Lake Superior and implications for its geodynamic evolution. Canadian Journal of Earth Sciences 34 (4), 476–488.

DeMets, C., Gordon, R. G., Argus, D., Stein, S., 1990. Current plate motions. Geophysical journal international 101 (2), 425–478.

Diehl, J., Haig, T., 1994. A paleomagnetic study of the lava flows within the Copper Harbor Conglomerate, Michigan: new results and implications. Canadian Journal of Earth Sciences 31 (2), 369–380.

Donea, J., Huerta, A., Ponthot, J.-P., Rodriguez-Ferran, A., 2004. Encyclopedia of Computational Mechanics Vol. 1: Fundamentals., Chapter 14: Arbitrary Lagrangian-Eulerian Methods.

Duretz, T., May, D., Gerya, T., Tackley, P., 2011. Discretization errors and free surface stabilization in the finite difference and marker-in-cell method for applied geodynamics: A numerical study. Geochemistry, Geophysics, Geosystems 12 (7).

Dziewonski, A. M., Lekic, V., Romanowicz, B. A., 2010. Mantle Anchor Structure: An argument for bottom up tectonics. Earth and Planetary Science Letters 299 (1), 69–79.

Evans, D. A., 1998. True polar wander, a supercontinental legacy. Earth and Planetary Science Letters 157 (1), 1–8.

Evans, D. A., 2003. True polar wander and supercontinents. Tectonophysics 362 (1), 303–320.

Evans, D. A., 2009. The palaeomagnetically viable, long-lived and all-inclusive Rodinia supercontinent reconstruction. Geological Society, London, Special Publications 327 (1), 371–404.

Fairchild, L. M., Swanson-Hysell, N. L., Ramezani, J., Sprain, C. J., Bowring, S. A., 2016. The end of Midcontinent Rift magmatism and the paleogeography of Laurentia. Lithosphere.

Fisher, N. I., Lewis, T., Embleton, B. J., 1987. Statistical analysis of spherical data. Cambridge university press.

Forsyth, D., Uyeda, S., 1975. On the relative importance of the driving forces of plate motion. Geophysical Journal International 43 (1), 163–200.

Forte, A., Peltier, W., 1987. Plate tectonics and aspherical earth structure: the importance of poloidal-toroidal coupling. Journal of Geophysical Research: Solid Earth 92 (B5), 3645–3679.

Fullsack, P., 1995. An arbitrary Lagrangian-Eulerian formulation for creeping flows and its application in tectonic models. Geophysical Journal International 120 (1), 1–23.

Fung, Y.-c., 1965. Foundations of solid mechanics. Prentice Hall.

Furuichi, M., May, D. A., 2015. Implicit solution of the material transport in Stokes flow simulation: Toward thermal convection simulation surrounded by free surface. Computer Physics Communications 192, 1–11.

Gable, C. W., O'connell, R. J., Travis, B. J., 1991. Convection in three dimensions with surface plates: Generation of toroidal flow. Journal of Geophysical Research: Solid Earth 96 (B5), 8391–8405.

Garrick-Bethell, I., Perera, V., Nimmo, F., Zuber, M. T., 2014. The tidal-rotational shape of the Moon and evidence for polar wander. Nature 512 (7513), 181–184.

Gelman, A., Carlin, J. B., Stern, H. S., Rubin, D. B., 2014. Bayesian data analysis. Vol. 2. Chapman & Hall/CRC Boca Raton, FL, USA.

Gelman, A., Rubin, D. B., 1996. Markov chain Monte Carlo methods in biostatistics. Statistical Methods in Medical Research 5 (4), 339–355.

Gold, T., 1955. Instability of the Earth's axis of rotation. Nature.

Goldreich, P., Toomre, A., 1969. Some remarks on polar wandering. Journal of Geophysical Research 74 (10), 2555–2567.

Goldstein, H., 1965. Classical mechanics. Pearson Education India.

Golub, G. H., Van Loan, C. F., 2012. Matrix computations. Vol. 3. JHU Press.

Gordon, R. G., Cox, A., Harter, C. E., 1978. Absolute motion of an individual plate estimated from its ridge and trench boundaries. Nature 274 (5673), 752–755.

Gordon, R. G., Cox, A., O'Hare, S., 1984. Paleomagnetic Euler poles and the apparent polar wander and absolute motion of North America since the Carboniferous. Tectonics 3 (5), 499–537.

Greff-Lefftz, M., 2004. Upwelling plumes, superswells and true polar wander. Geophysical Journal International 159 (3), 1125–1137.

Hager, B. H., Clayton, R. W., Richards, M. A., Comer, R. P., Dziewonski, A. M., 1985. Lower mantle heterogeneity, dynamic topography and the geoid. Nature 313 (6003), 541–545.

Halls, H., 1974. A paleomagnetic reversal in the Osler Volcanic Group, northern Lake Superior. Canadian Journal of Earth Sciences 11, 1200–1207.

Henry, S. G., Mauk, F. J., van der Voo, R., 1977. Paleomagnetism of the upper Keweenawan sediments: the Nonesuch Shale and Freda Sandstone. Canadian Journal of Earth Sciences 14 (5), 1128–1138.

Hillebrand, B., Thieulot, C., Geenen, T., van den Berg, A. P., Spakman, W., 2014. Using the level set method in geodynamical modeling of multi-material flows and Earth's free surface. Solid Earth 5 (2), 1087–1098.

Hnat, J. S., Van der Pluijm, B. A., Van der Voo, R., 2006. Primary curvature in the Mid-Continent Rift: Paleomagnetism of the Portage Lake Volcanics (northern Michigan, USA). Tectonophysics 425 (1), 71–82.

Iaffaldano, G., Bodin, T., Sambridge, M., 2012. Reconstructing plate-motion changes in the presence of finite-rotations noise. Nature communications 3, 1048.

Idnurm, M., 1985a. Late Mesozoic and Cenozoic palaeomagnetism of AustraliaâĂŤI. A redetermined apparent polar wander path. Geophysical Journal International 83 (2), 399–418.

Idnurm, M., 1985b. Late Mesozoic and Cenozoic palaeomagnetism of AustraliaâĂŤII. Implications for geomagnetism and true polar wander. Geophysical Journal International 83 (2), 419–433.

Idnurm, M., 1994. New Late Eocene pole for Australia, time-averaging of remanence directions, and palaeogeographic reference systems. Geophysical Journal International 117 (3), 827–833.

Irving, E., Green, R., 1958. Polar movement relative to Australia. Geophysical Journal International 1 (1), 64–72.

Irving, E., Park, J., 1972. Hairpins and superintervals. Canadian Journal of Earth Sciences 9 (10), 1318–1324.

Jarvis, G. T., Peltier, W., 1982. Mantle convection as a boundary layer phenomenon. Geophysical Journal International 68 (2), 389–427.

Jupp, P. E., Kent, J. T., 1987. Fitting smooth paths to speherical data. Applied statistics, 34–46.

Kaus, B. J., Mühlhaus, H., May, D. A., 2010. A stabilization algorithm for geodynamic numerical simulations with a free surface. Physics of the Earth and Planetary Interiors 181 (1), 12–20.

Kirschvink, J. L., Raub, T. D., 2003. A methane fuse for the Cambrian explosion: carbon cycles and true polar wander. Comptes Rendus Geoscience 335 (1), 65–78.

Kirschvink, J. L., Ripperdan, R. L., Evans, D. A., 1997. Evidence for a large-scale reorganization of Early Cambrian continental masses by inertial interchange true polar wander. Science 277 (5325), 541–545.

Klootwijk, C., 2009. Sedimentary basins of eastern Australia: paleomagnetic constraints on geodynamic evolution in a global context. Australian Journal of Earth Sciences 56 (3), 273–308.

Köppen, W., Wegener, A., 01 1924. Die Klimate der geologischen Vorzeit. Schweizerbart Science Publishers, Stuttgart, Germany.

Korenaga, J., 2010. Scaling of plate tectonic convection with pseudoplastic rheology. Journal of Geophysical Research: Solid Earth (1978–2012) 115 (B11).

Kramer, S. C., Wilson, C. R., Davies, D. R., 2012. An implicit free surface algorithm for geodynamical simulations. Physics of the Earth and Planetary Interiors 194, 25–37.

Kronbichler, M., Heister, T., Bangerth, W., 2012. High accuracy mantle convection simulation through modern numerical methods. Geophysical Journal International 191 (1), 12–29.

Kulakov, E. V., Smirnov, A. V., Diehl, J. F., 2013. Paleomagnetism of 1.09 Ga Lake Shore Traps (Keweenaw Peninsula, Michigan): new results and implications. Canadian Journal of Earth Sciences 50 (11), 1085–1096.

LeVeque, R. J., 2007. Finite difference methods for ordinary and partial differential equations: steady-state and time-dependent problems. Vol. 98. Siam.

Li, Z.-X., Bogdanova, S., Collins, A., Davidson, A., De Waele, B., Ernst, R., Fitzsimons, I., Fuck, R., Gladkochub, D., Jacobs, J., et al., 2008. Assembly, configuration, and break-up history of Rodinia: a synthesis. Precambrian research 160 (1), 179–210.

Lunn, D. J., Thomas, A., Best, N., Spiegelhalter, D., 2000. WinBUGS-a Bayesian modelling framework: concepts, structure, and extensibility. Statistics and computing 10 (4), 325–337.

Matsuyama, I., Mitrovica, J., Manga, M., Perron, J., Richards, M., 2006. Rotational stability of dynamic planets with elastic lithospheres. Journal of Geophysical Research: Planets 111 (E2).

McKenzie, D., 1968. The influence of the boundary conditions and rotation on convection in the earth's mantle. Geophysical Journal International 15 (5), 457–500.

McLaughlin, J. B., Orszag, S. A., 1982. Transition from periodic to chaotic thermal convection. Journal of Fluid Mechanics 122, 123–142.

McNamara, A. K., Zhong, S., 2005. Thermochemical structures beneath Africa and the Pacific Ocean. Nature 437 (7062), 1136–1139.

Mickens, R. E., 1994. Nonstandard finite difference models of differential equations. World Scientific.

Mickens, R. E., 2002. Nonstandard finite difference schemes for differential equations. The Journal of Difference Equations and Applications 8 (9), 823–847.

Mickens, R. E., 2005. Dynamic consistency: a fundamental principle for constructing nonstandard finite difference schemes for differential equations. Journal of Difference Equations and Applications 11 (7), 645–653.

Milne, G. A., Mitrovica, J. X., 1996. Postglacial sea-level change on a rotating Earth: first results from a gravitationally self-consistent sea-level equation. Geophysical Journal International 126 (3), F13–F20.

Minson, S., Simons, M., Beck, J., 2013. Bayesian inversion for finite fault earthquake source models I-theory and algorithm. Geophysical Journal International, ggt180.

Mitchell, R. N., Kilian, T. M., Raub, T. D., Evans, D. A., Bleeker, W., Maloof, A. C., 2011. Sutton hotspot: Resolving Ediacaran-Cambrian Tectonics and true polar wander for Laurentia. American Journal of Science 311 (8), 651–663.

Mitrovica, J., Forte, A., 2004. A new inference of mantle viscosity based upon joint inversion of convection and glacial isostatic adjustment data. Earth and Planetary Science Letters 225 (1), 177–189.

Mound, J. E., Mitrovica, J. X., Evans, D. A., Kirschvink, J. L., 1999. A sea-level test for inertial interchange true polar wander events. Geophysical Journal International 136 (3), F5–F10.

Müller, R. D., Royer, J.-Y., Lawver, L. A., 1993. Revised plate motions relative to the hotspots from combined Atlantic and Indian Ocean hotspot tracks. Geology 21 (3), 275–278.

Munk, W., MacDonald, G., 1960. The Rotation of the Earth, 323. Cambridge University Press, New York.

Nakiboglu, S., 1982. Hydrostatic theory of the Earth and its mechanical implications. Physics of the Earth and Planetary Interiors 28 (4), 302–311.

Nevanlinna, H., Pesonen, L., 1983. Late Precambrian Keweenawan asymmetric polarities as analyzed by axial offset dipole geomagnetic models. Journal of Geophysical Research: Solid Earth 88 (B1), 645–658.

Newton, I., 1946. Sir Isaac Newton's Mathematical Principles of Natural Philosophy and His System of the World. University of California Press.

Nimmo, F., Pappalardo, R. T., 2006. Diapir-induced reorientation of Saturn's moon Enceladus. Nature 441 (7093), 614–616.

Palmer, H., Davis, D., 1987. Paleomagnetism and U-Pb geochronology of volcanic rocks from Michipicoten Island, Lake Superior, Canada: precise calibration of the Keweenawan polar wander track. Precambrian Research 37 (2), 157–171.

Patil, A., Huard, D., Fonnesbeck, C. J., 2010. PyMC: Bayesian stochastic modelling in Python. Journal of statistical software 35 (4), 1.

Peltier, W., 1974. The impulse response of a Maxwell Earth. Reviews of Geophysics 12 (4), 649–669.

Perron, J. T., Mitrovica, J. X., Manga, M., Matsuyama, I., Richards, M. A., 2007. Evidence for an ancient martian ocean in the topography of deformed shorelines. Nature 447 (7146), 840–843.

Pesonen, L., Nevanlinna, H., 1981. Late Precambrian Keweenawan asymmetric reversals. Nature.

Pesonen, L. J., Halls, H. C., 1983. Geomagnetic field intensity and reversal asymmetry in late Precambrian Keweenawan rocks. Geophysical Journal International 73 (1), 241–270.

Popov, A., Sobolev, S., 2008. SLIM3D: A tool for three-dimensional thermomechanical modeling of lithospheric deformation with elasto-visco-plastic rheology. Physics of the Earth and Planetary Interiors 171 (1), 55–75.

Quinquis, M. E., Buiter, S. J., Ellis, S., 2011. The role of boundary conditions in numerical models of subduction zone dynamics. Tectonophysics 497 (1), 57–70.

Ricard, Y., Spada, G., Sabadini, R., 1993. Polar wandering of a dynamic Earth. Geophysical Journal International 113 (2), 284–298.

Richards, M., Bunge, H.-P., Ricard, Y., Baumgardner, J., 1999. Polar wandering in mantle convection models. Geophysical research letters 26 (12), 1777–1780.

Richards, M. A., Hager, B. H., 1984. Geoid anomalies in a dynamic Earth. Journal of Geophysical Research 89 (B7), 5987–6002.

Richards, M. A., Ricard, Y., Lithgow-Bertelloni, C., Spada, G., Sabadini, R., 1997. An explanation for Earth's long-term rotational stability. Science 275 (5298), 372–375.

Richardson, R. M., 1992. Ridge forces, absolute plate motions, and the intraplate stress field. Journal of Geophysical Research: Solid Earth 97 (B8), 11739–11748.

Roberts, J. H., Zhong, S., 2007. The cause for the north–south orientation of the crustal dichotomy and the equatorial location of Tharsis on Mars. Icarus 190 (1), 24–31.

Rudolph, M. L., Zhong, S., 2014. History and dynamics of net rotation of the mantle and lithosphere. Geochemistry, Geophysics, Geosystems 15 (9), 3645–3657.

Runcorn, S., 1955. Rock magnetism-geophysical aspects. Advances in Physics 4 (14), 244–291.

Sabadini, R., Peltier, W., 1981. Pleistocene deglaciation and the Earth's rotation: implications for mantle viscosity. Geophysical Journal International 66 (3), 553–578.

Sambridge, M., Bodin, T., Gallagher, K., Tkalčić, H., 2013. Transdimensional inference in the geosciences. Phil. Trans. R. Soc. A 371 (1984), 20110547.

Schmeling, H., Babeyko, A., Enns, A., Faccenna, C., Funiciello, F., Gerya, T., Golabek, G., Grigull, S., Kaus, B., Morra, G., et al., 2008. A benchmark comparison of spontaneous subduction modelsâĂŤtowards a free surface. Physics of the Earth and Planetary Interiors 171 (1), 198–223.

Schoene, B., Crowley, J. L., Condon, D. J., Schmitz, M. D., Bowring, S. A., 2006. Reassessing the uranium decay constants for geochronology using ID-TIMS U–Pb data. Geochimica et Cosmochimica Acta 70 (2), 426–445.

Schubert, G., Turcotte, D. L., Olson, P., 2001. Mantle Convection in the Earth and Planets. Cambridge University Press.

Seton, M., Müller, R., Zahirovic, S., Gaina, C., Torsvik, T., Shephard, G., Talsma, A., Gurnis, M., Turner, M., Maus, S., et al., 2012. Global continental and ocean basin reconstructions since 200Ma. Earth-Science Reviews 113 (3), 212–270.

Sivia, D., Skilling, J., 2006. Data analysis: a Bayesian tutorial. OUP Oxford.

Smirnov, A. V., Tarduno, J. A., 2010. Co-location of eruption sites of the Siberian Traps and North Atlantic Igneous Province: Implications for the nature of hotspots and mantle plumes. Earth and Planetary Science Letters 297 (3), 687–690.

Solomatov, V., 1995. Scaling of temperature-and stress-dependent viscosity convection. Physics of Fluids (1994-present) 7 (2), 266–274.

Spada, G., Ricard, Y., Sabadini, R., 1992. Excitation of true polar wander by subduction. Nature 360 (6403), 452–454.

Stahl, W. H., 1942. Astronomy and Geography in Macrobius. In: Transactions and Proceedings of the American Philological Association. JSTOR, pp. 232–258.

Steinberger, B., O'Connell, R. J., 1997. Changes of the Earth's rotation axis owing to advection of mantle density heterogeneities. Nature 387 (6629), 169–173.

Swanson-Hysell, N., Ramezani, J., Fairchild, L., Rose, I., 2016. New geochronologic and paleomagnetic constraints on Midcontinent Rift development. In: Geological Society of America Abstracts with Programs.

Swanson-Hysell, N. L., Burgess, S. D., Maloof, A. C., Bowring, S. A., 2014a. Magmatic activity and plate motion during the latent stage of Midcontinent Rift development. Geology 42 (6), 475–478.

Swanson-Hysell, N. L., Maloof, A. C., Weiss, B. P., Evans, D. A., 2009. No asymmetry in geomagnetic reversals recorded by 1.1-billion-year-old Keweenawan basalts. Nature Geoscience 2 (10), 713–717.

Swanson-Hysell, N. L., Vaughan, A. A., Mustain, M. R., Asp, K. E., 2014b. Confirmation of progressive plate motion during the Midcontinent Rift's early magmatic stage from the Osler Volcanic Group, Ontario, Canada. Geochemistry, Geophysics, Geosystems 15 (5), 2039–2047.

Tarduno, J. A., McWillams, M., Sleep, N., 1990. Fast instantaneous oceanic plate velocities recorded by the Cretaceous Laytonville Limestone: Paleomagnetic analysis and kinematic implications. Journal of Geophysical Research: Solid Earth 95 (B10), 15503–15527.

Tarling, D., Abdeldayem, A., 1996. Palaeomagnetic-pole errors and a 'small-circle' assessment of the Gondwanan polar-wander path. Geophysical Journal International 125 (1), 115–122.

Tauxe, L., Banerjee, S., Butler, R., van der Voo, R., 2010. Essentials of paleomagnetism. University of California Press, Berkeley.

Tauxe, L., Kodama, K. P., 2009. Paleosecular variation models for ancient times: Clues from Keweenawan lava flows. Physics of the Earth and Planetary Interiors 177 (1), 31–45.

Thieulot, C., 2011. FANTOM: Two-and three-dimensional numerical modelling of creeping flows for the solution of geological problems. Physics of the Earth and Planetary Interiors 188 (1), 47–68.

Torsvik, T., Smethurst, M., Meert, J. G., Van der Voo, R., McKerrow, W., Brasier, M., Sturt, B., Walderhaug, H., 1996. Continental break-up and collision in the Neoproterozoic and Palaeozoic-a tale of Baltica and Laurentia. Earth-Science Reviews 40 (3), 229–258.

Torsvik, T. H., Müller, R. D., Van der Voo, R., Steinberger, B., Gaina, C., 2008. Global plate motion frames: toward a unified model. Reviews of Geophysics 46 (3).

Torsvik, T. H., Smethurst, M. A., Van der Voo, R., Trench, A., Abrahamsen, N., Halvorsen, E., 1992. Baltica. A synopsis of Vendian-Permian palaeomagnetic data and their palaeotectonic implications. Earth-Science Reviews 33 (2), 133–152.

Tsai, V. C., Stevenson, D. J., 2007. Theoretical constraints on true polar wander. Journal of geophysical research 112 (B5), B05415.

Turcotte, D., Oxburgh, E., 1967. Finite amplitude convective cells and continental drift. Journal of Fluid Mechanics 28 (01), 29–42.

Van der Voo, R., 1990. The reliability of paleomagnetic data. Tectonophysics 184 (1), 1–9.

Van der Voo, R., Torsvik, T. H., 2001. Evidence for late Paleozoic and Mesozoic non-dipole fields provides an explanation for the Pangea reconstruction problems. Earth and Planetary Science Letters 187 (1), 71–81.

Wilford, J. N., 2001. The mapmakers. Vintage.

Zahirovic, S., Müller, R. D., Seton, M., Flament, N., 2015. Tectonic speed limits from plate kinematic reconstructions. Earth and Planetary Science Letters 418, 40–52.

Zhong, S., Gurnis, M., Moresi, L., 1996. Free-surface formulation of mantle convection-I. Basic theory and application to plumes. Geophysical Journal International 127 (3), 708–718.

Zhong, S., Zhang, N., Li, Z.-X., Roberts, J. H., 2007. Supercontinent cycles, true polar wander, and very long-wavelength mantle convection. Earth and Planetary Science Letters 261 (3), 551–564.

Zhong, S., Zuber, M. T., Moresi, L., Gurnis, M., 2000. Role of temperature-dependent viscosity and surface plates in spherical shell models of mantle convection. Journal of Geophysical Research: Solid Earth (1978–2012) 105 (B5), 11063–11082.

Zienkiewicz, O. C., Taylor, R. L., 1977. The finite element method. Vol. 3. McGraw-Hill London.